Volume I

PB 81 119463

Report No. FRA/ORD-80/53-1

PERFORMANCE OF A SINGLE-SIDED LINEAR INDUCTION MOTOR WITH SOLID BACK IRON AND WITH VARIOUS MISALIGNMENTS

General Electric Company
P.O. Box 43
Schenectady, N.Y. 12305

Gerald B. Kliman
William R. Mischler
W. Russel Oney

SEPTEMBER 1980

Prepared for

U.S. DEPARTMENT OF TRANSPORTATION
FEDERAL RAILROAD ADMINISTRATION
Office of Research and Development
Washington, D.C. 20590

NOTICE

The contents of this report reflect the views of General Electric Corporate Research and Development, which is responsible for the facts and the accuracy of the data presented herein. The contents do not necessarily reflect the official views or policy of the Department of Transportation. This report does not constitute a standard, specification, or regulation.

LIST OF RELATED REPORTS

All experimental and analytical work on linear electric motors, both synchronous and induction, performed by the General Electric Company under contract DOT-FR-64147 is contained in the following four reports:

Report No. FRA/ORD - 80/52

W.R. Mischler and T.A. Nondahl, Performance of a Linear Synchronous Motor with Laminated Track Poles and with Various Misalignments, The General Electric Company, Sept. 1980.

Volume 1 - This volume contains a description and summary of the linear synchronous motor work.

Volumes 2, 3, 4, 5, 6 - These volumes constitute Appendix I, and contain all test data and computer runs on the linear synchronous motor.

Report No. FRA/ORD - 80/53

G.B. Kliman, W.R. Mischler, and W.R. Oney, Performance of a Single-Sided Linear Induction Motor with Solid Back Iron and with Various Misalignments, The General Electric Company, Sept. 1980.

Volume I - This volume contains a description and summary of the linear induction motor work.

Volume II, Appendix B - Part 1 - This volume contains the first part of the reduced data on the linear induction motor work.

Volume II, Appendix B - Part 2 - This volume contains the second part of the reduced data on the linear induction motor work.

Report No. FRA/ORD -80/54

T.A. Nondahl and E. Richter, Comparisons Between Designs for Single-Sided Linear Electric Motors: Homopolar Synchronous and Induction, The General Electric Company, Sept.1980. (This report is complete in one volume.)

Report No. FRA/ORD - 80/73

G.B. Kliman, D.G. Elliott, V.B. Honsinger, T.A. Lipo, W.R. Mischler, T.A. Nondahl, and W.R. Oney, Performance of a Single-Sided Linear Induction Motor with Solid Back Iron and with Various Rail Configurations/Evaluation of the Claw-Pole Linear Synchronous Motor and Performance of the Homopolar Linear Synchronous Motor with Solid-Iron Poles, The General Electric Company, Sept.1980.

Volume 1 - This volume contains various experimental and analytical studies of three types of single-sided linear motors: induction, claw-pole, and homopolar synchronous.

Volume 2 - This volume contains all experimental runs connected with the studies of Volume 1.

TECHNICAL REPORT STANDARD TITLE PAGE

1. Report No.
FRA/ORD-80/53-1

2. Government Accession No.

3. Recipient's Catalog No.

4. Title and Subtitle
Performance of a Single-Sided Linear Induction Motor with Solid Back Iron and with Various Misalignments -Volume 1

5. Report Date
September 1980

6. Performing Organization Code

7. Author(s) Gerald B. Kliman, William R. Mischler, and W. Russel Oney

8. Performing Organization Report No.
SRD-78-069

9. Performing Organization Name and Address

General Electric Company
Corporate Research and Development
P.O. Box 43
Schenectady, New York 12301

10. Work Unit No.

11. Contract or Grant No.
DOT-FR-64147

12. Sponsoring Agency Name and Address
U.S. Department of Transportation
Federal Railroad Administration
Office of Research and Development
Washington, D.C. 20590

13. Type of Report and Period Covered
Phase II - Final Report
September 15, 1975 -
May 15, 1978

14. Sponsoring Agency Code

15. Supplementary Notes

16. Abstract

A test facility was designed and built to measure all aspects of the performance of a single-sided high-speed linear induction motor with solid back iron over a wide range of frequency, speed, and excitation. The facility was equipped and instrumented to measure all the usual performance parameters plus all of the six-axis forces in normal operation and, when displaced, in the remaining five degrees of freedom (air gap, lateral, pitch, roll, and yaw). Performance in the normal position was compared to the mesh/matrix prediction. Generally good agreement was obtained between measured and predicted values of thrust and efficiency. Differences between predicted and measured thrust (especially at high slips) were related to the solid back iron and skin saturation. Agreement between predicted and measured normal forces was not satisfactory. The six-axis force measuring system was thoroughly analyzed to determine the range of validity of the measurements and the errors inherent in using a sector motor to simulate a flat linear motor.

17. Key Words (Selected by Author(s))

Linear induction motors, Linear electric motors, High-speed ground transportation

18. Distribution Statement

Document is available to the public through the National Technical Information Service, Springfield, VA 22161

19. Security Classif. (of this report)
UNCLASSIFIED

20. Security Classif. (of this page)
UNCLASSIFIED

21. No. of Pages
103

22. Price

INTRODUCTION

This report summarizes the results of the major part of tests run on the General Electric/Department of Transportation Single-Sided Linear Induction Motor (SLIM). This was part (Phase II) of a program to investigate both linear induction motors and linear synchronous motors. In this portion of the program, the performance of the linear induction motor was measured over a wide range of speeds, frequencies, and currents. Performance under "off-nominal" or "G-matrix" conditions was also run. That is, the stator was displaced by various offsets and angles for those tests. Additional tests, including reduced side bars, lateral flux traverses, and "iron only" performance were run separately (Phase IV) and will be summarized in another report.

Section 1 of this report describes the experimental motor, test stand, and data acquisition system. An explanation of the processed data format is given in Section 2. The off-line FORTRAN Program used to process the data is given in Appendix A. The complete reduced data is given in Appendix B (in a separate volume). The principal results of the displaced motor (G-matrix) are presented and interpreted in Section 3. The principal results and interpretation of the nominal performance are presented in Section 4. Since thrust, normal force, pitch torque, and so on, as measured by a 6-axis force measuring system (force yoke) form a major part of the data, a discussion of the validity of these results is presented in Section 5.

TABLE OF CONTENTS

TABLE OF CONTENTS (CONT'D)

Section Page

LIST OF ILLUSTRATIONS

Figure Page

LIST OF ILLUSTRATIONS (CONT'D)

LIST OF ILLUSTRATIONS (Cont'd)

LIST OF ILLUSTRATIONS (Cont'd)

LIST OF TABLES

Section 1

EXPERIMENTAL APPARATUS

A cylindrical sector motor configuration has been chosen to model the single-sided linear induction motor (SLIM). Surface speed, pole size, rotor surface resistivity, and gap dimensions for a full-size machine are used for the model. Only the number of poles has been reduced. Characteristics of a 1.4 m wheel diameter are compatible with the rotational speed of the load machine, the mechanical stress limitations of aluminum alloy and steel plate, and the size limits of available machine tools.

A four-pole SLIM design is the best compromise for the model. If a two-pole model were used, it would be dominated by end effects. It would be so unlike the full-size machine being modeled that the test results would be difficult to interpret. A six-pole model would wrap around the rotor more than 90°, making experiments with different clearance gaps impossible to perform.

The SLIM model is rated 150 hp at 111 m/s (250 mph). This corresponds to a thrust of 1000 N. Motor and test facilities are designed to obtain performance characteristics over a wide range of conditions that are likely to be encountered by high-speed linear motors for locomotive propulsion.

Stator iron spans a 79° sector of a circle. A thin-wall aluminum cylinder is backed by a disk of steel. This simulates a reaction rail of infinite length. Clearance gap for the model is 18.2 mm, which is typical for a full-size SLIM.

Design features for the model SLIM are shown in Table 1-1.

Ten force sensors support or restrain the stator. Their locations are shown in Figure 1-1. The fixture in which the force sensors are mounted bolts to the base of the dynamometer. Figure 1-2 shows the stator connections. Temperature differences between components in the fixture are monitored. A large differential expansion might introduce a strain-related component of voltage in the sensor output signal.

Sensors are positioned at right angles to each other in three axes. A data reduction program resolves the measurements into thrust, normal, and lateral forces; and pitch, yaw, and roll torques.

Rail topography with respect to thickness and overhang of the aluminum reaction rail was investigated with the aid of a Federal Railway Administration-supplied sine wave math model [1]. A unique feature of the reaction rail which is not accounted for in the math model is its unlaminated back iron. It affects performance by making the reaction rail appear thicker. A solid steel rotor is the most practical configuration for the SLIM experiment. And, in a practical application, solid steel appears to be more cost-effective than laminated back iron.

TABLE 1-1. SLIM MODEL DESIGN FEATURES

Stator	
Sector length	0.965 m (38.0 in)
Stack width	0.1715 m (6.75 in)
Lamination thickness	0.483 mm (0.019 in)
Inside diameter	1.4016 m (55.18 in)
Slots per pole	9
Pole pitch	0.200 m (7.88 in)
Slot pitch	22.24 mm (0.875 in)
Slot width	13.08 mm (0.515 in)
Slot depth	61.47 mm (2.42 in)
Slots and teeth	43 and 44
Phases	3
Wound poles	4
Circuits	1
Connection	Wye
Winding	Independent
Coil pitch	7/9
Coils - formed	36
Turns per coil	4
Wire arrangement in conductor	2 wide by 4 high
Wire size	5.08 mm by 1.40 mm-QYT
Total weight (on supports)	3679 n (827 lb)
Rotor	
Back iron	
Width	0.1715 m (6.75 in)
Outside diameter	1.3589 m (53.5 in)
Material	1020 steel
Electrical conductivity	0.050 X 10^8 s/m @ 25 °C
Reaction rail	
Width	0.2985 m (11.75 in)
Outside diameter	1.3653 m (53.75 in)
Thickness	3.175 mm (0.125 in)
Material	Aluminum 6061-T6
Electrical conductivity	0.236 X 10^8 s/m @ 28 °C
Gaps	
Iron Gap	21.4 mm (0.841 in)
Clearance gap	18.2 mm (0.716 in)

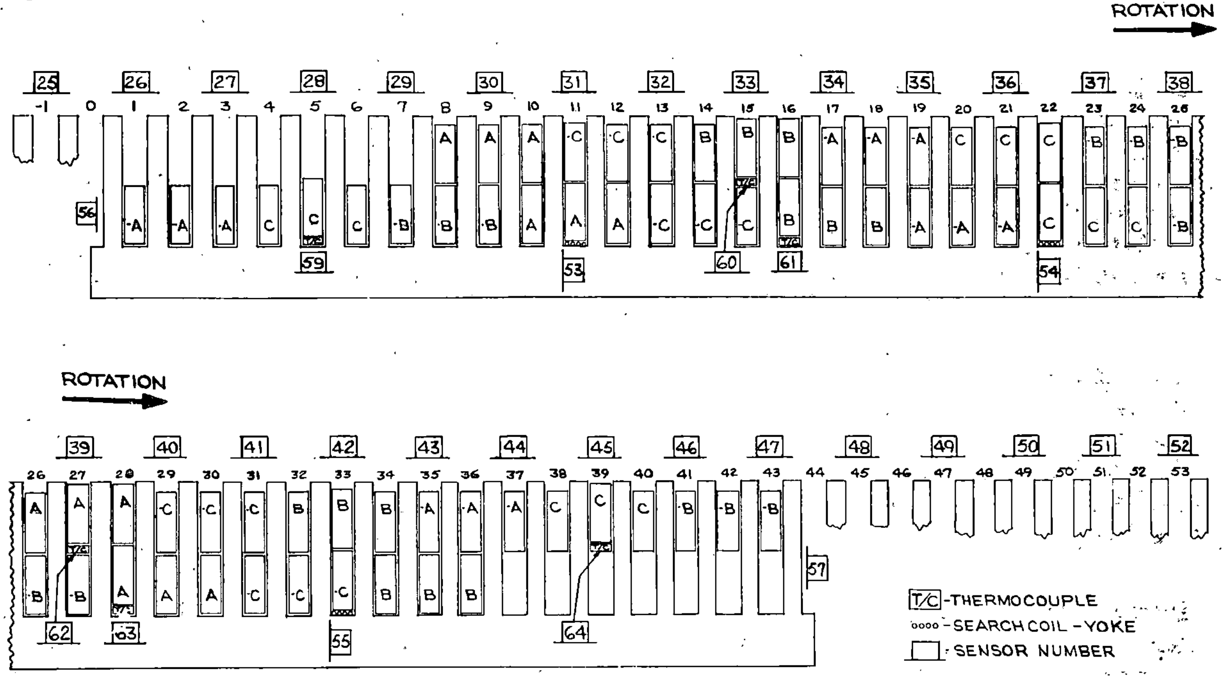

FIGURE 1-1. SENSOR LOCATIONS IN LIM STATOR.

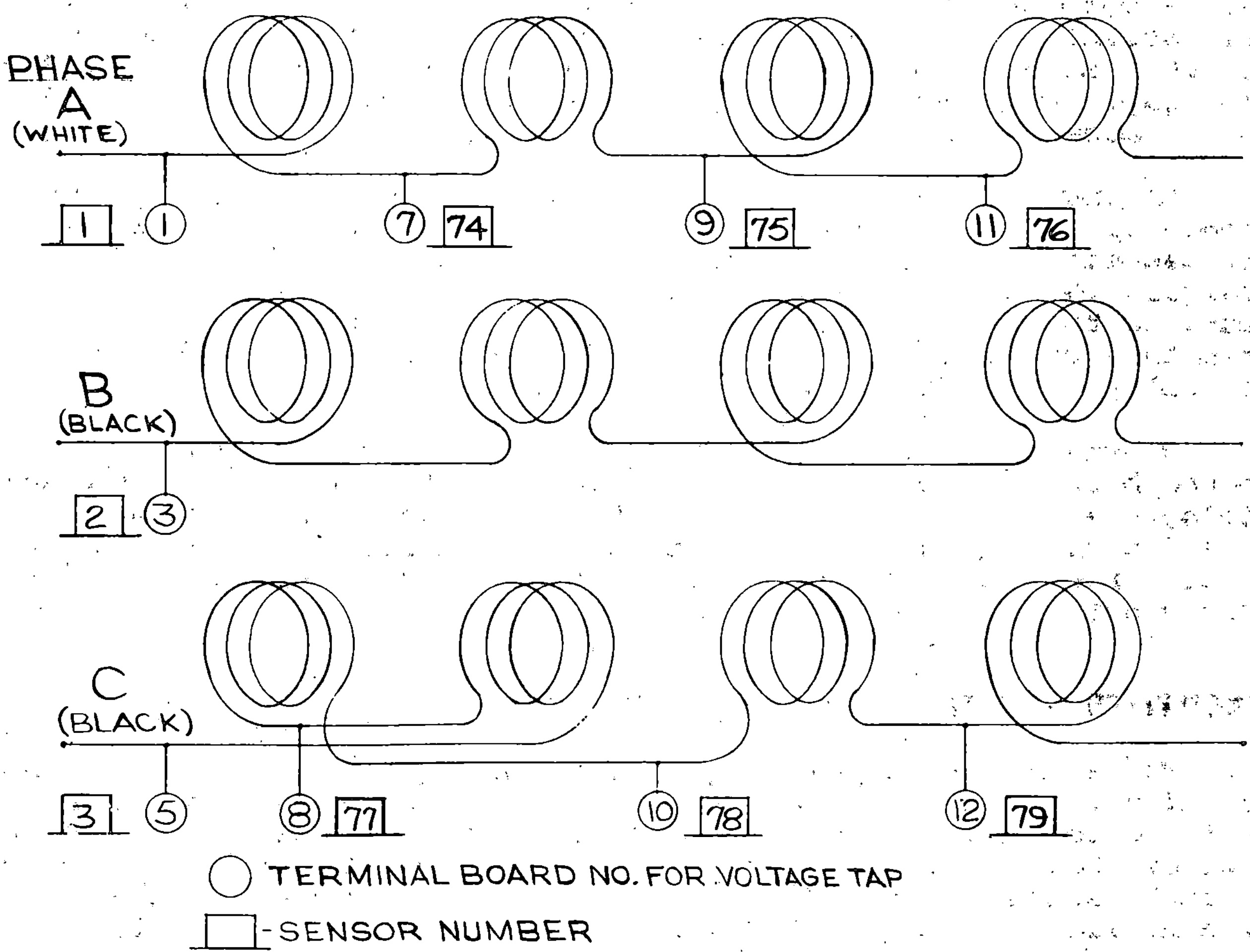

FIGURE 1-2. LIM STATOR CONNECTION DIAGRAM.

A thick plate of AISI 1020 steel, mill-certified, was turned to finished dimensions. Ultrasonic examination of the disk and a magnetic test and red dye test of the finished bore have revealed no serious flaws or conditions. Two sections of sheet aluminum were stretched over the outside of the steel disk. Then they were butt-welded to form a cylinder with the desired overhang. The side bars extended about one-third pole pitch beyond the steel on both sides.

The reaction rail temperature was measured with an optical pyrometer. Total temperature of the overhang typically reached 28 °C when the data was taken. The center section, which is heat-sinked to the steel, warms up more slowly. Electrical conductivity of aluminum alloy 6061 having a T6 temper is 43% maximum at 20 °C, which is equivalent to 0.2363×10^8 s/m at 28 °C.

Both the model SLIM and the full-size SLIM are "copper" motors. Air gap flux density should be low, and current loading should be high. These criteria are opposite of present-day round motor practice. The difference between a SLIM and a round machine is the size of their respective air gaps. Railroad practice requires a very large clearance gap to accommodate expected variations when SLIM propulsion is adapted to present trackage with a minimum of rework. In addition, the sheet conductor takes up space within the iron gap. The resulting ratio of iron gap to pole pitch is 10.7% in the model SLIM.

An increase in pole pitch should improve machine performance. Frequency will be lower; more ampere-conductors will be available for magnetizing flux. Yoke flux in the reaction rail will be greater, but thickness is determined by mechanical considerations. Thus, up to a point, the iron rail need not be enlarged in section. When this point is reached, further increase in pole pitch should be evaluated for its cost effectiveness.

Because the air gap flux and tooth flux are low, the best slot-to-tooth ratio is 60:40. Above this ratio the end turns become unwieldy. A wide slot has the advantage of lower slot leakage flux in addition to increased current loading capability. The air gap is so large that Carter's coefficient is almost unaffected by the slot width.

FACILITIES AND TEST SETUP

The SLIM model stator may be seen in Figure 1-3. It is mounted on a fixture which incorporates all force sensors. Sensors are positioned to measure reaction forces in three orthogonal axes. Movement of the stator is restricted to just enough to produce an acceptable signal from a strain gage. This is no more than one-tenth of a millimeter. Vertical forces are measured directly on the stator. Horizontal forces in the other two axes result from the

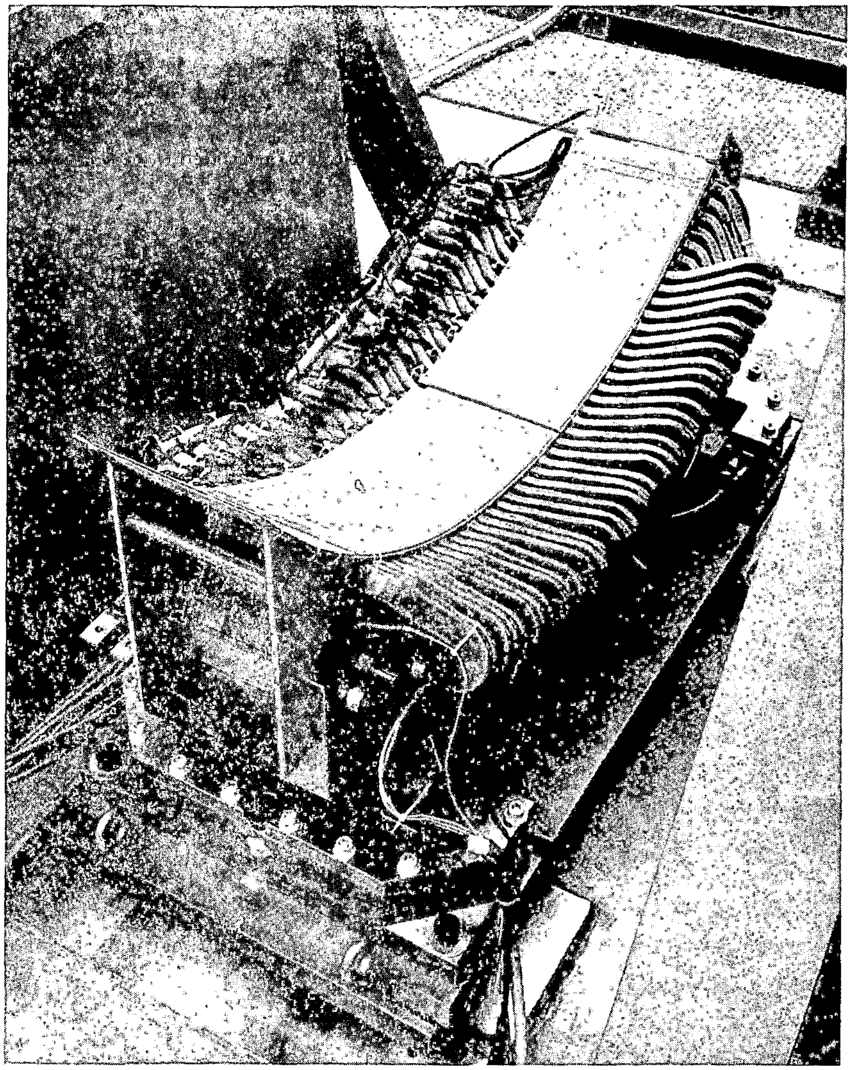

FIGURE 1-3. SLIM STATOR WITH SEARCH COILS INSTALLED.

relative movement of components in the fixture against the spring constant of the gages. Movable components in the fixture roll on ball bearings and case-hardened surfaces. The resulting motion is almost friction free. A total of 10 force sensors is used: four are vertical; two are lengthwise; four are crosswise - one at each corner.

A closeup view of search coils in the air gap may be seen in Figure 1-4. Each coil spans one tooth pitch. The width of the coil covers the full width of the core. This shape and size average the nonuniform distribution of flux in the crosswise direction.

The SLIM model may be seen in Figure 1-5. It is directly connected to a dynamometer load machine. A steel disk which supports the aluminum reaction rail carries the flux. A noncontacting torque transducer floats between shaft ends.

FIGURE 1-4. AIR GAP FLUX SEARCH COILS.

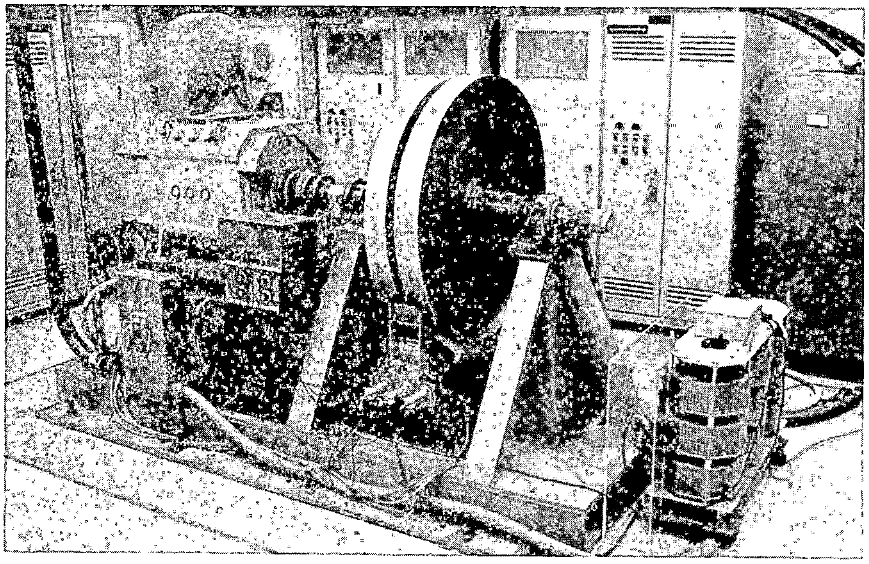

FIGURE 1-5. MODEL SLIM MOUNTED IN TEST STAND.

Thrust is determined by two methods: first, measured torque (which has been corrected for friction and windage - a small correction) is divided by the radius arm to give electromagnetic thrust; and, second, vertical and longitudinal restraint forces on the stator are reduced to thrust by calculations which include wraparound effects.

Controls for the dynamometer load machine and variable frequency power source may be seen in Figure 1-6. Test runs are made at set speed points with the dynamometer speed control. Frequency and current are supplied to the SLIM stator from a separately controlled constant-current inverter (CCI). A block diagram of the power system is shown in Figure 1-7. The CCI power circuit may be seen in Figure 1-8. Frequency is adjustable up to 400 Hz.

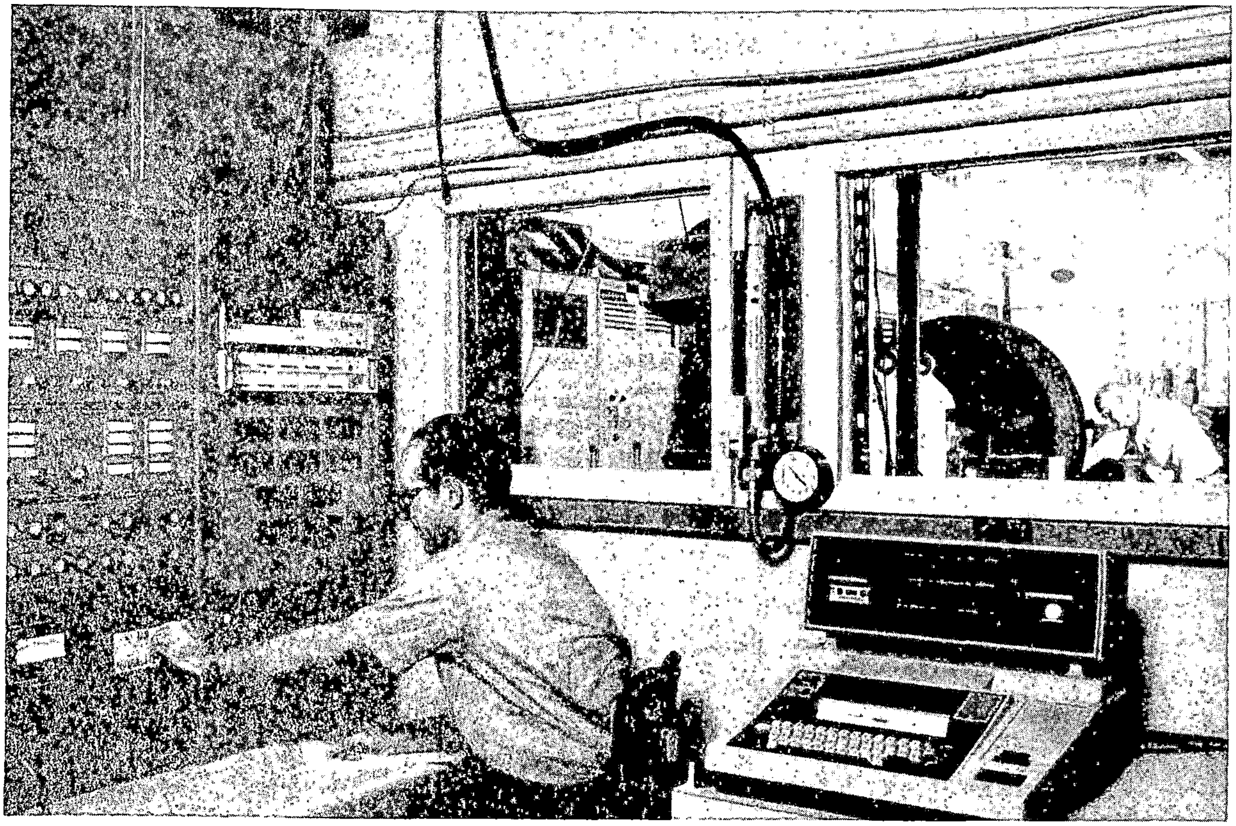

FIGURE 1-6. SLIM CONTROL ROOM.

Many electrical and mechanical parameters are measured and recorded during a test run to fully characterize the SLIM. A data acquisition system (DAS), shown in Figure 1-9, shortens the time needed for a test run and removes human error from the test data. A high-speed scanner, a microprocessor, a memory, and a cassette tape recorder are the basic parts of the DAS.

All measured parameters are converted to a dc analog signal between zero and +9.99 V. These signals are applied continuously to the scanner terminals. A total of 79 parameters are scanned. This is repeated two more times, for a total of three scans in

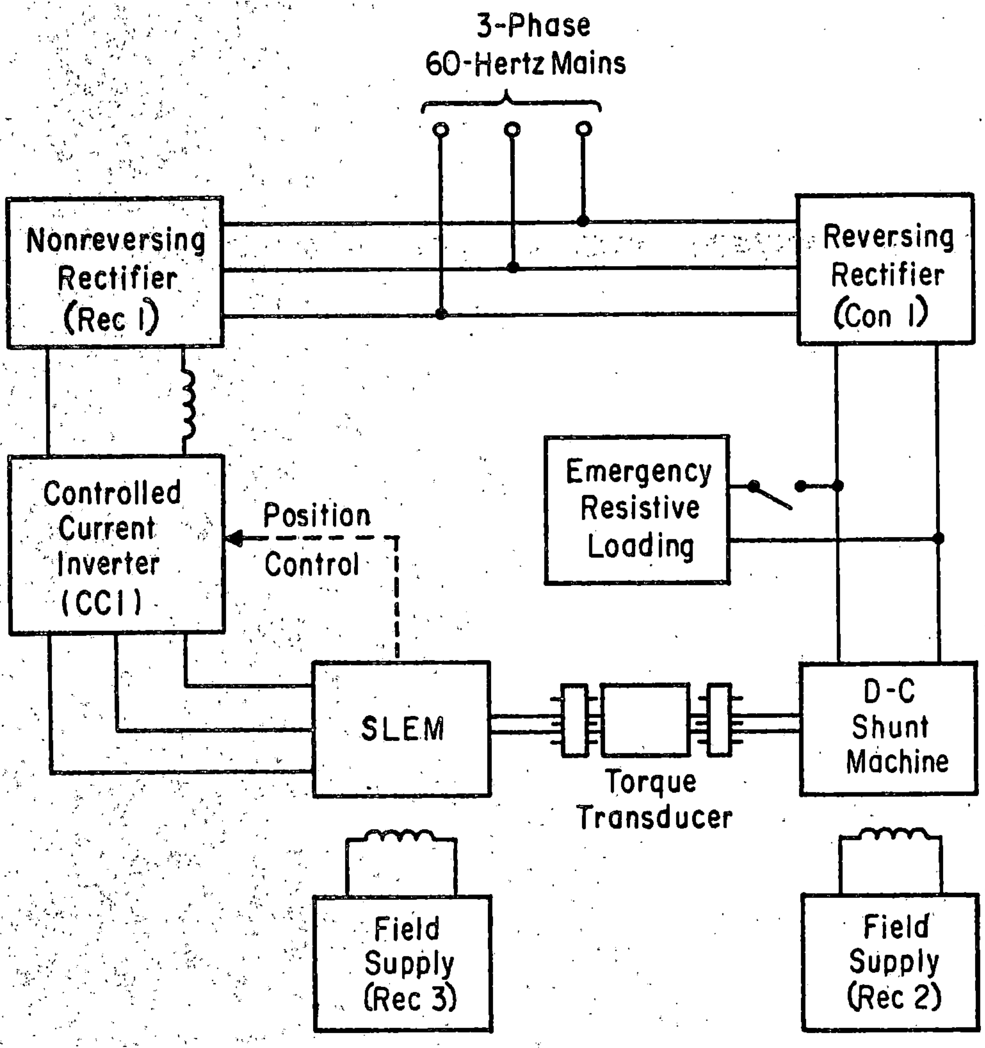

FIGURE 1-7. SLIM LABORATORY TEST HOOKUP.

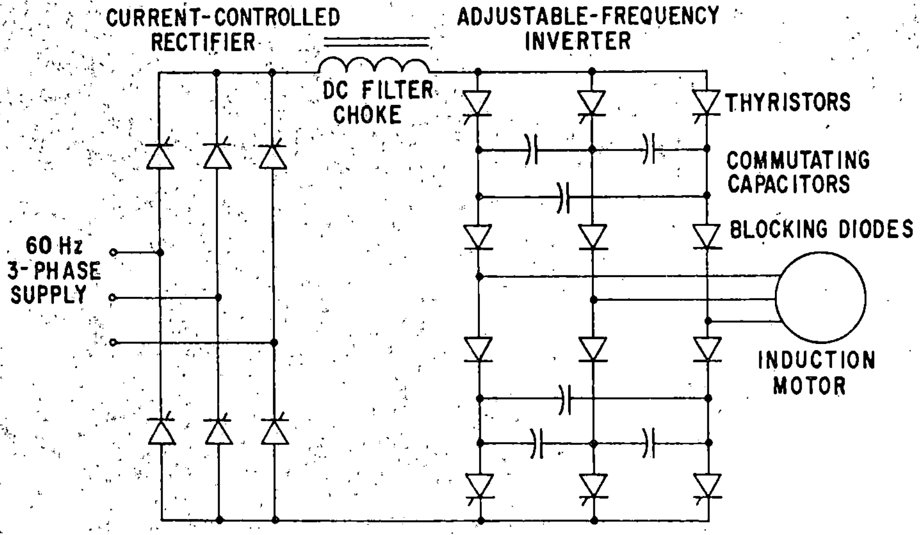

FIGURE 1-8. CONTROLLED-CURRENT INVERTER DRIVE FOR INDUCTION MOTOR.

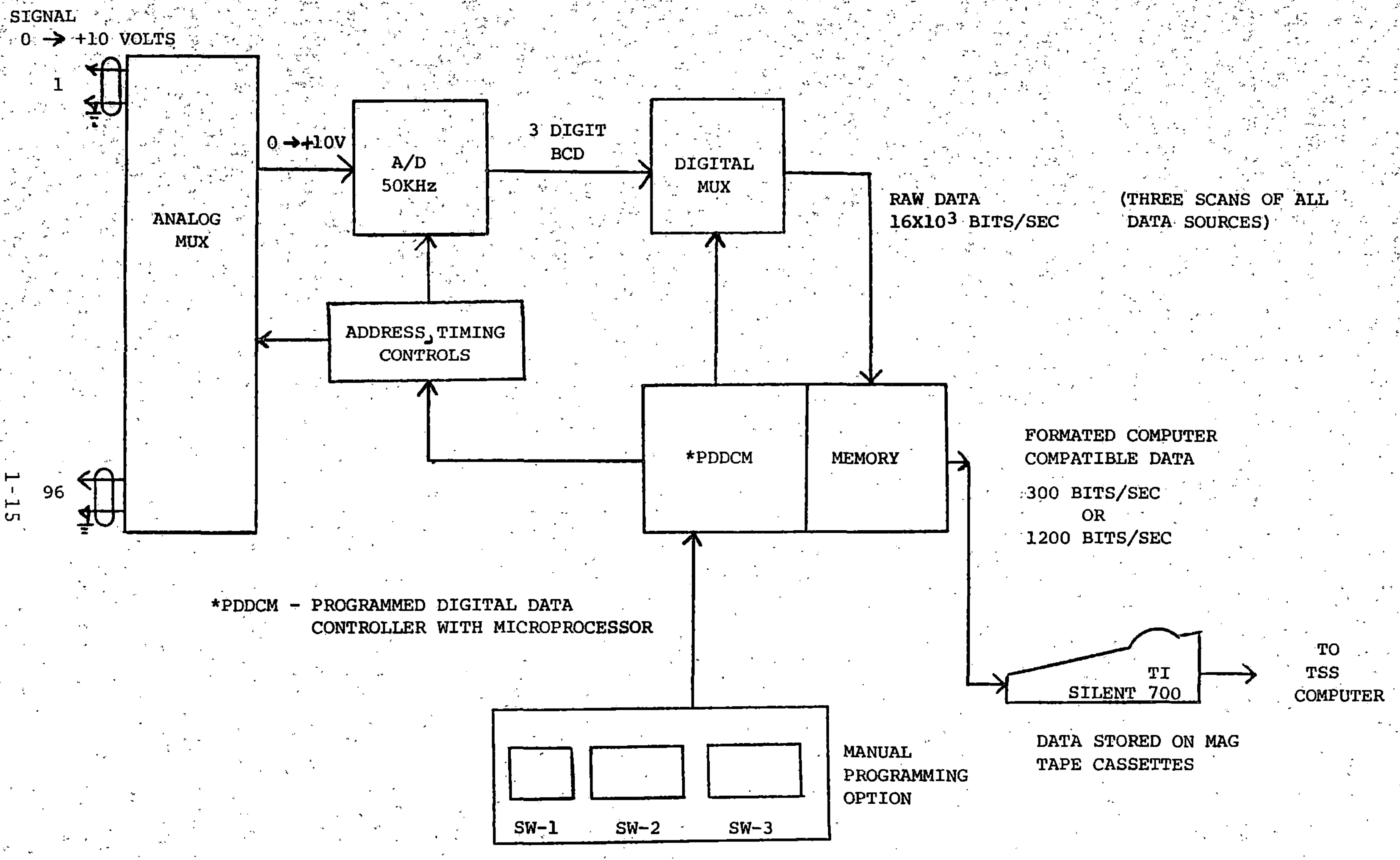

*PDDCM - PROGRAMMED DIGITAL DATA CONTROLLER WITH MICROPROCESSOR

SW-1 - SELECT NUMBER OF SCANS 0 - 3

SW-2 - SELECT BEGINNING ADDRESS

SW-3 - SELECT END ADDRESS

FIGURE 1-9. DATA ACQUISITION SYSTEM.

less than a second. These data are acquired faster than they can be imprinted directly on a magnetic tape cassette. Hence, a temporary memory accumulates the data while it is being taken. After the scans have been made and the data reside in memory, transfer to a cassette tape is automatically implemented. Transfer is completed in only a few seconds. Then, at the convenience of the operator, the data which are now on tape may be put into a digital computer for data reduction.

Figure 1-10 shows raw data for an example test run. The first line is for identification. The three-digit numbers between commas are the analog values of dc voltages with their decimal points omitted.

```
                LIST DATA

9/13 14:30 999 1014 24 150 250 2
000,263,273,269,258,255,261,000,000,000
089,507,000,020,000,452,422,437,464,033
030,023,027,058,000,019,047,101,155,277
289,290,345,345,362,361,357,358,396,381
340,354,335,325,319,252,238,139,062,042
031,023,019,592,403,682,025,037,000,198
000,071,520,213,271,363,026,999,367,192
223,881,001,061,300,212,105,263,199,096
-01,000,265,273,270,259,256,262,000,000
000,090,507,000,001,000,455,420,437,459
033,029,025,026,068,000,018,050,102,155
277,290,293,345,349,362,380,361,358,398
365,340,356,336,325,322,254,237,141,062
041,031,023,019,597,407,668,025,037,000
212,480,414,002,294,136,220,405,999,213
223,197,881,000,083,296,215,102,263,202
092,-01,000,264,274,270,259,256,261,000
000,000,085,507,000,000,000,457,422,432
466,034,031,021,029,058,000,019,049,102
155,276,288,293,343,344,364,377,360,358
389,385,339,353,337,323,320,254,236,140
063,041,031,023,019,595,406,662,025,037
000,481,999,283,339,106,456,129,462,999
251,201,244,882,000,081,299,213,106,281
204,093,-01,-02
```

FIGURE 1-10. RAW DATA FROM TYPICAL TEST RUN.

The identification line begins with the date of test. Next comes the time of test on a 24-hour clock. This is followed by a sequential run number, revolutions per minute, percent slip, line frequency, and either amperes or volts. Finally, there is the signature of the operator.

Data for each scan begins with a marker "000" and ends with a "-01." The end of the data recording is flagged with the marker "-02." Raw data are sequenced exactly as shown in the Sample Data Output, Section 2, pages 2-2 and 2-3.

The most vulnerable part of the DAS is the analog signal supplied to the scanner. A great deal of shielding is required, and, in some cases, a filter is required to eliminate such spurious signals as a local radio station. Instrumentation received frequent calibration with follow-on checks of tape data versus input calibration signals. In general, the test data acquired by the DAS have been consistent, repeatable, and accurate. Table 1-2 is a list of sensed parameters.

TABLE 1-2. SENSED PARAMETERS

Parameter	Number of Sensors
Phase voltage	3
Phase current	3
Phase power	3
Line frequency	1
Motor r/min	1
Shaft torque	1
CCI dc voltage	1
CCI dc current	1
Force sensors	10
Flux search coils	33
Temperature	12
Load motor voltage	1
Load motor current	1
Load motor field current	1
Phase belt tap voltages	6

Section 2

EXPERIMENTAL DATA

INTRODUCTION

SLEM data are stored in raw data files as shown by example in Figure 1-10. Further reduction by a data reduction program produces an output in the form shown on pages 13, 14, and 15. An identifying heading line with basic information about the conditions of the run is followed by a tabulation of the three voltage readings from each sensor channel and the average of these readings. This information was printed on every run in an effort to detect faulty channels when and if they failed. Following this tabulation are calculations from the data of voltage, current, input power, speed, torque, force, flux, and temperature. The program interprets the raw data and calculates the electrical and mechanical performance measures of the machine.

In Appendix A is a listing of the data reduction program used for runs at 150 Hz on August 9, 1977, for Runs #785 and up. Programs were changed from time to time during testing as voltage and current signal levels were changed and as operating frequencies were changed. The changes to programs were made in multipliers on the volts, amperes, and watts channels and in the friction and windage calculations. Programs for generating mode data were similar to motoring ones except for appropriate sign changes.

In the testing of the SLIM, some data channels were found to be of minimal importance, and these were not tuned up for reliable output. These include:

#13	DC Link Volts
#14	DC Link Amperes
#59-70	Temperatures
#71-73	DC Load Motor Parameters

As time permits in the schedule for setting up and testing the synchronous homopolar machine, these channels will be put into action. Their absence in the induction motor data is of minimal importance.

The so-called "Phase Belt Voltage" readings at the bottom of page 15 need explanation. They form only a first approximation of the actual rms voltages per phase belt because they are calculated as algebraic differences of the rms tap voltages. No information as to relative phase of the tap voltages enters the calculation.

The data runs cataloged here and presented in Appendix B have had the raw data tabulation, the analysis of the untuned temperature

SAMPLE DATA OUTPUT

```
DATE     TIME   RN#    DRUMRPM  SLIP %   OSC HZ   VOLTS   ENG
7/2      15:55  607    409      50       150      200     2


SENSOR#        1ST READING    2ND READING    3RD READING    AVERAGE
   1           4.1400         4.1400         4.1400         4.1400
   2           4.1300         4.1300         4.1200         4.1267
   3           4.1700         4.1600         4.1700         4.1667
   4           2.0700         2.0700         2.0600         2.0667
   5           2.0400         2.0300         2.0300         2.0333
   6           2.0900         2.0900         2.0900         2.0900
   7           0.1200         0.1200         0.1300         0.1233
   8           0.1400         0.1500         0.1500         0.1467
   9           0.1300         0.1500         0.1400         0.1400
  10           0.8800         0.8600         0.8600         0.8667
  11           2.0400         2.0400         2.0500         2.0433
  12           0.6600         0.6600         0.6600         0.6600
  13           3.2100         2.5900         2.1000         2.6333
  14           0.             0.             0.             0.
  15           5.1400         5.1400         5.1500         5.1433
  16           4.9500         4.9600         4.9600         4.9567
  17           5.0200         5.0300         5.0100         5.0200
  18           5.2100         5.2000         5.2000         5.2033
  19           0.2400         0.2500         0.2300         0.2400
  20           0.1700         0.1700         0.1600         0.1667
  21           0.1900         0.2000         0.2100         0.2000
  22           0.2400         0.2300         0.2400         0.2367
  23           0.             0.             0.             0.
  24           0.5900         0.7100         0.5400         0.6133
  25           0.0400         0.0400         0.0300         0.0367
  26           0.2600         0.2500         0.2500         0.2533
  27           0.3900         0.3800         0.3900         0.3867
  28           0.3800         0.3900         0.3900         0.3867
  29           0.8500         0.8500         0.8500         0.8500
  30           0.8000         0.8000         0.7900         0.7967
  31           0.8300         0.8300         0.8300         0.8300
  32           0.9500         0.9500         0.9500         0.9500
  33           1.0000         1.0000         1.0200         1.0067
  34           0.5700         0.5700         0.5700         0.5700
  35           0.8100         0.8100         0.8100         0.8100
  36           0.6600         0.6600         0.6600         0.6600
  37           0.6900         0.6800         0.6900         0.6867
  38           0.7900         0.7900         0.7900         0.7900
  39           0.7000         0.7100         0.7100         0.7067
  40           0.6800         0.6700         0.6800         0.6767
  41           0.7400         0.7400         0.7300         0.7367
  42           0.6400         0.6400         0.6500         0.6433
  43           0.7100         0.7100         0.7000         0.7067
  44           0.8700         0.8900         0.8800         0.8800
  45           0.4600         0.4600         0.4600         0.4600
  46           0.3900         0.4000         0.3900         0.3933
  47           0.4700         0.4700         0.4700         0.4700
  48           0.1800         0.1800         0.1700         0.1767
  49           0.1000         0.1000         0.1100         0.1033
  50           0.0700         0.0600         0.0600         0.0633
  51           0.0300         0.0400         0.0300         0.0333
  52           0.0200         0.0200         0.0200         0.0200
  53           2.5500         2.5500         2.5400         2.5467
  54           1.6800         1.6900         1.6800         1.6833
  55           2.3200         2.3700         2.3600         2.3500
  56           0.2300         0.2300         0.2300         0.2300
  57           0.0600         0.0600         0.0600         0.0600
  58           0.             0.             0.             0.
  59           0.9500         2.0800         1.1500         1.3933
  60           2.1000         0.7100         1.2800         1.3633
  61           2.5400         1.6000         0.1800         1.4400
  62           0.             1.1900         2.5900         1.2600
  63           1.2800         0.5800         1.3100         1.0567
  64           0.4300         2.2700         1.1600         1.2867
  65           1.2500         0.2900         2.0300         1.1900
  66           2.3500         1.2800         0.3100         1.3133
  67           0.             1.6200         3.8500         1.8233
  68           1.2700         1.0600         1.8400         1.3900
  69           1.4400         1.3800         1.3700         1.3967
  70           1.3900         1.4600         1.4500         1.4333
  71           5.3800         5.3700         5.3800         5.3767
  72           1.3900         1.4000         1.4000         1.3967
  73           1.8600         1.8600         1.8600         1.8600
  74           4.8500         4.9200         4.8500         4.8733
  75           3.1700         3.1700         3.1900         3.1767
  76           1.5400         1.5400         1.5500         1.5433
  77           4.5800         4.5900         4.6200         4.5967
  78           3.0600         3.0800         3.0400         3.0600
  79           1.4200         1.4500         1.4400         1.4367
```

SAMPLE DATA OUTPUT (cont'd)

```
                 VOLTS - LINE TO NEUTRAL

LINE            SENSOR#            CFACTOR           VOLTS
1-N               1                47.4000          196.2360
2-N               2                47.4000          195.6040
3-N               3                47.4000          197.5000

                      AMPS - LINE

LINE            SENSOR#            CFACTOR           AMPS
1-N               4                96.9800          200.4253
2-N               5                96.9800          197.1927
3-N               6                96.9800          202.6882

                 KWATTS - LINE TO NEUTRAL

LINE            SENSOR#            CFACTOR           KWATTS
1-N               7                48.2900            5.9556
2-N               8                48.2900            7.0825
3-N               9                48.2900            6.7606

                               TOTAL KWATTS=         19.7989

                SENSOR#            CFACTOR
FREQUENCY(HERTZ)  10               166.6700          150.0030
ROTOR SPEED(RPM)  11               200.0000          408.6667
SHAFT TORQUE(NM)  12               299.3000          197.5380
F&W TORQUE(NM)=   12               299.3000            6.7173
ELECTRO-MAG TORQUE 12              299.3000          204.2553
DC LINK VOLTS     13                33.3333           87.7778
DC LINK AMPS      14               102.5641            0.

                      POWER OUTPUT

KW=                           8.7454
HP=                          11.7230
THRUST(NEWTONS)=            291.4601
EFFICIENCY(%)=               44.1711
POWER FACTOR(%)=             16.7882
KVA=                        117.9333
EFF X PF (PU)=                0.0742
SLIP(HERTZ)=                 75.0808

                      FORCE

POSITION        SENSOR#            CFACTOR           NEWTONS
   A              15               890.0000         -127.5667
   B              16               890.0000           38.5667
   C              17               890.0000          -17.8000
   D              18               890.0000         -180.9667
   E              19               550.0200          132.0048
   F              20               550.0200           91.6700
   G              21               558.0300          111.6060
   H              22               558.0300          132.0671
   I              23               458.3500            0.
   J              24               467.2500          331.0800

            REDUCTION OF SENSOR FORCES TO RESULTANT FORCES

RESULTANT OF TZA=              -438.6611
FORCE ANGLE OF RESULTANT=        -0.9774
LOCATION OF RESULTANT=            0.1221
RADIAL FORCE=                  -245.3054
TANGENTIAL THRUST=              363.6603
PITCH TO=                        41.8211
ROLL TO=                          0.2261
YAW TO=                         -25.4759
LATERAL FORCE=                   12.2437
```

SAMPLE DATA OUTPUT (cont'd)

```
                    FLUX DENSITY IN TESLA

POSITION   SENSOR#   CFACTOR    PEAK      CFACTOR    RMS
SLOT -1      25      0.0912     0.0033    0.0644     0.0024
SLOT  1      26      0.0912     0.0231    0.0644     0.0163
SLOT  3      27      0.0912     0.0353    0.0644     0.0249
SLOT  5      28      0.0912     0.0353    0.0644     0.0249
SLOT  7      29      0.0912     0.0775    0.0644     0.0547
SLOT  9      30      0.0912     0.0727    0.0644     0.0513
SLOT 11      31      0.0912     0.0757    0.0644     0.0534
SLOT 13      32      0.0912     0.0866    0.0644     0.0611
SLOT 15      33      0.0912     0.0918    0.0644     0.0648
SLOT 17      34      0.0912     0.0520    0.0644     0.0367
SLOT 19      35      0.0912     0.0739    0.0644     0.0521
SLOT 21      36      0.0912     0.0602    0.0644     0.0425
SLOT 23      37      0.0912     0.0626    0.0644     0.0442
SLOT 25      38      0.0912     0.0720    0.0644     0.0508
SLOT 27      39      0.0912     0.0644    0.0644     0.0455
SLOT 29      40      0.0912     0.0617    0.0644     0.0435
SLOT 31      41      0.0912     0.0672    0.0644     0.0474
SLOT 33      42      0.0912     0.0587    0.0644     0.0414
SLOT 35      43      0.0912     0.0644    0.0644     0.0455
SLOT 37      44      0.0912     0.0803    0.0644     0.0566
SLOT 39      45      0.0912     0.0420    0.0644     0.0296
SLOT 41      46      0.0912     0.0359    0.0644     0.0253
SLOT 43      47      0.0912     0.0429    0.0644     0.0302
SLOT 45      48      0.0912     0.0161    0.0644     0.0114
SLOT 47      49      0.0912     0.0094    0.0644     0.0066
SLOT 49      50      0.0912     0.0058    0.0644     0.0041
SLOT 51      51      0.0912     0.0030    0.0644     0.0021
SLOT 53      52      0.0912     0.0018    0.0644     0.0013
YOKE BELOW: SENSOR#  CFACTOR    PEAK      CFACTOR    RMS
SLOT 11      53      0.3650     0.9295    0.2570     0.6545
SLOT 22      54      0.3650     0.6144    0.2570     0.4326
SLOT 33      55      0.3650     0.8577    0.2570     0.6039
BUTT-LEAL    56      0.0912     0.0210    0.0644     0.0148
BUTT-TRAIL   57      0.1823     0.0109    0.1287     0.0077

                        MOTOR TEMP

 POSITION          SENSOR#             CFACTOR          CELESUA
(DRAWING AXXXXXX)
     1               59                21.3300          29.7198
     2               60                21.3300          29.0799
     3               61                21.3300          30.7152
     4               62                21.3300          26.8758
     5               63                21.3300          22.5367
     6               64                21.3300          27.4446
     7               65                21.3300          25.3827
     8               66                21.3300          26.0134
     9               67                21.3300          38.6917
    10               68                21.3300          29.6487
    11               69                21.3300          29.7909
    12               70                21.3300          30.5730

                        DC MOTOR

                   SENSOR#             CFACTOR
VOLTS                71                54.7000         294.1037
AMPS                 72                39.6667          55.4011
FLO AMPS             73                20.0400          37.2744

                        AC MOTOR

 POSITION          SENSOR#             CFACTOR          TAP VOLTS
(DRAWING AXXXXXX)
    13               74                32.0500          156.1903
    14               75                32.0500          101.8122
    15               76                32.0500           49.4638
    16               77                32.0500          147.3232
    17               78                32.0500           98.0730
    18               79                32.0500           46.0452

                   PHASE BELT VOLTAGES

PHASE              BELT               VOLTAGE %

                              V(X) = VOLTAGE VALUE AT SENSOR X

  A                  1        ((V(1)-V(74))/V(1))*100.      =   20.4069
  A                  2        ((V(74)-V(75))/V(1))*100.     =   27.7106
  A                  3        ((V(75)-V(76))/V(1))*100.     =   26.6762
  A                  4        ((V(76)/V(1))*100.            =   25.2063

  C                  1        ((V(77)-V(78))/V(3))*100.     =   24.9368
  C                  2        ((V(3)-V(77))/V(3))*100.      =   25.4060
  C                  3        ((V(78)-V(79))/V(3))*100.     =   26.3432
  C                  4        (V(79)/V(3))*100.             =   23.3140
```

and dc motor channels, and the phase belt voltages deleted. Only the dc link data has been allowed to remain, and these two lines should be ignored.

Friction and windage tests were made by plotting shaft torque as a function of speed with the linear machine unenergized. Line 1370 of the data reduction program was used to insert a reasonable model of the friction and windage curve obtained over the expected operating speed range. A linear approximation was found to be satisfactory over the 70% to 100% speed range usually tested.

The four vertical force sensors, A, B, C, and D were arranged electronically to produce a 5 V signal for the data scanner when the stator was unenergized and no external forces were imposed on it. This offset was necessary in order to allow measurement of both attractive and repulsive forces. The offset was removed in line 1800 of the data reduction program, before the multiplier of 890 N/V was applied.

All data presented is based on the three-sample average. Thrust (hence output power and efficiency) is based on the shaft torque transducer rather than the force yoke so that it is also averaged by the considerable inertia of the wheel. Radial force and tangential thrust are calculated from the sensor outputs by the force resolution method described in Section 5. Pitch torque, except where indicated, has not been processed through the force resolution. The calculated radial force corresponds to normal force in the straight (flat) motor subject to the conditions discussed in Section 5. Individual force sensor readings have no separate meaning as they are always utilized in pairs. See Section 5 for treatment of the force data and a discussion of its validity.

In the earlier stages of testing of the machine, the data acquisition equipment and the data reduction program were arranged to calculate the flux densities in the stator for sine wave signals. A voltage at the flux coil was amplified and put through a converter to produce a dc voltage equal to the true rms of the incoming signal. A simple integration of this voltage, amounting to dividing by frequency, was performed in the data reduction program. Around Run #519, all of the flux sensing channels were pulled apart for modification. Beginning with Run #527, the modified channels were in operation. The modifications included the addition of an RC low-pass filter to the flux channels to provide an electronic integration of the flux signal. The amplifier gains were changed, and the data reduction program was modified to suit.

Flux densities printed out for 60 Hz sine wave data, up to Run #148, are correct. From Run #172 through Run #526, all of the flux density data (obtained with square wave current on the stator) should be ignored. For all runs including and after #527, the flux densities reported over the slots are correct. The yoke densities printed out as Channels #53, 54, 55 should be multiplied by 0.305 to get correct values, while the leading edge density, #56, should be multiplied by 0.721, the trailing edge by 0.742. These last five channels were modified in the same manner as the channels for the slots, but the proper conversion factors were not initially applied for the differing areas and numbers of turns in the coils.

It should be noted that representative data at 60 and 150 Hz were taken after the flux channels were modified. G-table data were not repeated, as flux densities were not considered to be critical data in these tests.

Catalogue of Test Data

The following is a catalog of all runs used in the analysis presented in this report. It is to be used in referring to the actual copies of the runs contained in Appendix A. A number of runs are not included, either because their results were unsatisfactory or because the numbers were not, in fact, used. In most cases, these conditions are noted. The gaps in the 60 Hz sine wave data are a result of the debugging work that was under way during those tests.

CATALOG

60 Hz Sine Wave Data

33, 38-41, 43-46	60 Hz, 50 V Slip Curve
48-54, 56, 58	60 Hz, 70 V Slip Curve
60-68	60 Hz, 90 V Slip Curve
70-78	60 Hz, 110 V Slip Curve
80-89	60 Hz, Magnetizing Curve
92-98	60 Hz, 24% Slip Curve
101-109	60 Hz, 240 A Slip Curve
127-135	60 Hz, Fourth Quadrant
146-148	60 Hz, Locked Rotor

Square Wave Data with CCI

172-180	60 Hz, Magnetizing Curve
181-189	60 Hz, 24% Slip Linearity
(190-233)	60 Hz (Deleted Tests)
234-240	60 Hz, 23.3 mm Air Gap
(241 Deleted)	
242-247	60 Hz, 13.1 mm Air Gap
248-250	60 Hz, 13.1 mm Air Gap
(251-262)	60 Hz (Deleted Data)
263-289	60 Hz, Lateral Offsets
290-294	60 Hz, Yaw Angles - Bad Force Data

CATALOG (Cont'd)

295-315	60 Hz, Yaw Angles
316-323	60 Hz, Pitch Angles
324-347	60 Hz, Roll Angles
(348-387)	60 Hz (Deleted Data)
(388-415)	150 Hz (Deleted Data)
416-422	150 Hz, 325 A Slip Curve
423-429	150 Hz, 200 A Slip Curve
430-436	150 Hz, 250 A Slip Curve
437-446	150 Hz, 24% Slip Linearity

Square Wave Data with CCI (Cont'd)

447-453	150 Hz, 23.3 mm Air Gap
454-460	150 Hz, 13.1 mm Air Gap
461-464	150 Hz, Normal Air Gap
465-480	150 Hz, Lateral Offsets
481-483	60 Hz Retests
(484 - Not used)	
485-494	150 Hz, Yaw Angles
495-502	60 Hz, Check and High Slip
503-510	150 Hz, Yaw Angles
511-526	150 Hz, Roll Angles

(Flux Sensors Modified)

527-535	60 Hz, Magnetizing Curve
536-544	150 Hz, Magnetizing Curve
545-555	150 Hz, 24% Slip Linearity
556-564	150 Hz, 300 A Slip Curve
565-567	150 Hz, 200 A Slip Curve
568-570	150 Hz, 250 A Slip Curve
571-573	150 Hz, 325 A Slip Curve
574-583	60 Hz, 24% Slip Linearity
(584 - Not used)	
585-593	60 Hz, 275 A Slip Curve
594-605	150 Hz, Pitch Angles
606	60 Hz, Locked Rotor
(607 - Not used)	

CATALOG (Cont'd)

608-618	200 Hz, 300 A Slip Curve
619-629	250 Hz, 300 A Slip Curve
(630-638)	300 Hz, (Deleted Data)
639-647	332 Hz, Slip and Linearity
648-660	365 Hz, Slip and Linearity
661-682	365 Hz, Large and Small Air Gap
(683-686)	365 Hz (Deleted Data)
687-715	300 Hz, Lateral Offsets
716-718	365 Hz, Slip Curve, Retest

(Flux Sensors Modified) (Cont'd)

719-734	300 Hz, Yaw Angles
735-740	300 Hz, Large Gap
741-746	300 Hz, Small Gap
747-750	300 Hz, Standard Gap
751-766	300 Hz, Roll Angles
767-774	300 Hz, Pitch Angles
775-784	300 Hz, Slip Curve
785-787	150 Hz, High Slip
788-790	60 Hz, High Slip
791-794	150 Hz, Fourth Quadrant
(795-798 - Not used)	
799-801	150 Hz, High Slip, Retest

Section 3

INTERPRETATION OF "G-MATRIX" TEST DATA

GENERAL DISCUSSION

Figure 3-1 shows the assumed axes and their directions as used in the "G-Table" tests on the SLIM. Table 3-1 lists the displacements and angles tested in each of the five categories of vertical, lateral, roll, yaw, and pitch. These are values arrived at through interpretation of the contract and investigation of the limits of the test equipment.

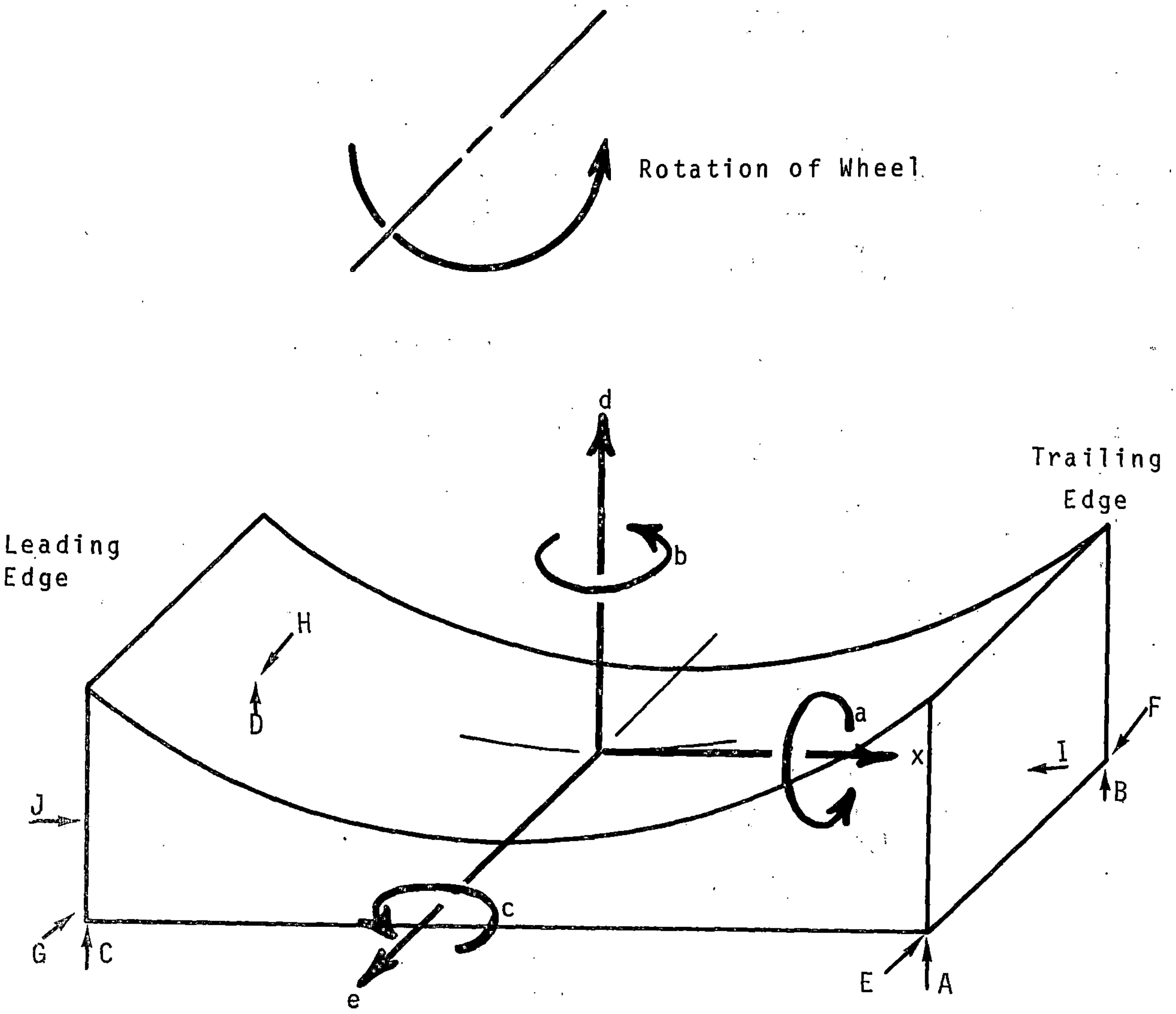

a = roll
b = yaw
c = pitch
x = direction of wheel travel
d = vertical displacement (air gap)
e = lateral displacement

FIGURE 3-1. DEFINITIONS OF DIRECTIONS FOR "G-MATRIX" TESTS.

TABLE 3-1. "G-TABLE" PARAMETERS TESTED

A. Vertical: (nominal d = 18.2 mm)
d' = 13.1 mm (d-5.1 mm)
d" = 23.3 mm (d+5.1 mm)

B. Lateral: e' = 12.5 mm
e" = 25 mm

C. Roll: a' (0.00148 rad)
  2.1 mm tilt between rails
  1/4 mm tilt across width of stator
a" (0.00296 rad)
  4.2 mm tilt between rails
  1/2 mm tilt across width of stator

D. Yaw: b' (0.0224 rad)
  ±12.5 mm across length of machine (total 25 mm)
b" (0.0448 rad)
  ± mm across length of machine (total 50 mm)

E. Pitch: c' (+0.00456 rad)
  +5 mm across length of machine
  largest gap at leading end
c" (-0.00456 rad)
  -5 mm across length of machine
  largest gap at trailing end

Tests were run at currents and loads corresponding to 10%, 40%, and 100% rating, at 24% slip. This slip was chosen as a likely operating point for the machine in view of its performance in earlier tests. The square wave current inverter was used as the power supply for these tests.

Some difficulty was experienced in obtaining meaningful data from the lateral force sensors in the test equipment. The electromagnetic forces acting on the stator in a lateral direction were of the order of 0.1% of its weight, and frictional dead band effects were noted in the sensor readings. Initially there was about 0.04 mm clearance between each of the four lateral sensors and the stator support structure. Calibration of these sensors with a spring dial scale and a lever extension on the stator revealed about a 45 N dead band.

The sensors were moved inward so as to provide a slight preload, and another calibration revealed that the dead band was reduced to an almost undetectable level. This arrangement, with calibration from 0 to 80 N on each sensor pair, was used in the tests presented here. The data still shows a good deal of mechanical "noise," and some interpretation and adjustment of the data is shown in these figures.

The data as reduced by the data reduction computer program are presented for lateral offsets and for yaw angle offsets. Each of these curves was adjusted, point by point, to pass near or through zero at zero current. The curve for a "+" displacement was then averaged with the negative of the one for a "-" displacement. This is the curve which appears on the figures called "adjusted."

Mechanical and mathematical adjustments to the system were not completely successful, and it is not obvious that the type of support structure used in this test setup is able to produce really meaningful data at the low force levels encountered. The lateral forces and torques produced for the conditions tested are apparently of the same magnitude as the frictional forces in the test setup.

60-HERTZ TESTS

Vertical Displacements

The stator of the SLIM was positioned under the wheel on shims of 15.2 (normal) 10.1, and 20.3 mm thickness in order to produce air gaps of 18.2 (normal), 23.3, and 13.1 mm, respectively. Data obtained on voltage, current, thrust, attraction, pitch torque, efficiency, and power factor for these conditions is presented in Figures 3-2 through 3-7.

It may be noted from Figures 3-2, 3-3, and 3-4 that the ratio of normal force to thrust and of pitch torque to thrust is approximately constant over the range of air gaps tested. As expected, more torque per $(\text{amperes})^2$ was obtained at the reduced air gap, less at the increased one. The voltage required from the inverter to produce a given current varied only a little over the range of gaps tested, appearing to increase with increased gap at low load levels and to decrease at higher load levels. Figure 3-5 shows the data obtained for this case, and indicates the small size of the variation.

Another effect expected from change of air gap was a change of efficiency and power factor (true rms V-A/W). In Figures 3-6 and 3-7, these parameters are plotted against air gap at the various loads tested. Reduction of the air gap increases both efficiency and power factor, while an increase of the gap reduces both.

Lateral Displacements

Figures 3-8 and 3-10 present the yaw torque and lateral force data obtained by displacing the stator sideways by $e = 0, \pm 12.5,$

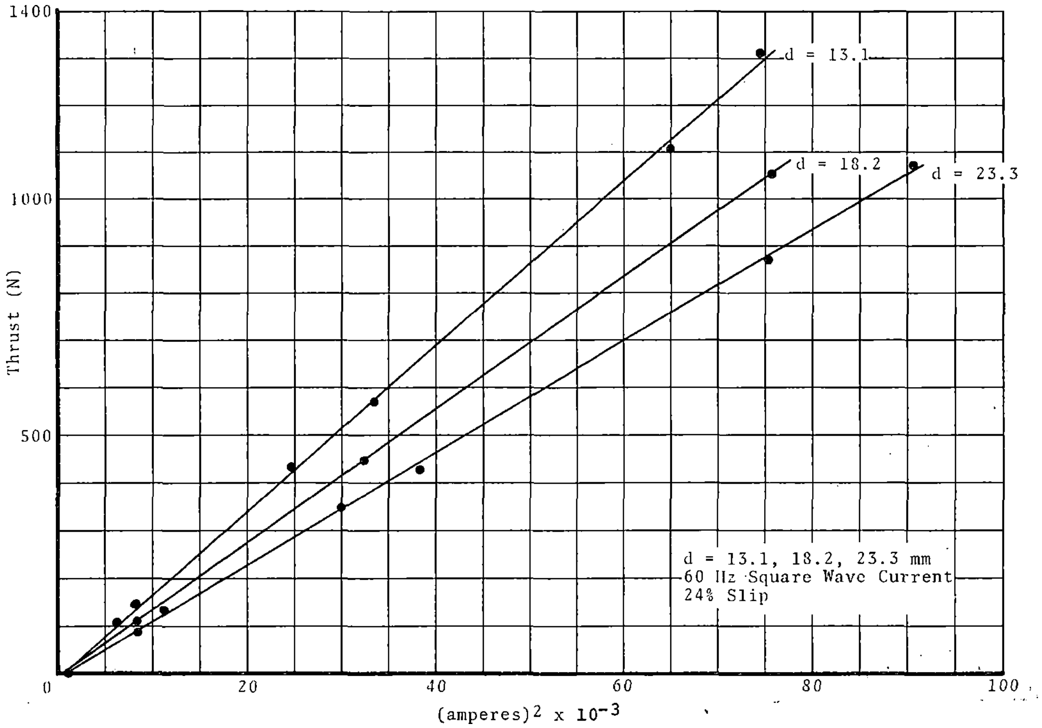

FIGURE 3-2. THRUST VS. (CURRENT)^2.

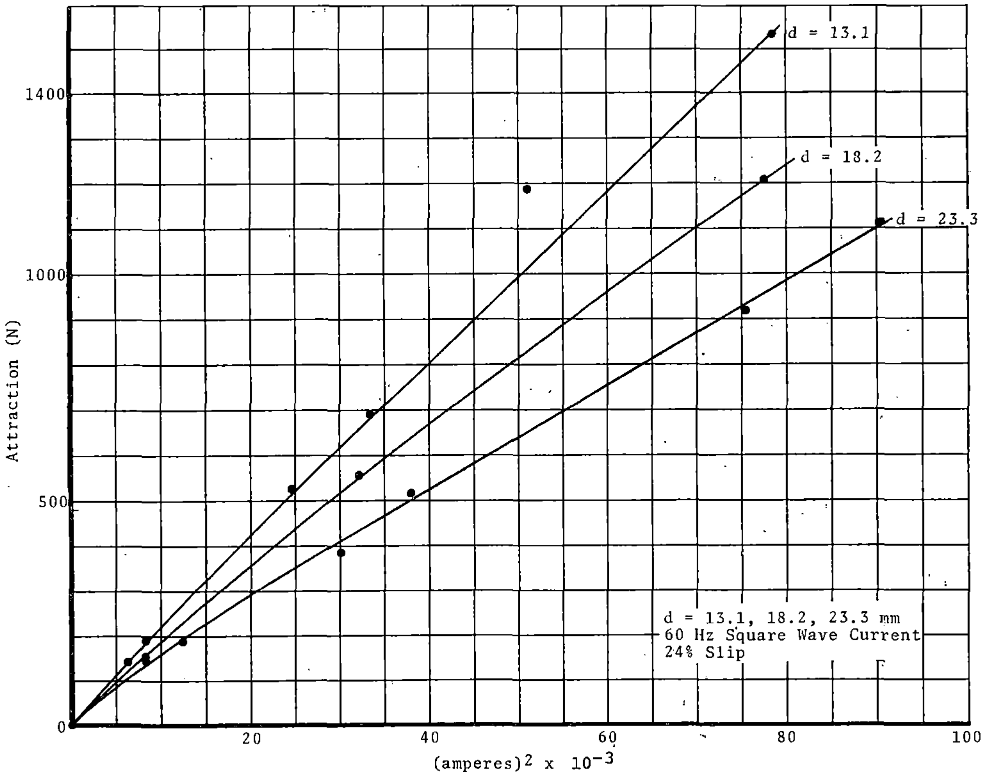

FIGURE 3-3. ATTRACTION (RADIAL FORCE) VS. (CURRENT)^2.

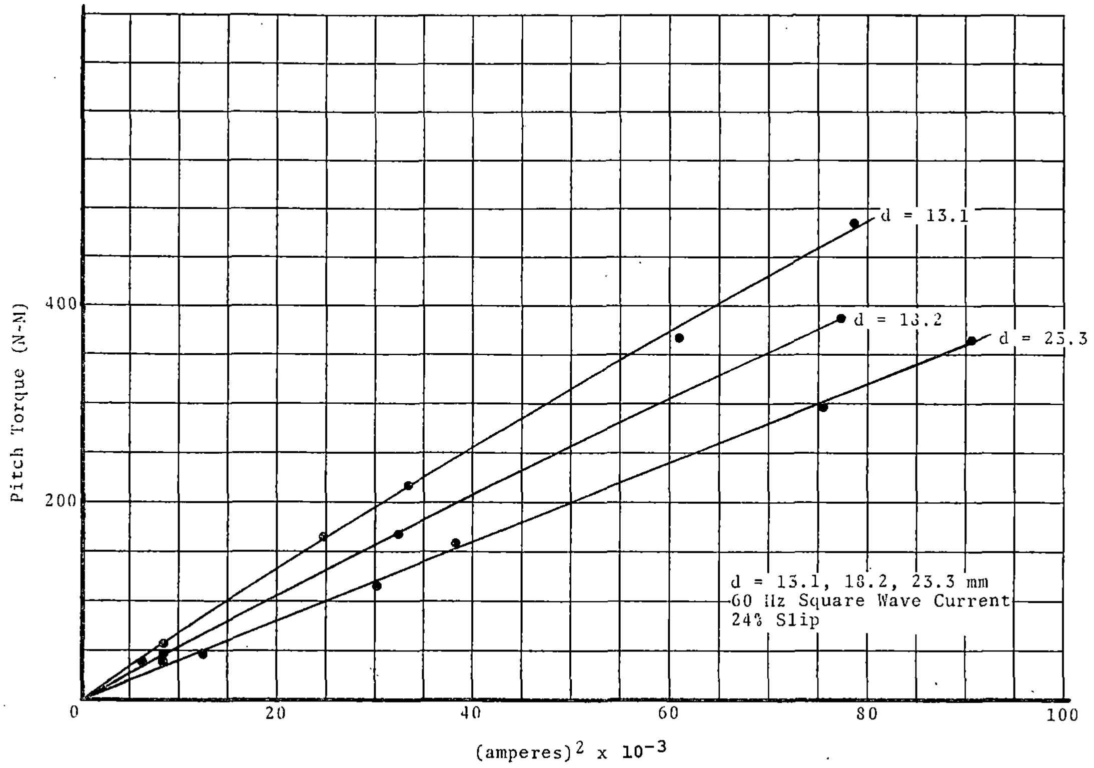

FIGURE 3-4. PITCH TORQUE VS. (CURRENT)^2.

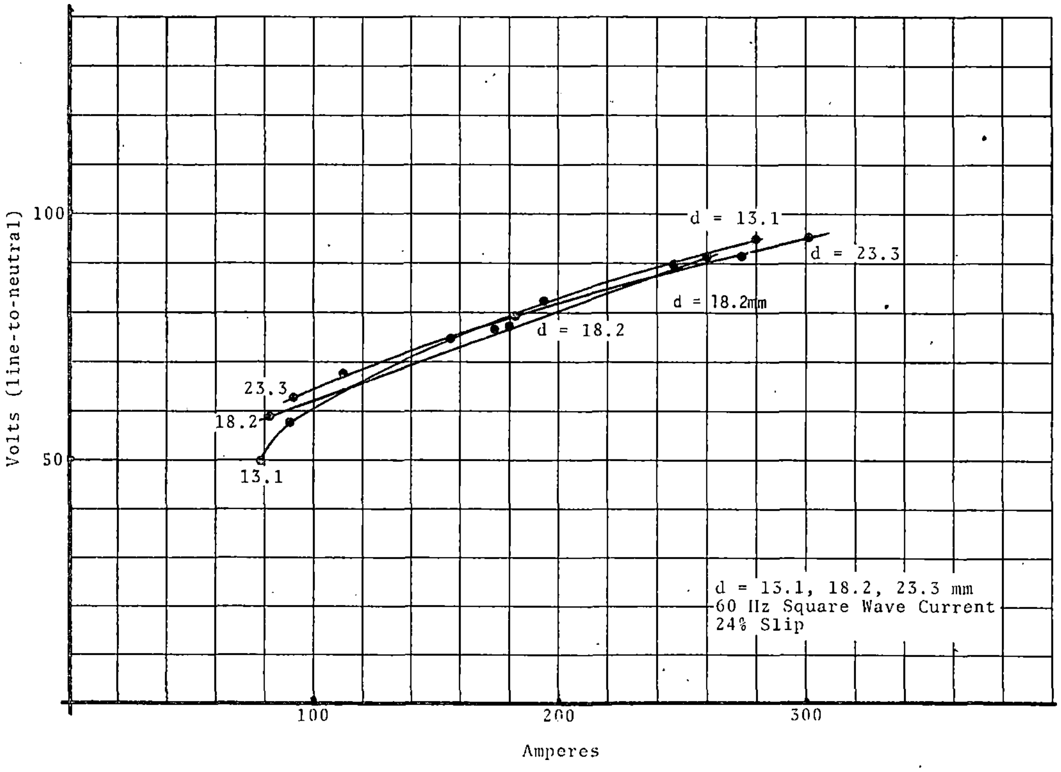

FIGURE 3-5. OBSERVED VOLTAGE VS. CURRENT.

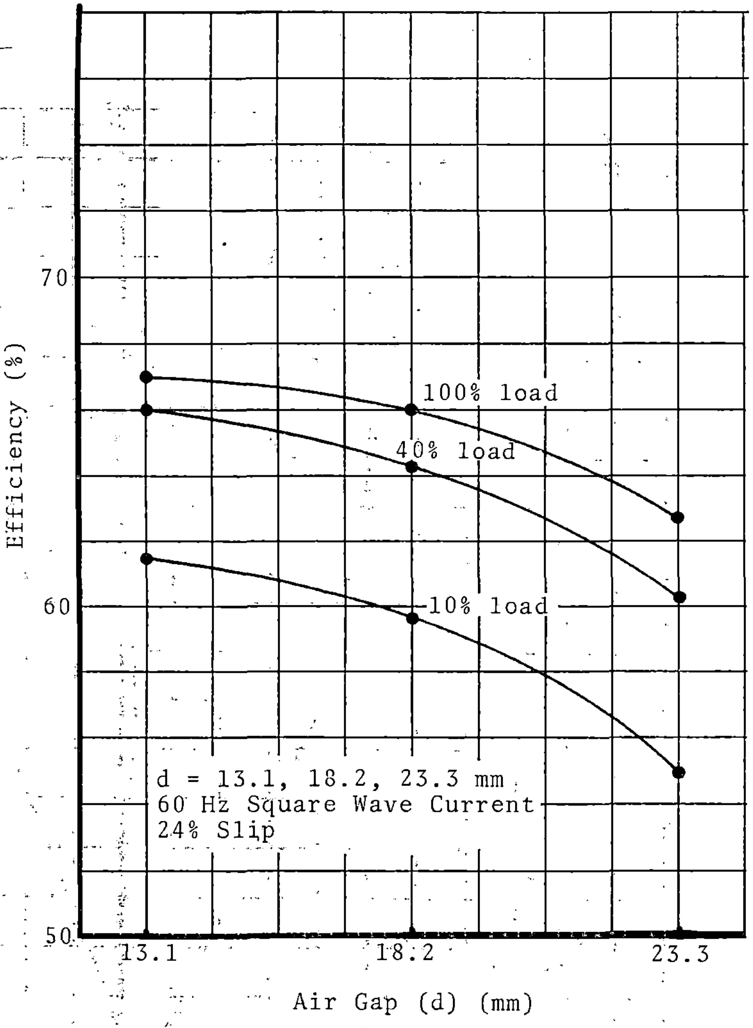

FIGURE 3-6. EFFICIENCY VS. AIR GAP.

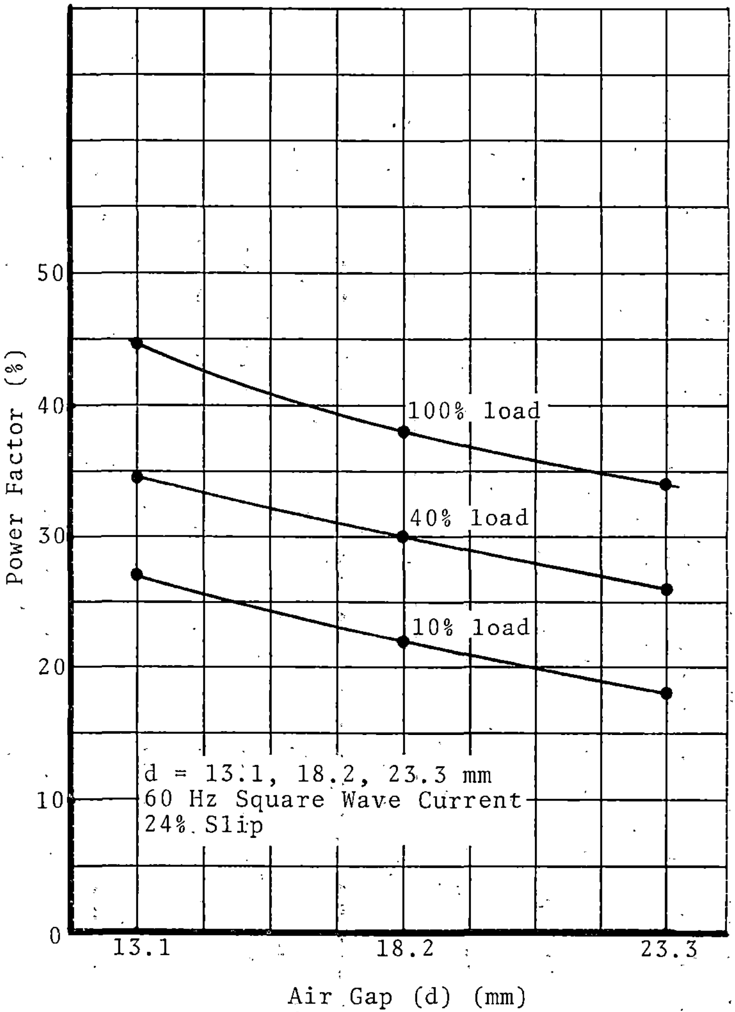

FIGURE 3-7. APPARENT POWER FACTOR VS. AIR GAP.

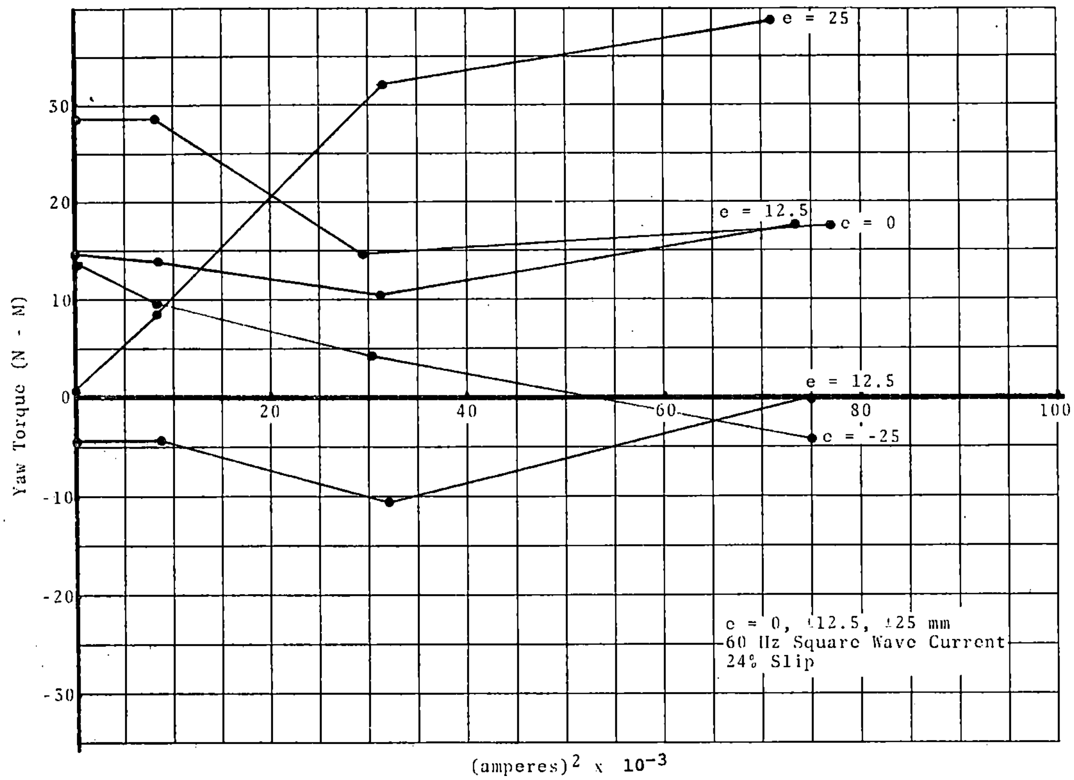

FIGURE 3-8. YAW TORQUE VS. (CURRENT)^2.

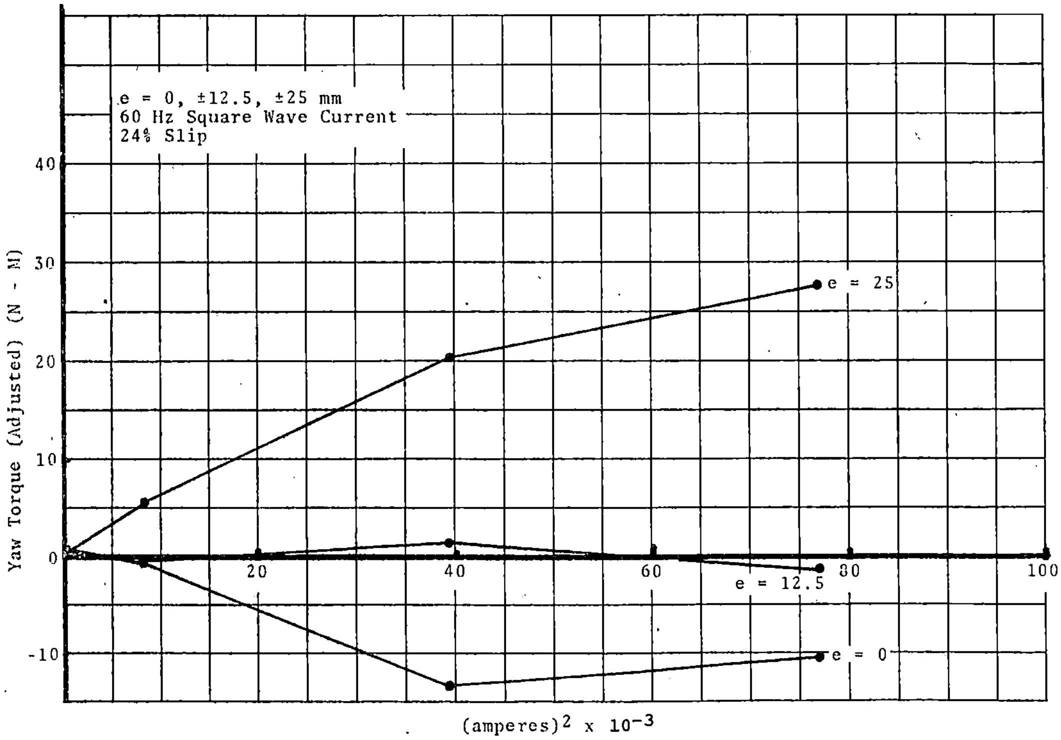

FIGURE 3-9. YAW TORQUE (ADJUSTED) VS. (CURRENT)^2.

and ± 25mm. A brief inspection of the curves in these figures will indicate the difficulty of obtaining meaningful data as mentioned earlier. Only the curves for e ∓ ± 25 seem to agree from "+" to "-". It should be remembered that the displacements made are approximately equal to the air gap of the machine, and hence might not be expected to produce large forces. The largest forces observed, in fact, are about 2 to 4% of the thrust and normal forces. The fact that these forces and torques are as small as this is, in itself, a significant finding, but it is appropriate to try to get as much as possible from the data.

Figures 3-9 and 3-11 are the results of adjusting the data as previously described. Note that the zero displacement curve wanders quite a bit, providing some indication of the reliability of the data. Only the e = 25mm curves show any believable trend in both lateral force and torque.

It is interesting to interpret the magnitudes and signs of these forces and torques in terms of what they mean to this short model machine. At 25 mm displacement and reasonable load (50 to 100%), the lateral force is negative. That is, it acts to restore the stator to its position under the wheel. The yaw torque, however, is positive and has the effect of centering the trailing portion of the stator while increasing the offset of the leading portion. In fact, under load conditions where the leading portion of the machine is levitated or has a negative force of attraction, the net force recorded by the leading end lateral sensors is positive, or tending to increase the lateral displacement. The forces of attraction and repulsion in the machine are exactly those of unlike and like magnetic poles. Attraction, where it occurs, acts in every direction, and repulsion does likewise.

No effects of lateral displacements were noted on efficiency or on thrust per amperes squared. The power factor of the machine appears to suffer by about 1-1/2% when at the maximum (25 mm) offset.

Roll Angle Displacements

The stator assembly was tilted to both sides by two different angles, and lateral alignment of the stator iron with the wheel iron was maintained as closely as possible. Angles of roll tested were a = 0, ±0.00148 and ±0.00296 rad.

Data obtained from these tests showed no consistent effect on any of the force sensors nor on thrust per amperes squared, efficiency nor power factor. The larger roll angles correspond to a difference of ± 1.4% of air gap across the stack of the machine. Apparently this difference is too small to produce detectable changes in performance or detectable forces in the test fixture.

Yaw Angle Displacements

Figures 3-12 and 3-14 present the torque and force data obtained in testing the SLIM under yaw conditions. The angles of

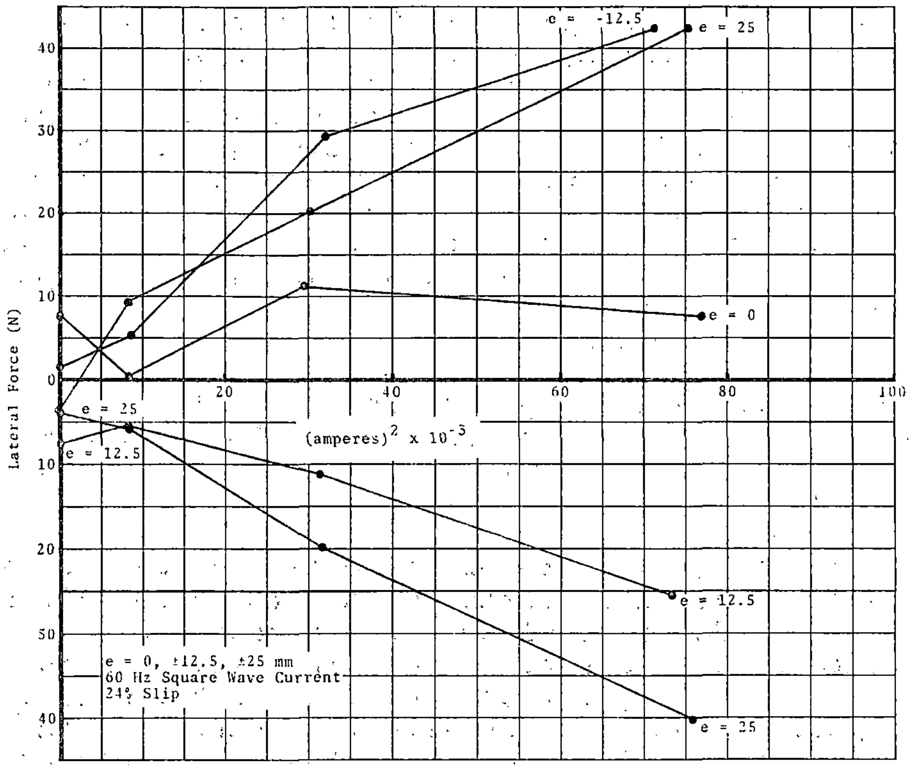

FIGURE 3-10. LATERAL FORCE VS. (CURRENT)^2.

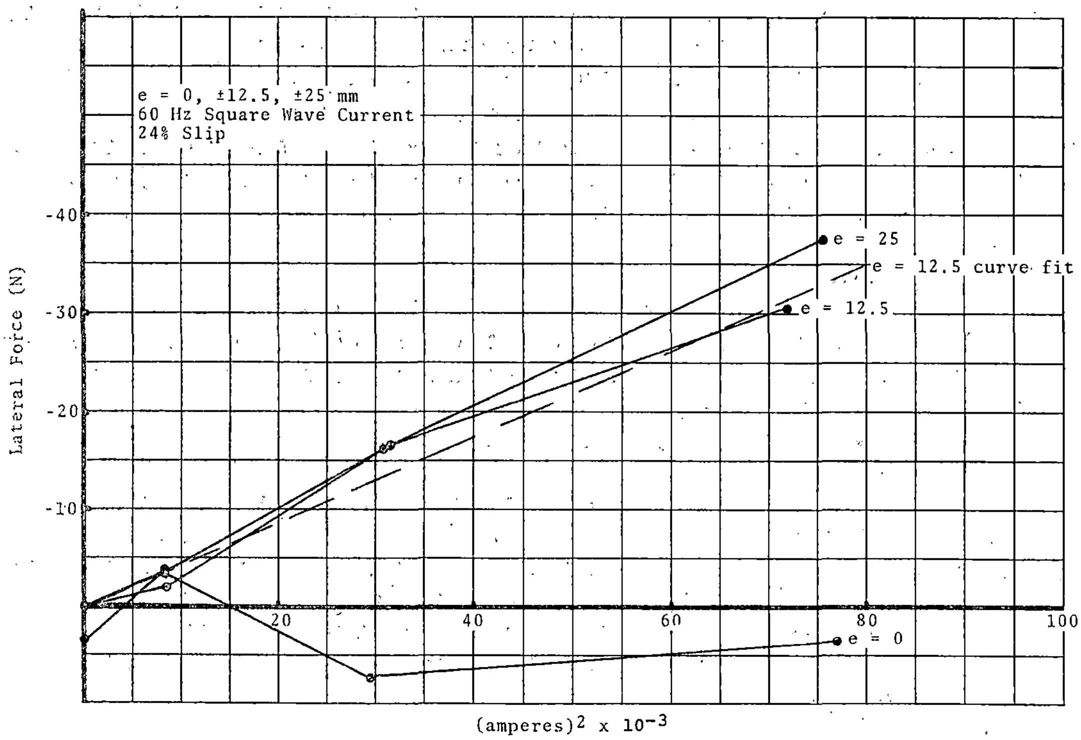

FIGURE 3-11. LATERAL FORCE (ADJUSTED) VS. (CURRENT)^2.

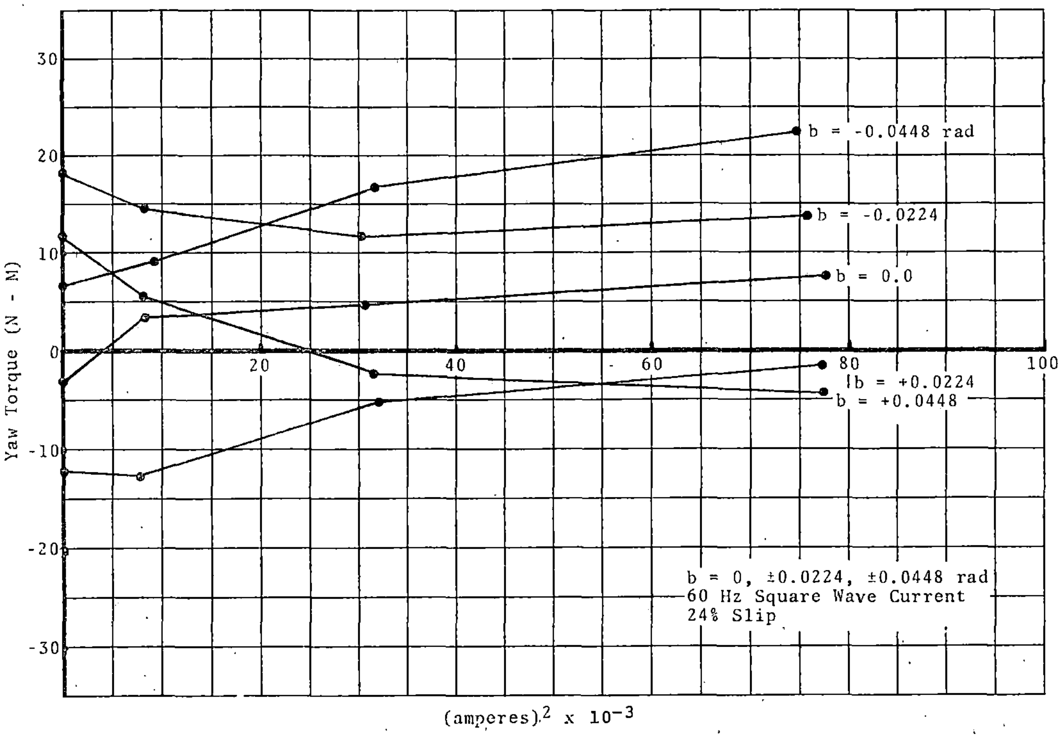

FIGURE 3-12. YAW TORQUE VS. (CURRENT)^2.

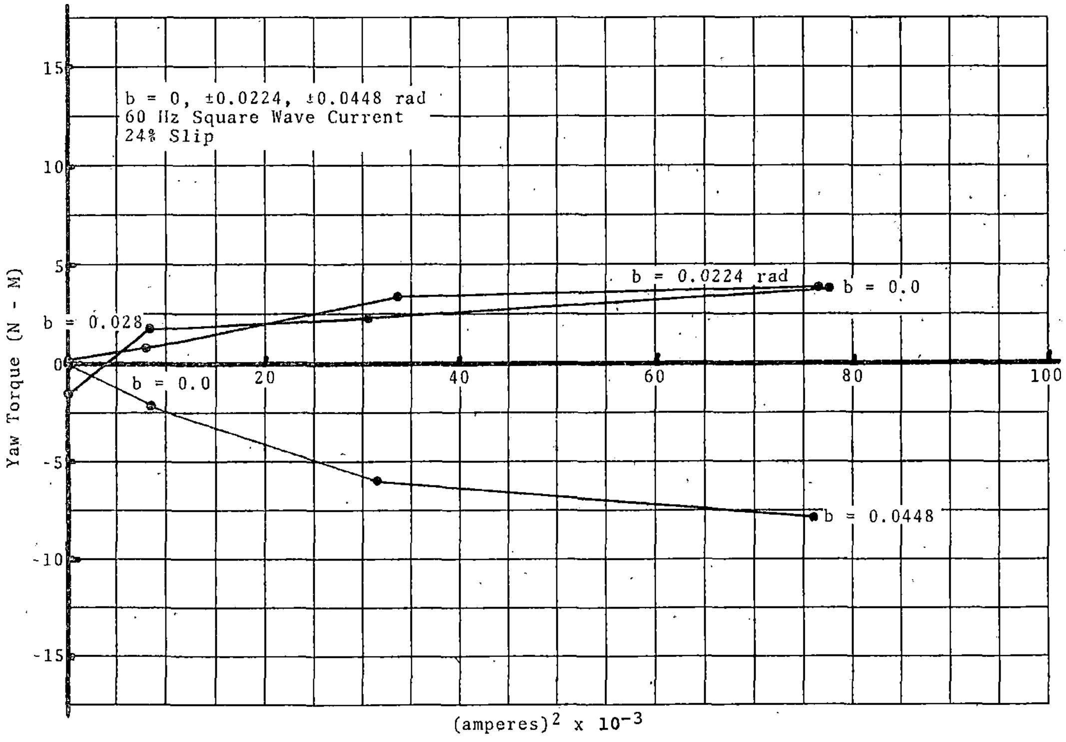

FIGURE 3-13. YAW TORQUE (ADJUSTED) VS. (CURRENT)^2.

b = 0, ± 0.0224, and ± 0.0448 rad were chosen, not because they reflected the rail-truck data in the contract, but because they might be large enough to produce meaningful forces. The ± 0.0448 rad yaw brings the corners of the stator flux instrumentation as near the wheel as can be allowed.

Even with the relatively large angles used, producing ± 25 mm of displacement at the ends of the stators, only small forces and torques were detected. In the adjusted curves of Figures 3-13 and 3-15, only the 0.0448 rad data seems to make sense. Here a negative yaw torque is acting to restore the stator to its proper alignment, and a positive lateral force is acting to pull the trailing end back under the wheel. These two effects can be explained by the attraction of the rear portion of the stator to the wheel iron.

The values and senses of the force and torque for 0.0224 rad yaw do not appear to be consistent, and are probably lost in the mechanical noise of the stator support structure.

No effect of yaw angle displacement on thrust, nor on power factor or efficiency, was noted. Apparently, a greater displacement, probably several times the machine air gap, would be required to produce a noticeable change.

Pitch Angle Displacements

Only one set of pitch-changing shims was utilized in the tests of the SLIM. These provided c = 0, +0.00456, and -0.00456 rad pitch angles. The data obtained on pitch torque variation is presented in Figure 3-16 and is fairly consistent.

The change in pitch torque is such as to produce a positive feedback, or unstable, situation. An increase in the air gap at the leading end (positive pitch) produces an increased pitch torque, which would further increase the gap at the lead end.

No effects were observed in these tests on any other force sensors, on torque per amperes squared, nor on efficiency and power factor.

Figure 3-17 compares the flux distribution in the air gap of the machine under the three pitch conditions tested. The flux density might be expected to show a skewing toward the end of the machine with the smaller airgap, but the plot shows no such trend. Either the amount of pitch is insufficient to show the effect, or the mere magnitude of flux at a location is not sufficient information to show all that occurs. The slight difference in flux density magnitude showing near the ends of the machine is reflected in the small variations in thrust from run to run. This variation is presented here without explanation.

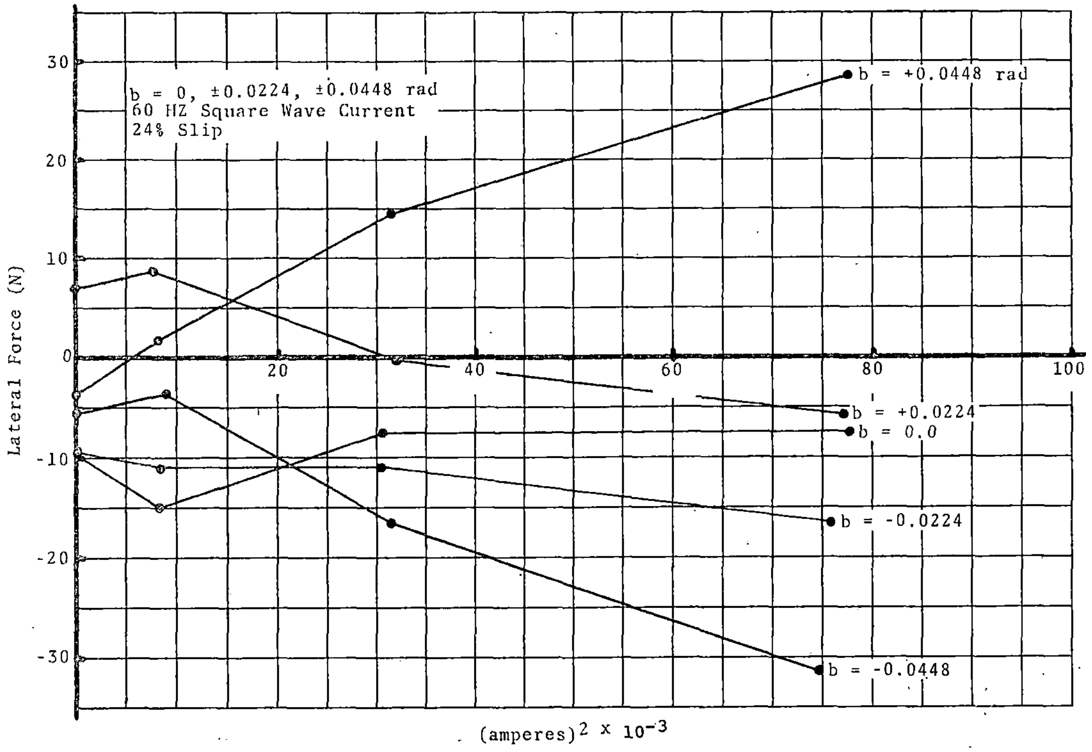

FIGURE 3-14. LATERAL FORCE VS. (CURRENT)^2.

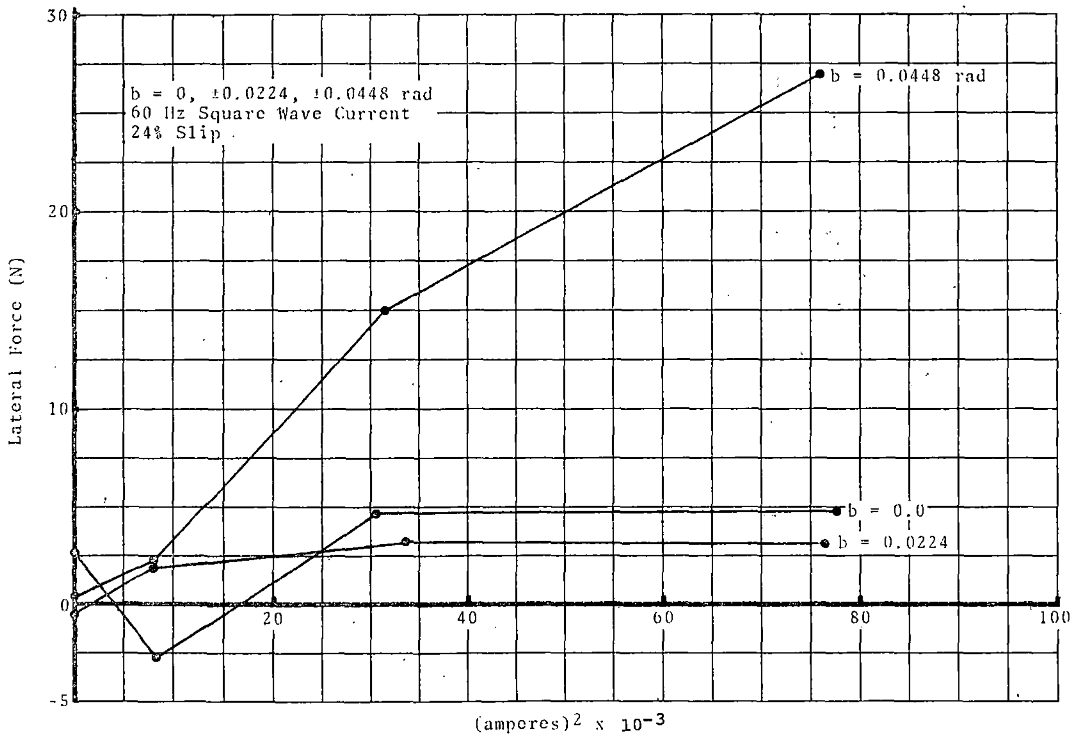

FIGURE 3-15. LATERAL FORCE (ADJUSTED) VS. (CURRENT)^2.

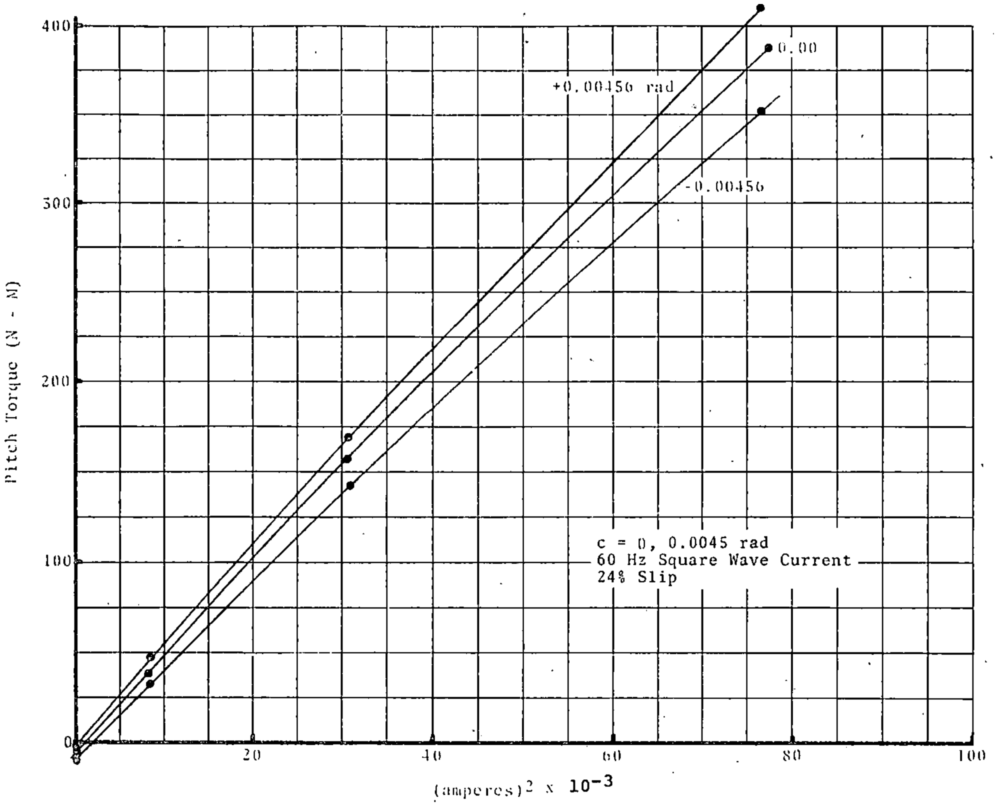

FIGURE 3-16. PITCH TORQUE VS. (CURRENT)^2.

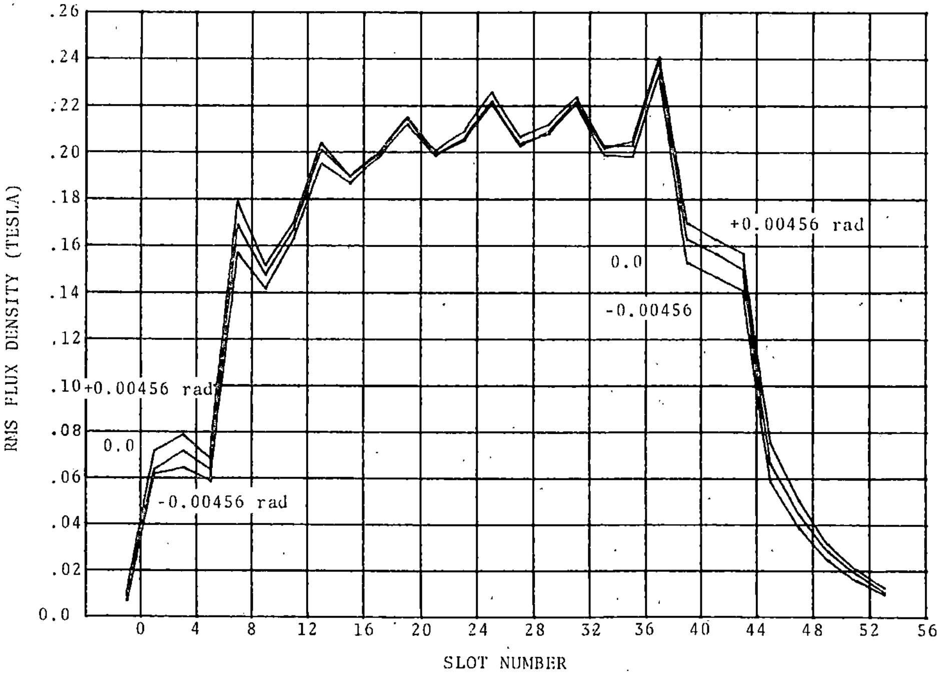

FIGURE 3-17. FLUX DENSITY IN GAP
FOR c = 0, ± 0.00456 rad
60 Hz SQUARE WAVE CURRENT
24% SLIP.

150-HERTZ TESTS

Vertical Displacements

Figures 3-18, 3-19 and 3-20 show the effect of increase or decrease of the air gap dimension on thrust radial force and pitch torque. All are increased by reduction of the gap and decreased by enlargement of the gap. The direction of the effects, as well as the magnitude of the effects, is similar to the 60 Hz case. It must be noted, of course, that the radial force is negative over these operating conditions.

Some scattering of the data on radial force occurred in the lower-to-middle range of currents, but the lines were plotted to reflect the overall trend of the data, with more trust put in the high current (high force) data. Pitch torque data suffered similarly at low levels, and, again, the curves reflect the best compromise.

The rms voltage at the terminals of the machine increased slightly with increasing air gap of the machine, as shown by Figure 3-21. Figure 3-22, which shows the efficiency of the machine at various loads for the three air gaps, does not make very much sense. Efficiency calculations from tests of the machine are questionable because the "watts" signal in the data acquisition system is at a rather low-voltage level. Prior to the testing of the synchronous machine, this problem will be corrected. The power factor data, however, showed the same trend as at 60 Hz, namely, the expected increase with increasing load and decreasing air gap (Figure 3-23).

Lateral Displacements

Figures 3-24 and 3-26 present the yaw torque and lateral force from displacements of the stator sideways by e = 0, ± 12.5 and ± 25 mm. Again, as at 60 Hz, the magnitudes of forces and torques were small, and the data was adjusted. The adjusted curves are shown in Figures 3-25 and 3-27.

The yaw torque shows an increasing positive value for increasing current levels with positive displacement. The data at e = 0 is confusing because the magnitude of yaw torque is greater for no displacement than for the larger of the two offsets. Positive yaw torque for the actual displacements, however, is easily explained by the large repulsive force at the leading end of the stator and the much less repulsive force at the trailing end. It does not matter, in the production of torque in this sense, whether the trailing end force is attractive or repulsive, so long as it is less repulsive than the leading end force.

The lateral force is also positive for positive displacements, as would be expected from the net levitational, or repulsive, force between the stator and track. The forces shown in Figure 3-27 are, in a sense, to increase the displacement, and no guidance effects

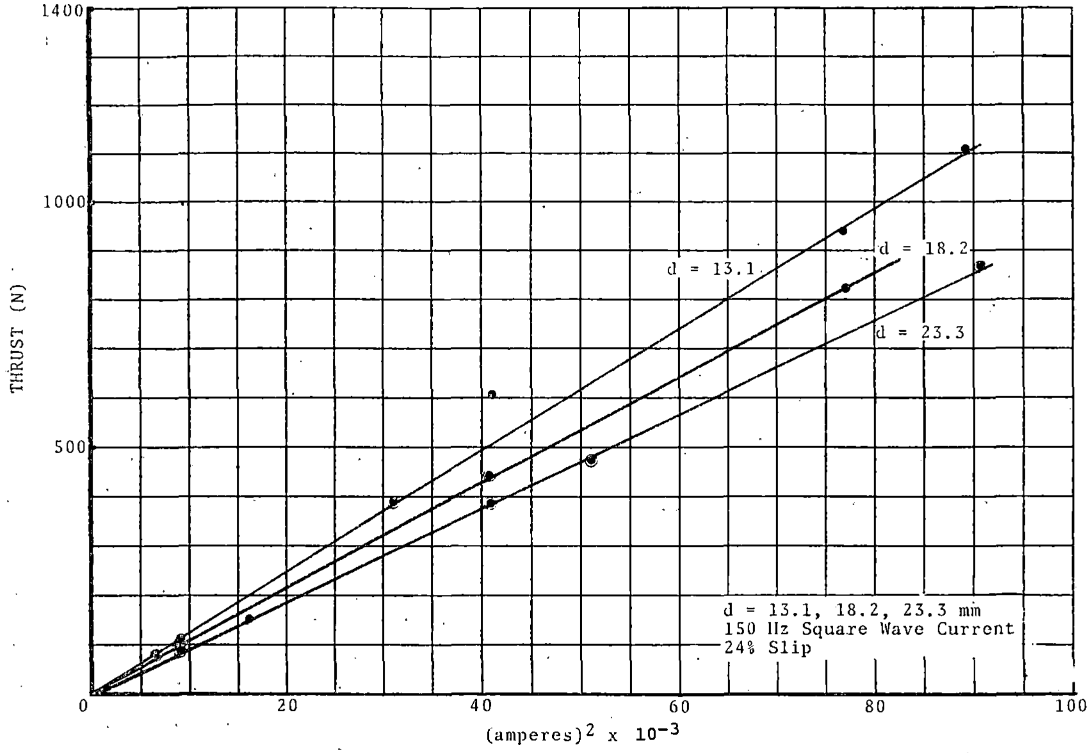

FIGURE 3-18. THRUST VS. (CURRENT)^2.

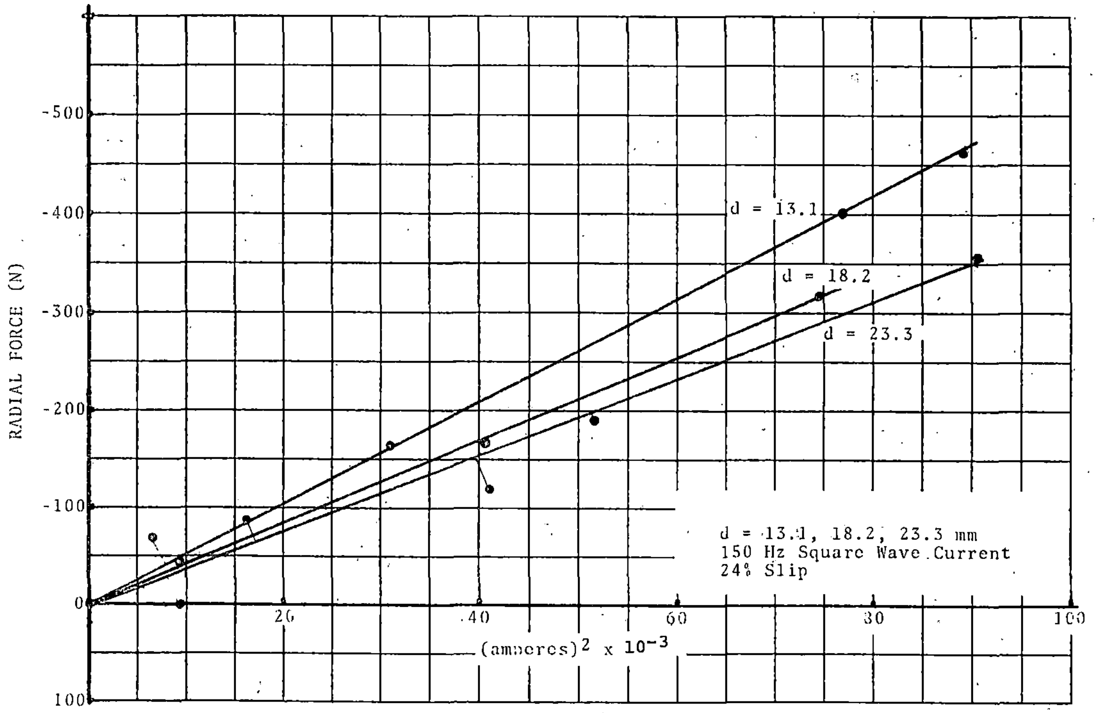

FIGURE 3-19. RADIAL FORCE (ATTRACTION) VS. (CURRENT)^2.

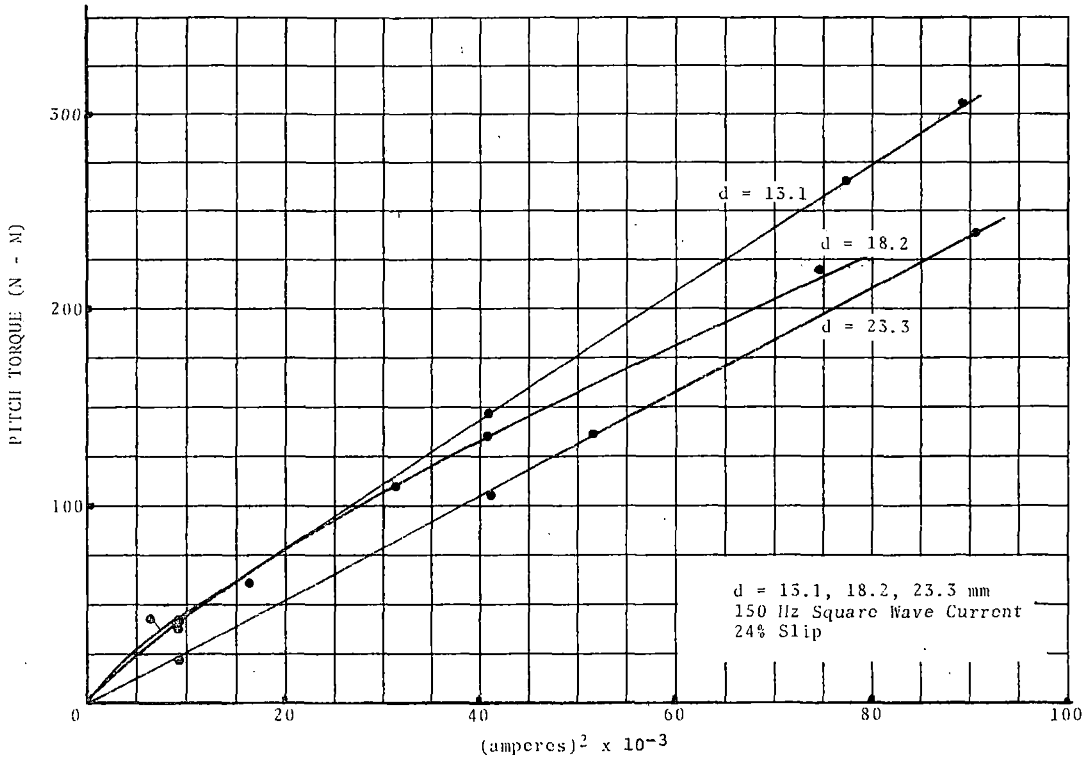

FIGURE 3-20. PITCH TORQUE VS. (CURRENT)^2.

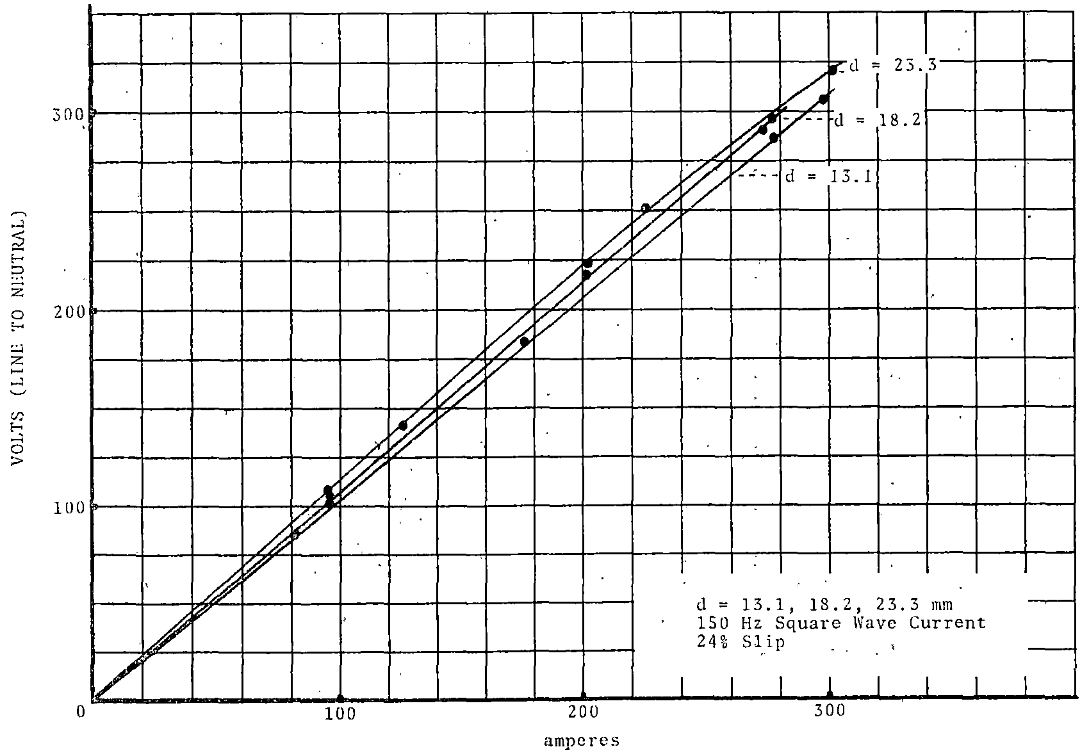

FIGURE 3-21. RMS VOLTAGE VS. CURRENT.

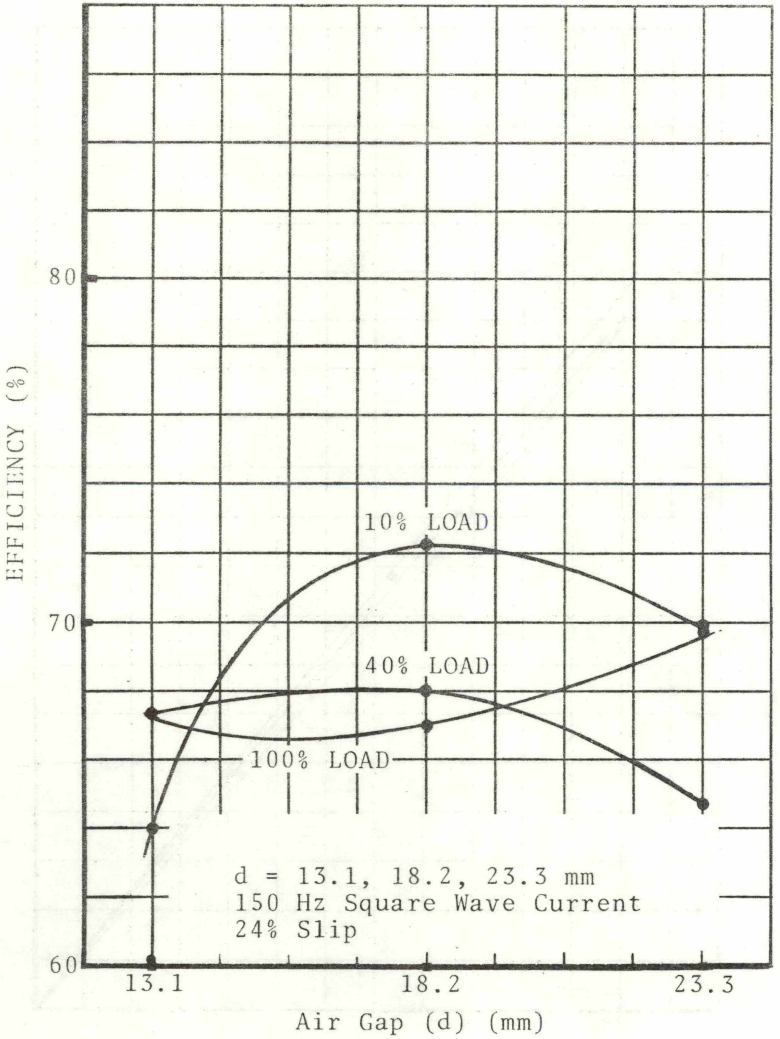

FIGURE 3-22. EFFICIENCY VS. AIR GAP.

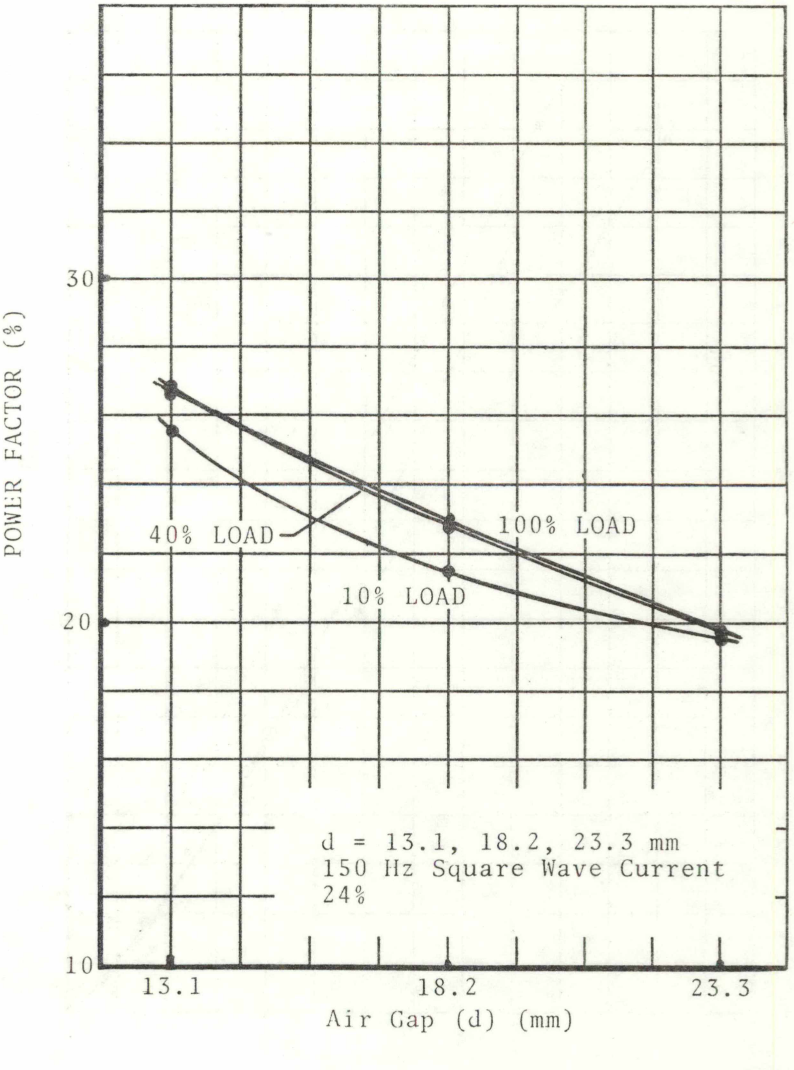

FIGURE 3-23. APPARENT POWER FACTOR VS. AIR GAP.

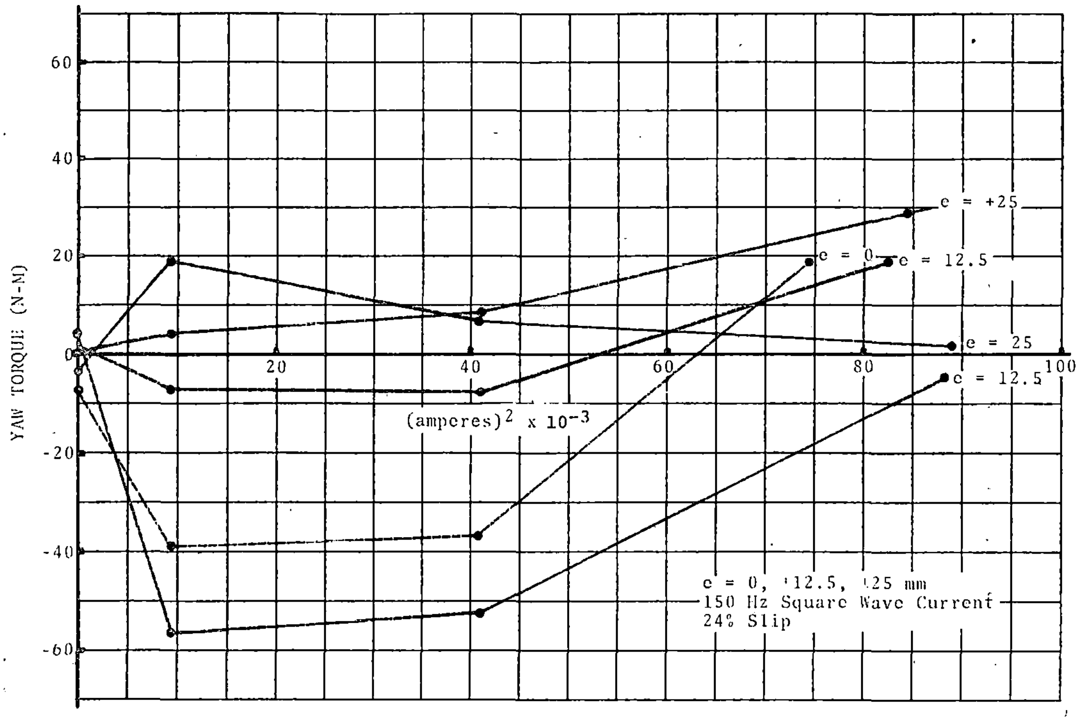

FIGURE 3-24. YAW TORQUE VS. (CURRENT)^2.

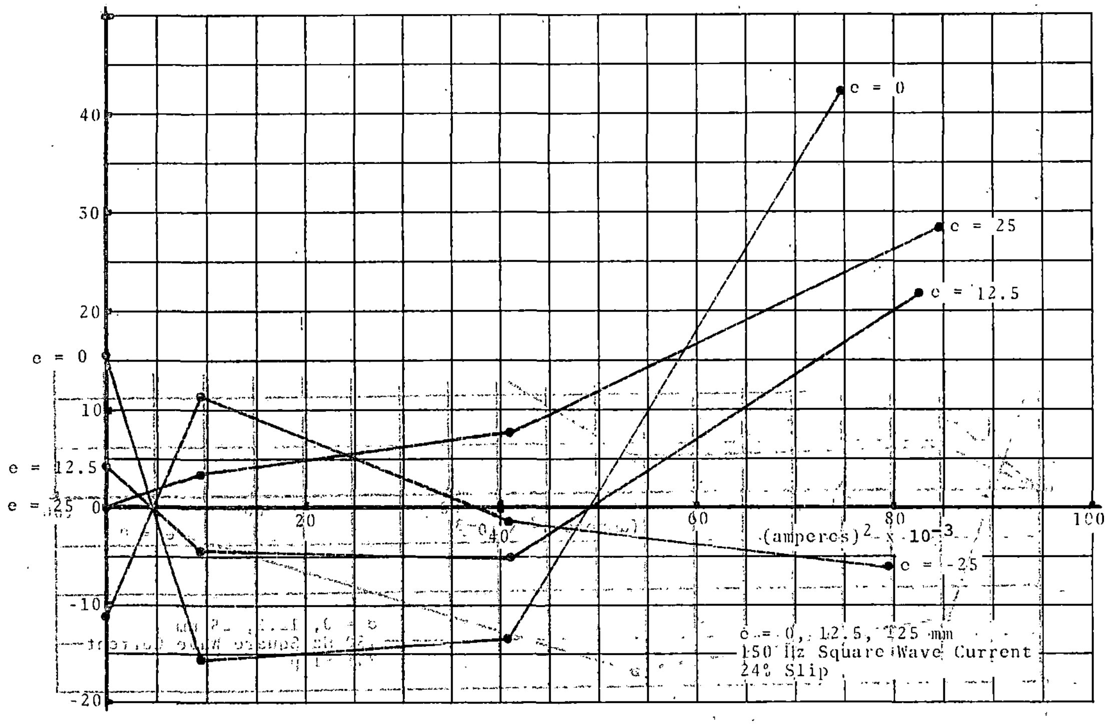

FIGURE 3-25. YAW TORQUE (ADJUSTED) VS. (CURRENT)^2.

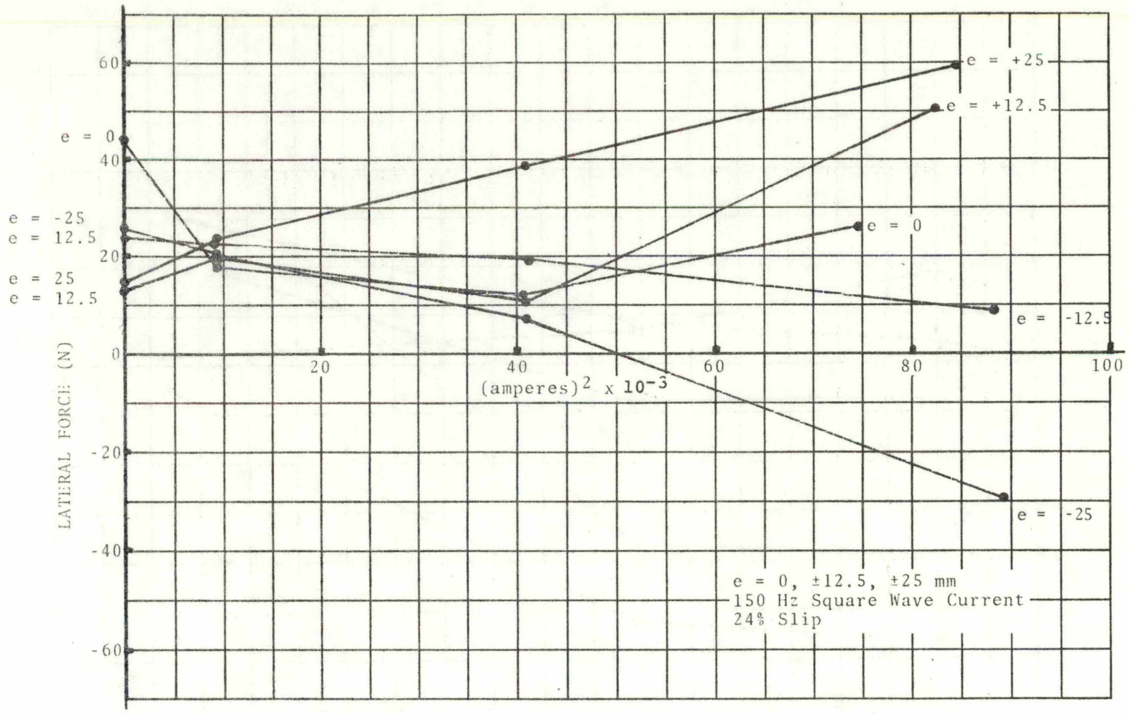

FIGURE 3-26. LATERAL FORCE VS. (CURRENT)^2.

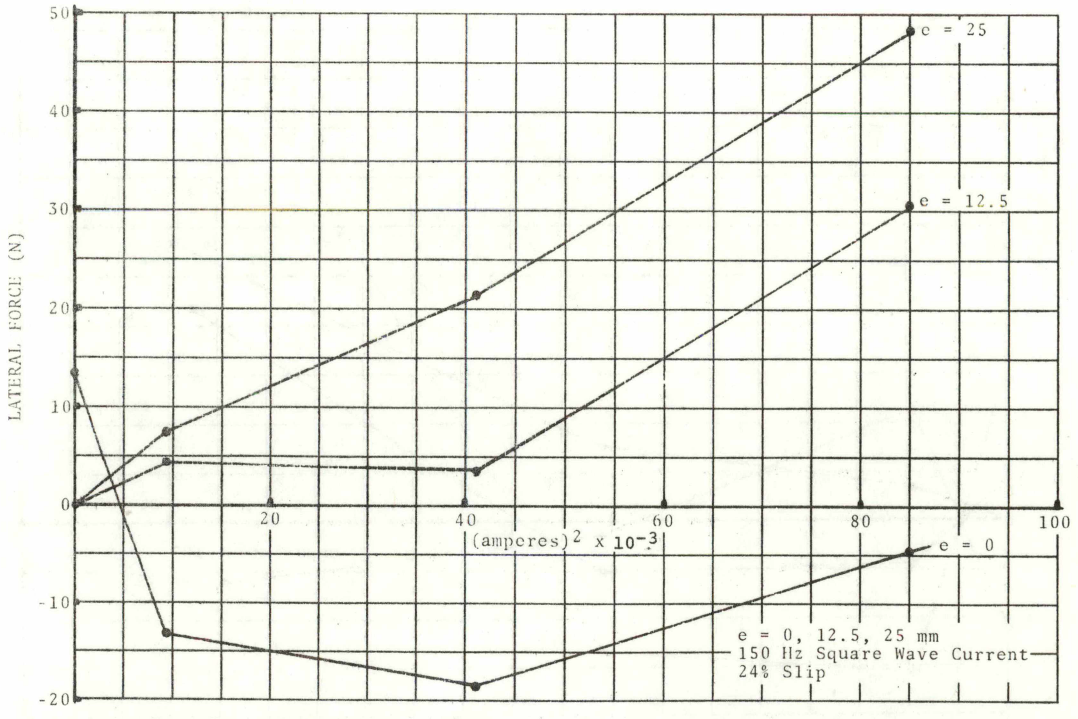

FIGURE 3-27. LATERAL FORCE (ADJUSTED) VS. (CURRENT)^2.

can be obtained from the motor. The 150 Hz lateral forces are similar in magnitude (but opposite in sense) to those reported at 60 Hz.

No significant effects of these lateral displacements were observed on thrust per amperes squared or on efficiency or power factor.

Roll Angle Displacements

No significant force data nor effects on performance were detected in the tests of roll to a = 0, ±0.00148, and ±0.00296 rad. As previously mentioned in the 60 Hz section, these angles apparently were too small to produce any detectable effects.

Yaw Angle Displacements

The forces and torques obtained in tests of the machine operating at the specified yaw angles are presented in Figures 3-28 and 3-30. The magnitudes are, as observed in the 60 Hz tests, rather small; and adjustment of the data was performed in an attempt to sort out trends. The adjusted data is presented in Figures 3-29 and 3-31.

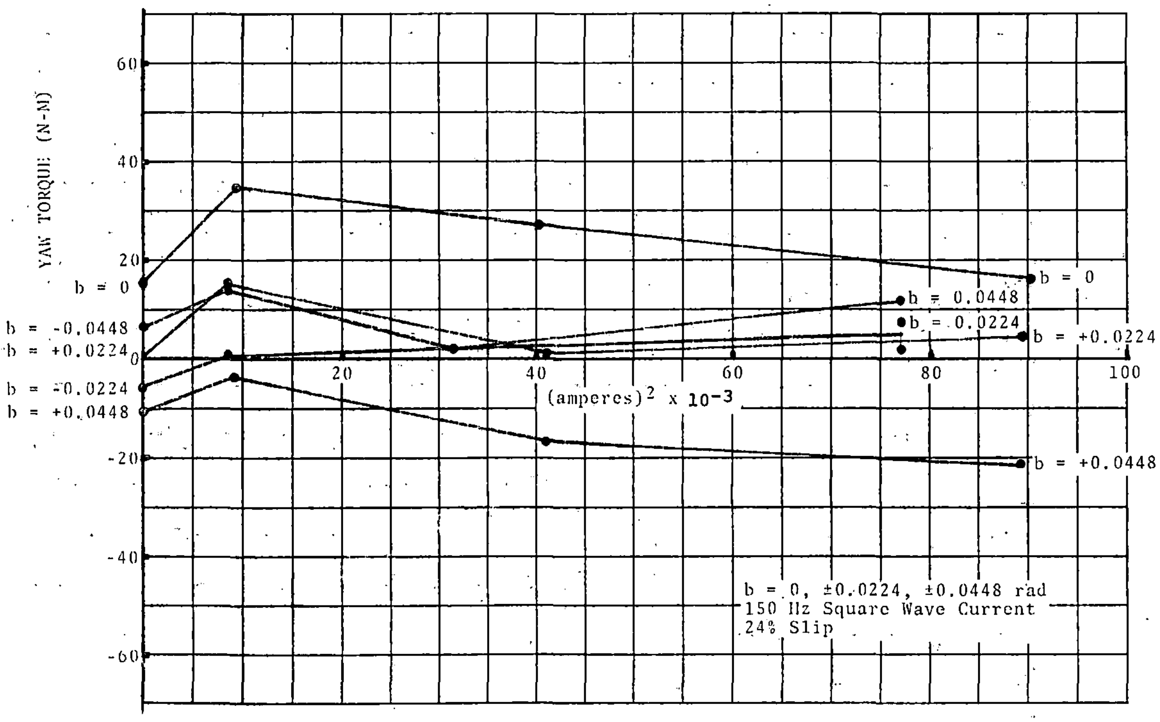

FIGURE 3-28. YAW TORQUE VS. (CURRENT)^2.

Yaw torque data for the centered case appears to be simply mechanical "noise" in the system, but there is an apparent trend toward a small negative yaw torque for the positive yaw conditions. The distribution of attractive and repulsive forces over the stator should predict either no yaw torque or a slight positive one. The

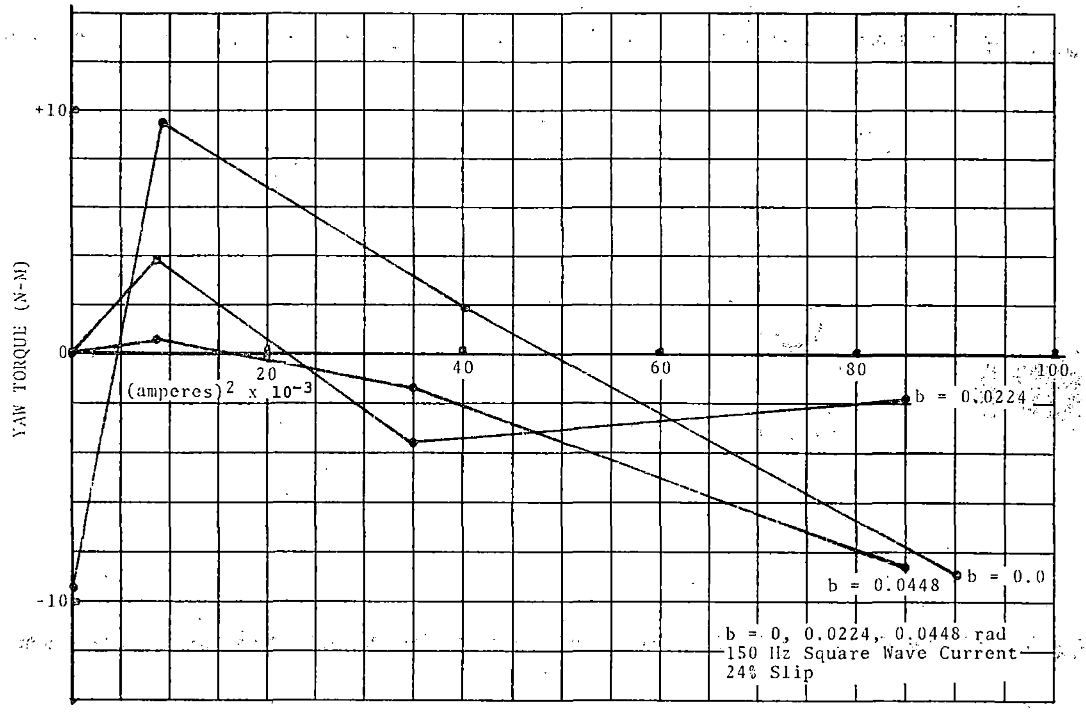

FIGURE 3-29. YAW TORQUE (ADJUSTED) VS. (CURRENT)^2.

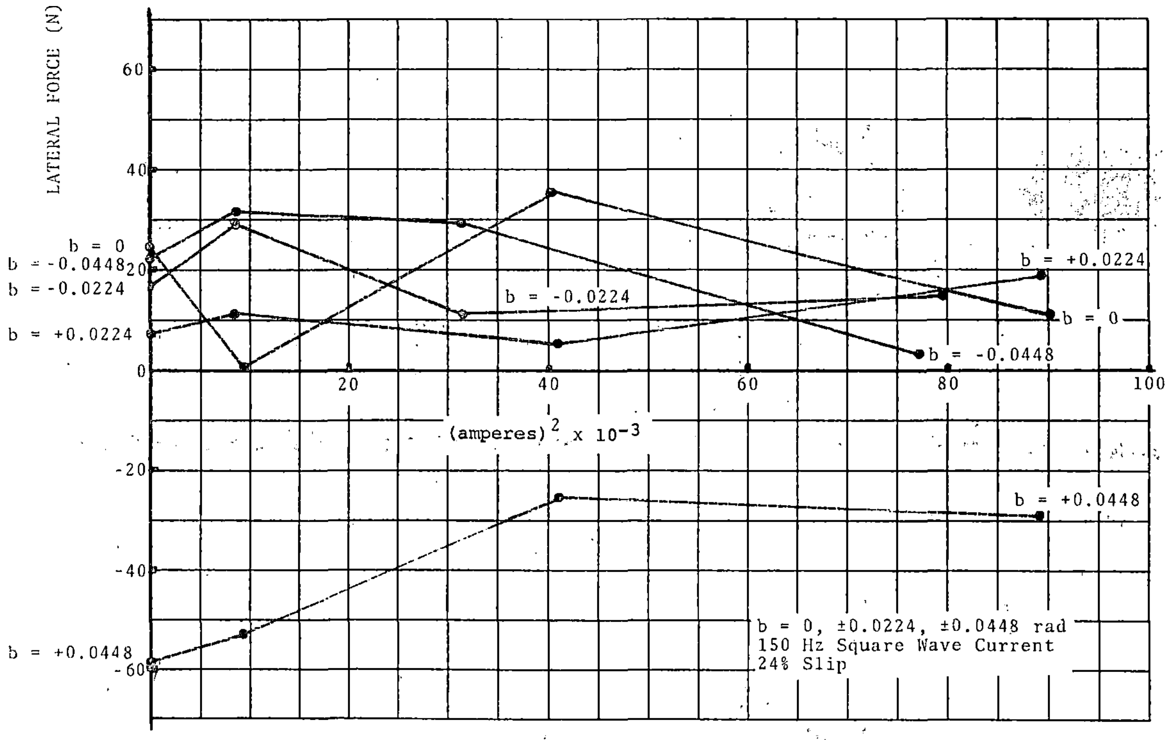

FIGURE 3-30. LATERAL FORCE VS. (CURRENT)^2.

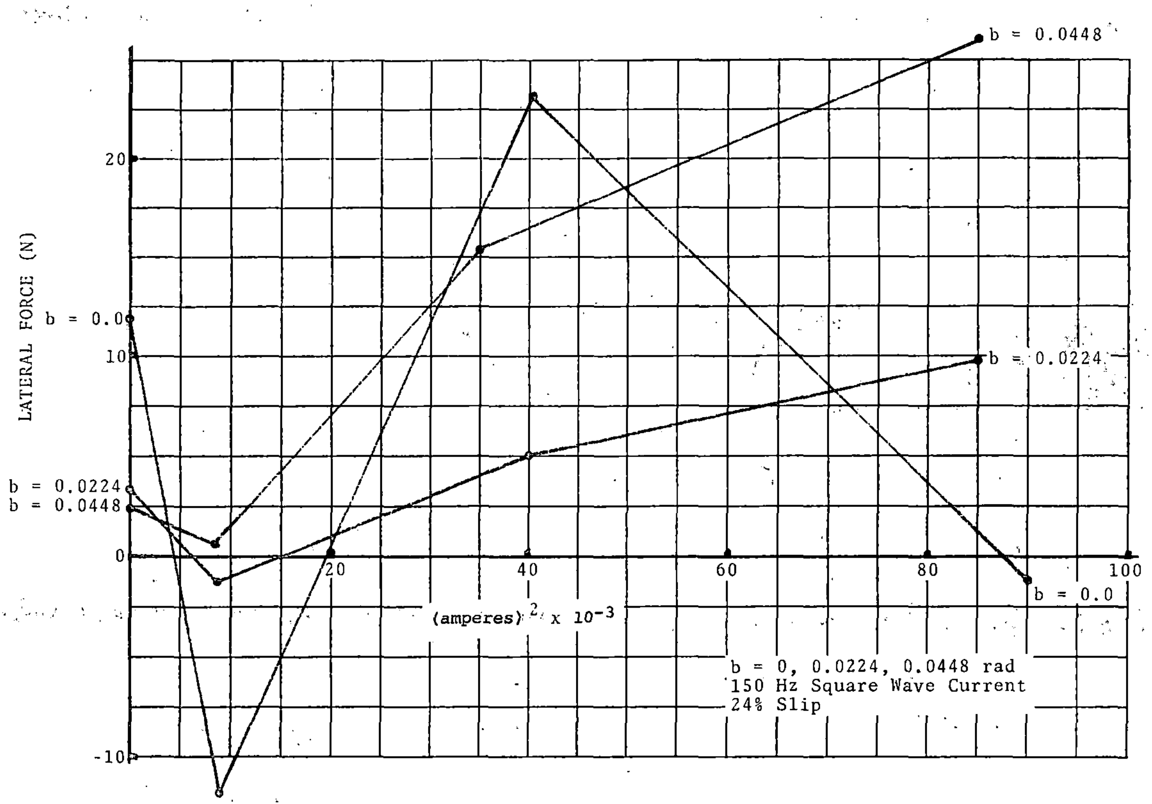

FIGURE 3-31. LATERAL FORCE (ADJUSTED) VS. (CURRENT)^2.

data obtained, with levels of two to eight newton-meters, when the noise of the normal run is ±10 newton-meters, is probably totally insignificant. The significant point is that no appreciable yaw torque was detected for these conditions.

The lateral forces presented in Figure 3-31 are subject to the same question of significance as the yaw torques. Here the distribution of forces in the air gap would predict a positive lateral force for positive yaws because the greater repulsive force at the leading end of the machine would tend to push the stator away from the rail. An attractive force at the trailing end would add to this force, while a smaller repulsive force would subtract, but not completely balance, the large leading end force. The data as presented agrees with this analysis, but the magnitude of force observed was only one to two percent of the rated thrust, and not very significant.

No effects of yaw displacements were seen in thrust, efficiency, or power factor data.

Pitch Angle Displacements

Pitch torque as measured for the pitch angles of c = 0 and ±0.00456 rad is plotted in Figure 3-32. The data is somewhat confusing because no trend is presented. The pitch torque measured for both positive and negative angles is greater than that for the normal position of the stator. The magnitude of pitch torque, as measured at 150 Hz, was about half that measured at 60 Hz, and the

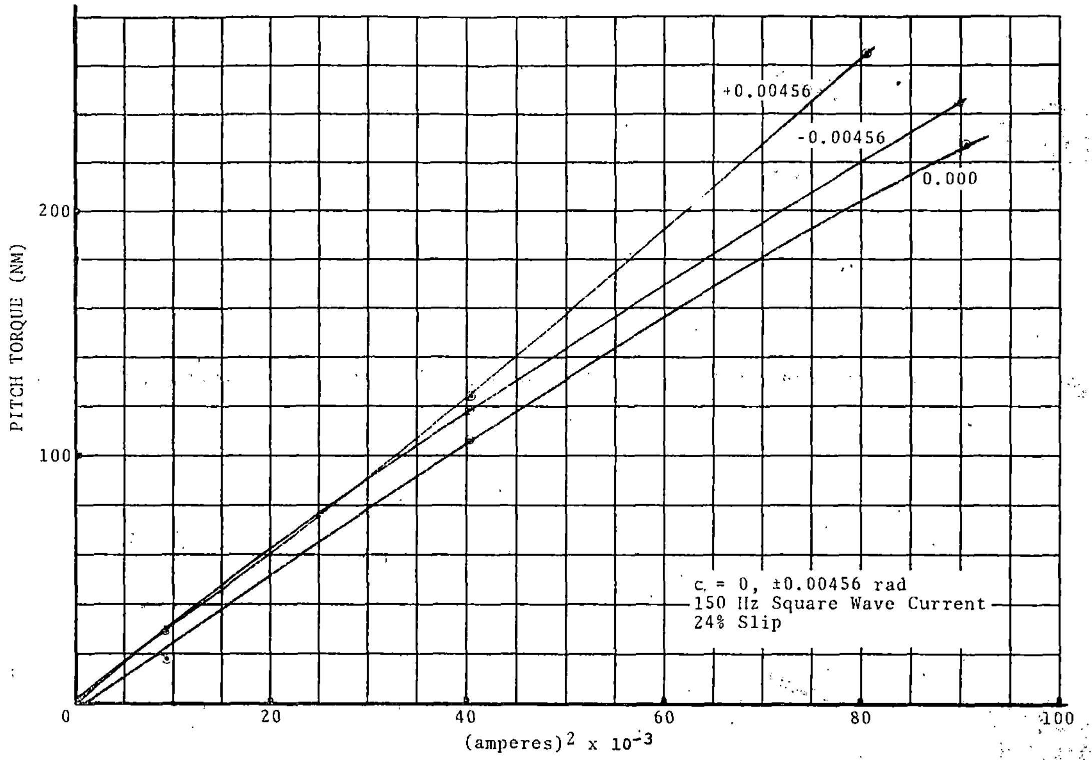

FIGURE 3-32. PITCH TORQUE VS. (CURRENT)^2.

differences shown in Figure 3-32 are relatively small. The data thus suffers from the same sort of problem as the lateral and yaw data, that of showing small differences of large numbers.

No significant effect of pitch angle on pitch torque can be interpreted from this data, and no effect of pitch angle on any other performance measure was observed.

300-HERTZ TESTS

Vertical Displacements

Thrust, radial force, and pitch torque as measured for air gaps of d = 13.1, 18.2, and 23.3 mm are presented in Figures 3-33, 3-34 and 3-35, respectively. The same trends and about the same percentage differences in these parameters are shown as for 60 Hz and for 150 Hz. Again, forces are larger with smaller air gap dimensions. As was the case at 150 Hz, the radial force is negative, indicating levitation of the stator over the rail. Radial force and pitch torque data show some scatter of points, but the direction and approximate magnitude of the effects are clear.

Figure 3-36 shows the rms voltage at the stator terminals for the various operating conditions. As in previous tests, there is a slight increase in voltage for the larger air gap, a slight decrease for the smaller one.

Figures 3-37 and 3-38 show the effects of air gap on efficiency and power factor. The efficiency data seems to have little

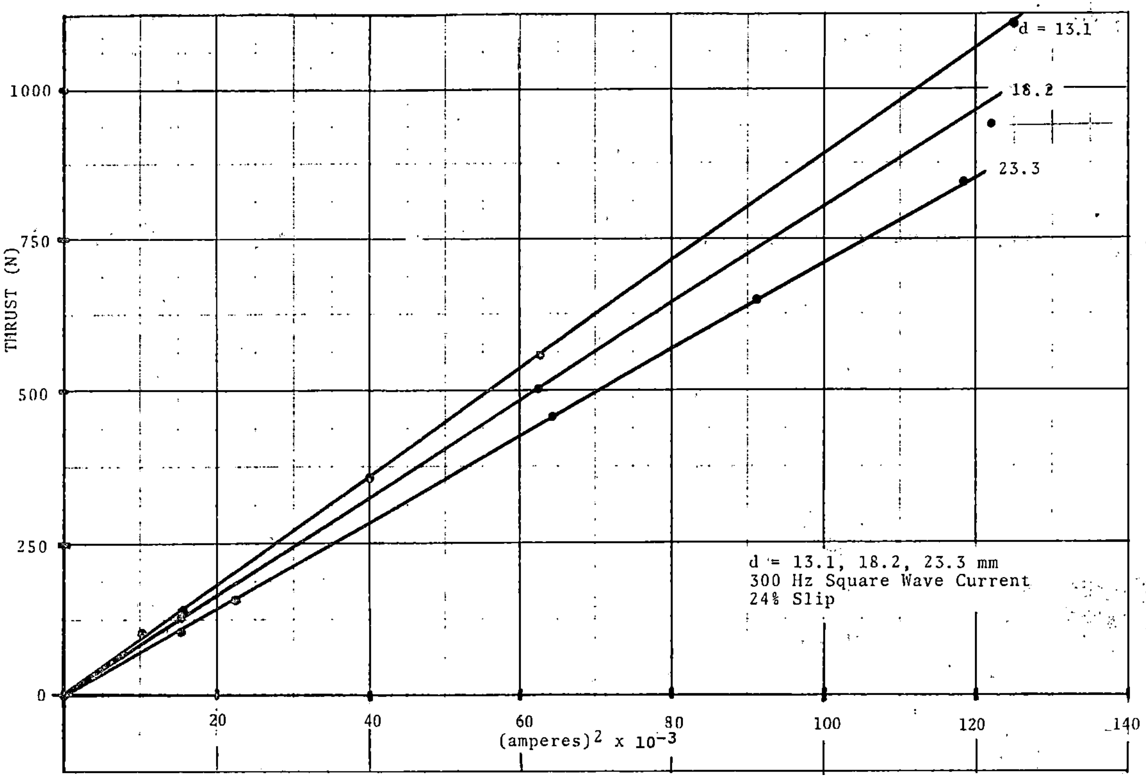

FIGURE 3-33. THRUST VS. (CURRENT)^2.

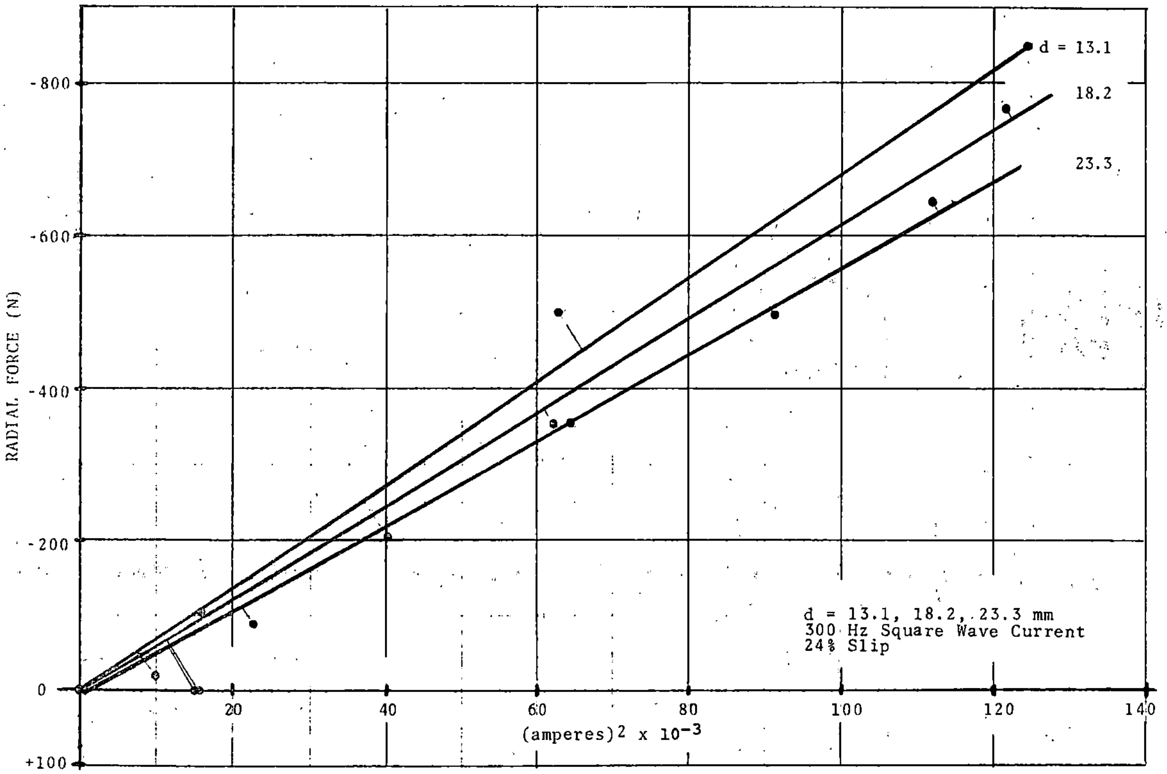

Figure 3-34. RADIAL FORCE VS. (CURRENT)^2.

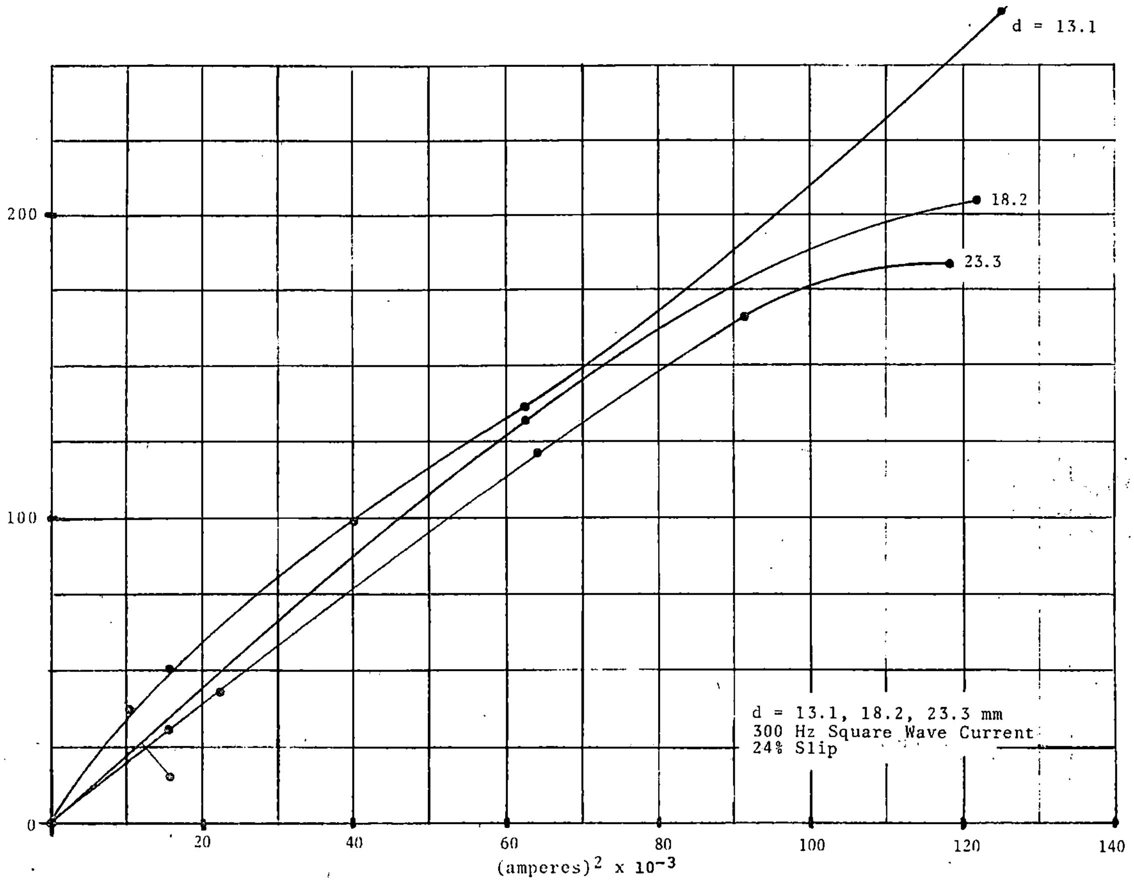

FIGURE 3-35. PITCH TORQUE VS. (CURRENT)^2.

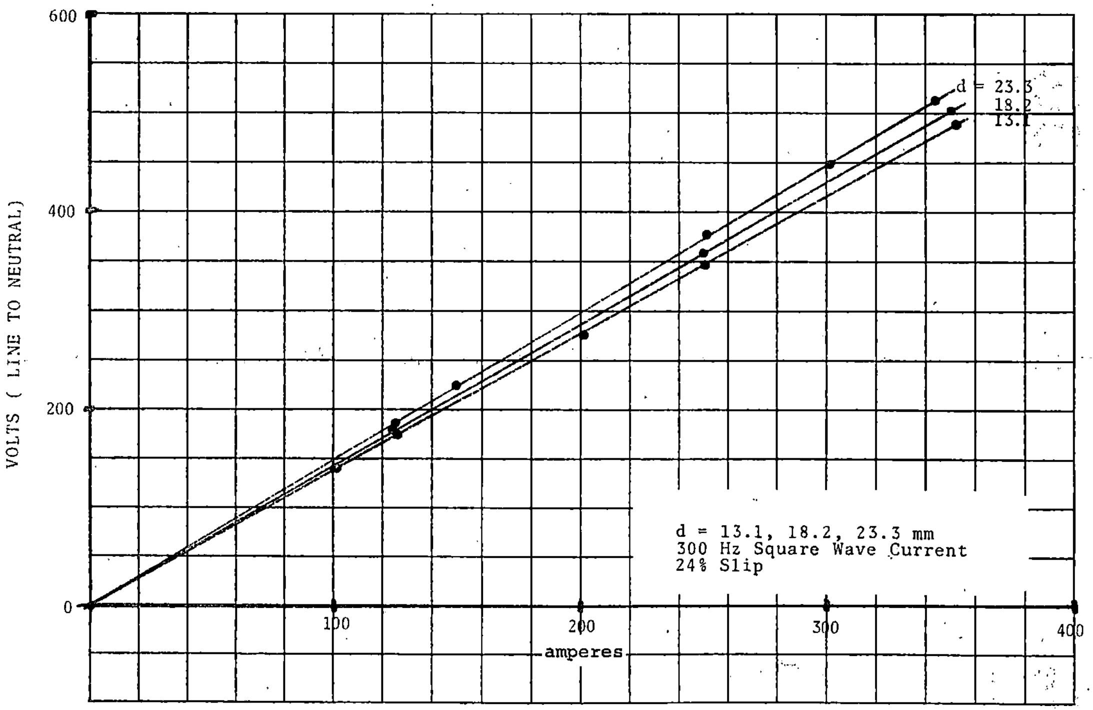

FIGURE 3.36. RMS VOLTAGE VS. LINE CURRENT.

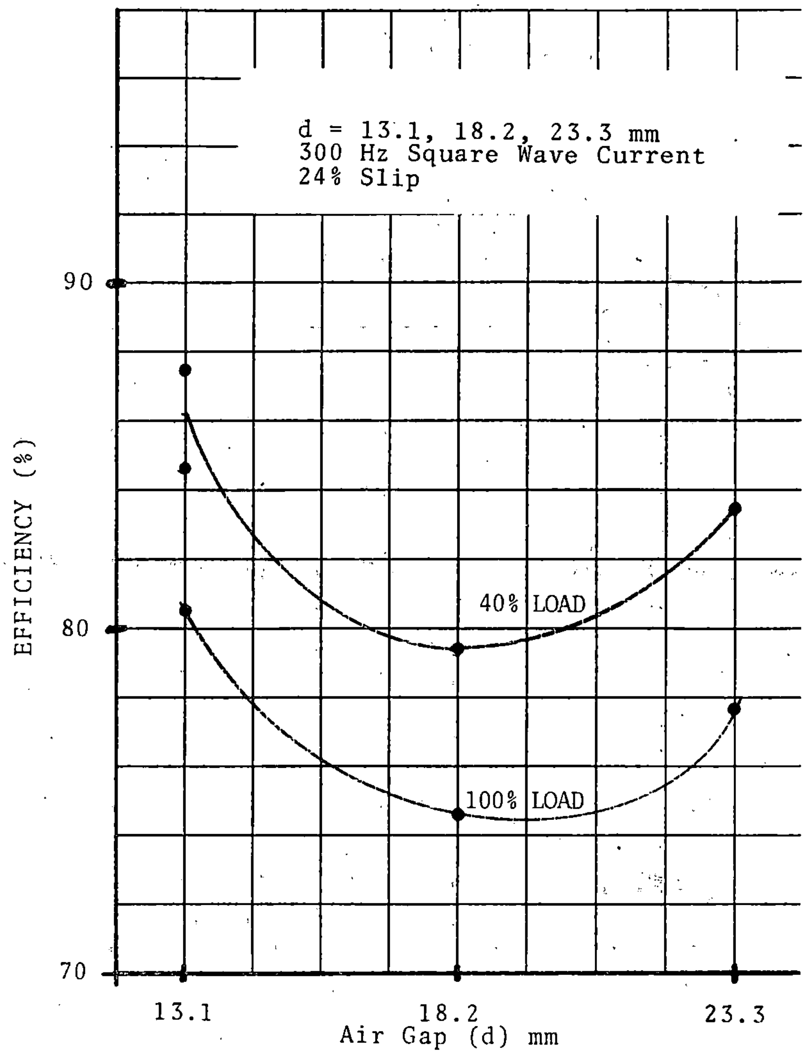

FIGURE 3-37. RELATIVE EFFICIENCY VS. AIR GAP.

meaning for the reasons mentioned in the sections describing the 150 Hz tests. Power factor displays the same trends of increase with decreasing air gap that had been observed at lower frequencies. The load data for efficiency was not at all logical, and the light load curve of power factor is rather questionable.

Lateral Displacements

Figure 3-39 shows the lateral forces measured for lateral displacements of the stator of e = 0, ±12.5, ±25, -51 and -76 mm. The 51 and 76 mm displacements were tested as a result of suggestions made at the Seventh Quarterly Review, and their results proved very interesting.

In Figure 3-39 the lateral forces have been adjusted to show zero force at or near zero current. The magnitudes of forces observed here are about 100 N, whereas the 60 and 150 Hz tests were producing 30 to

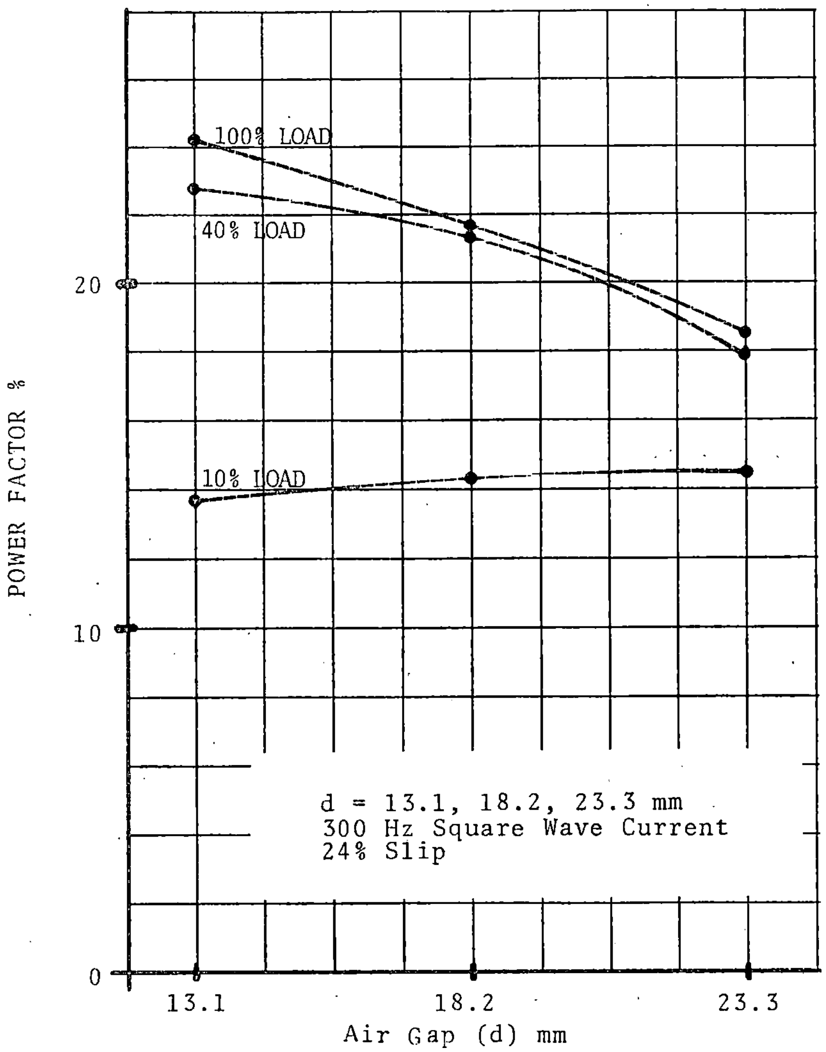

FIGURE 3-38. APPARENT POWER FACTOR VS. AIR GAP.

40 N for the same 25 mm displacements. The forces have the same sign as the displacement, making them antiguidance forces, as they were for the 150 Hz case. The increased magnitude of forces has brought them up out of the mechanical noise of the system, and they exhibit a reasonable behavior with respect to magnitude of displacement and current squared.

Yaw torque data was studied, but the magnitudes were small and the effects did not show any consistent trends. As a result, this data was not plotted. With the entire stator repelling the rail, positive lateral forces of nearly equal magnitude occur at the lead and trail ends of the stator, and no significant yaw torque would be expected.

The effect of lateral displacements of large magnitude (up to 76 mm, which is 44% of the width of the stator) on lateral force, thrust, and radial force, are presented in Figures 3-40, 3-41 and 3-42, respectively. With the largest displacement, 76 mm, thrust

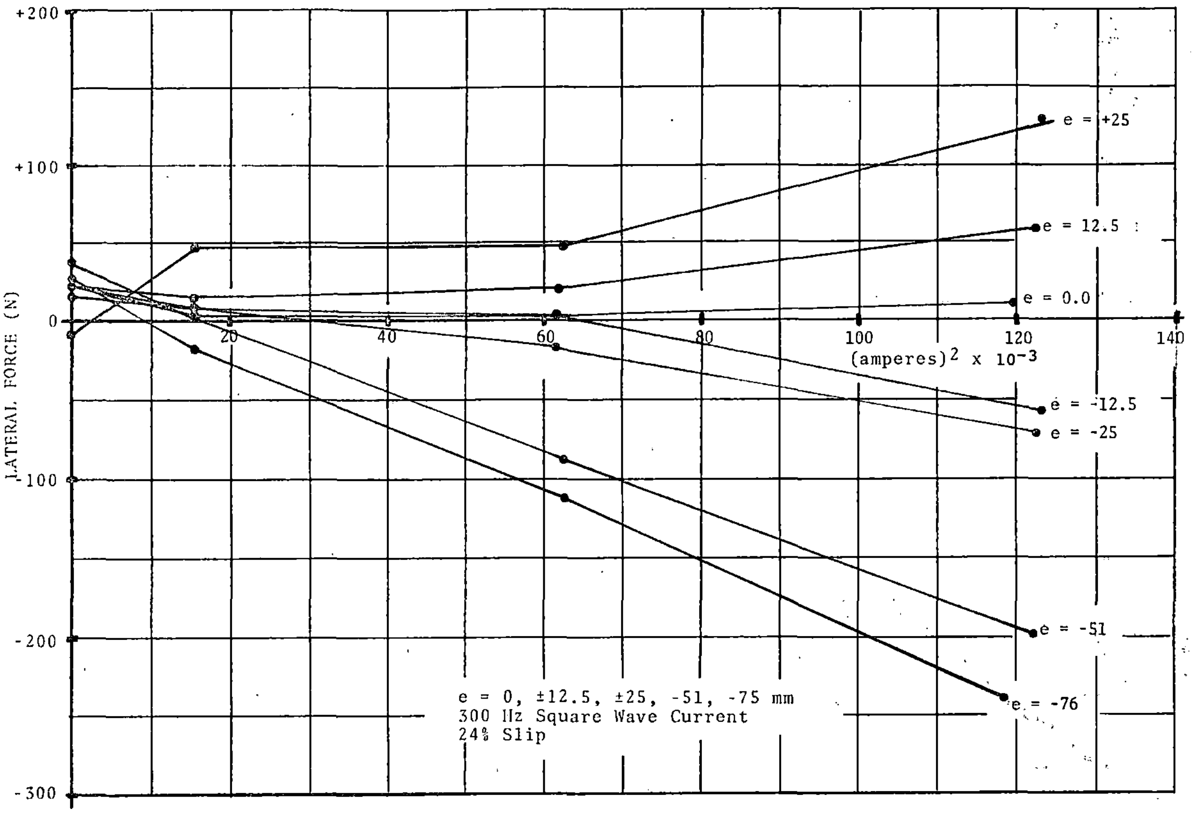

FIGURE 3-39. LATERAL FORCE VS. (CURRENT)^2.

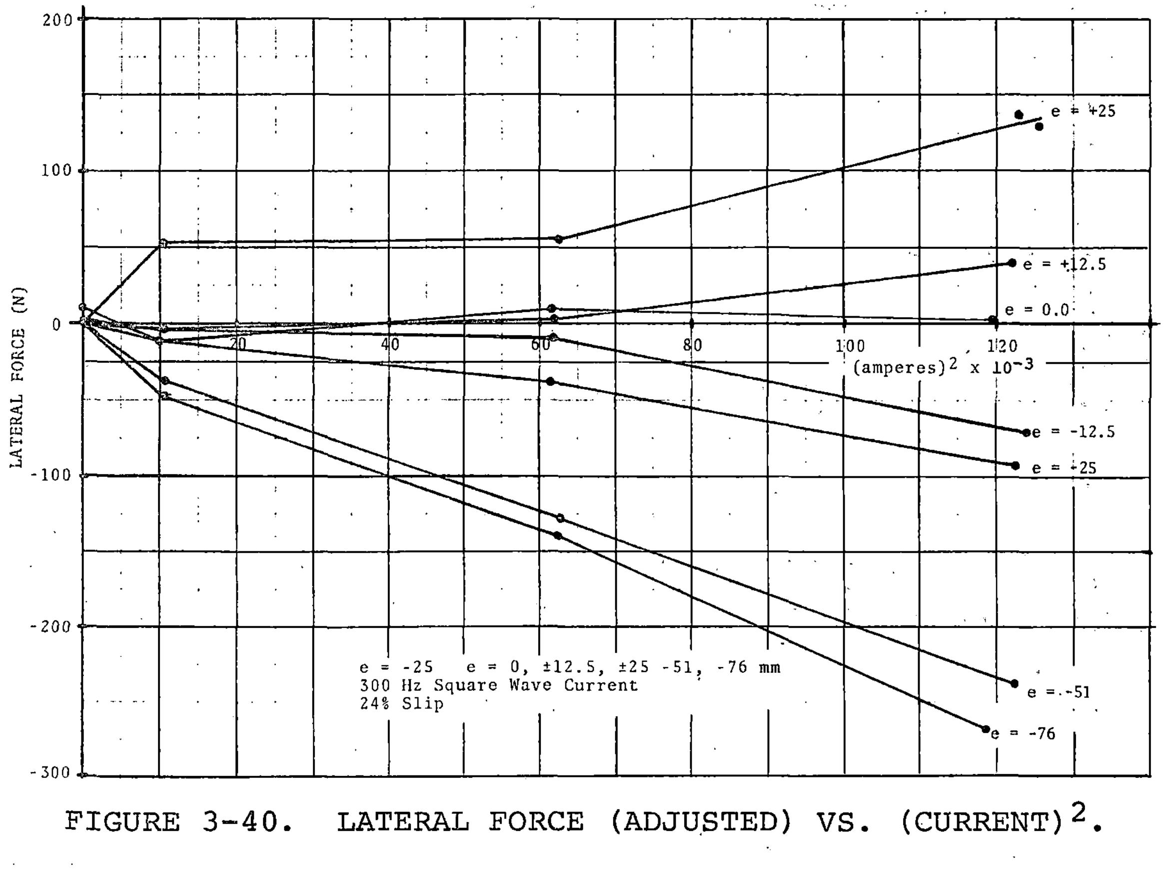

FIGURE 3-40. LATERAL FORCE (ADJUSTED) VS. (CURRENT)^2.

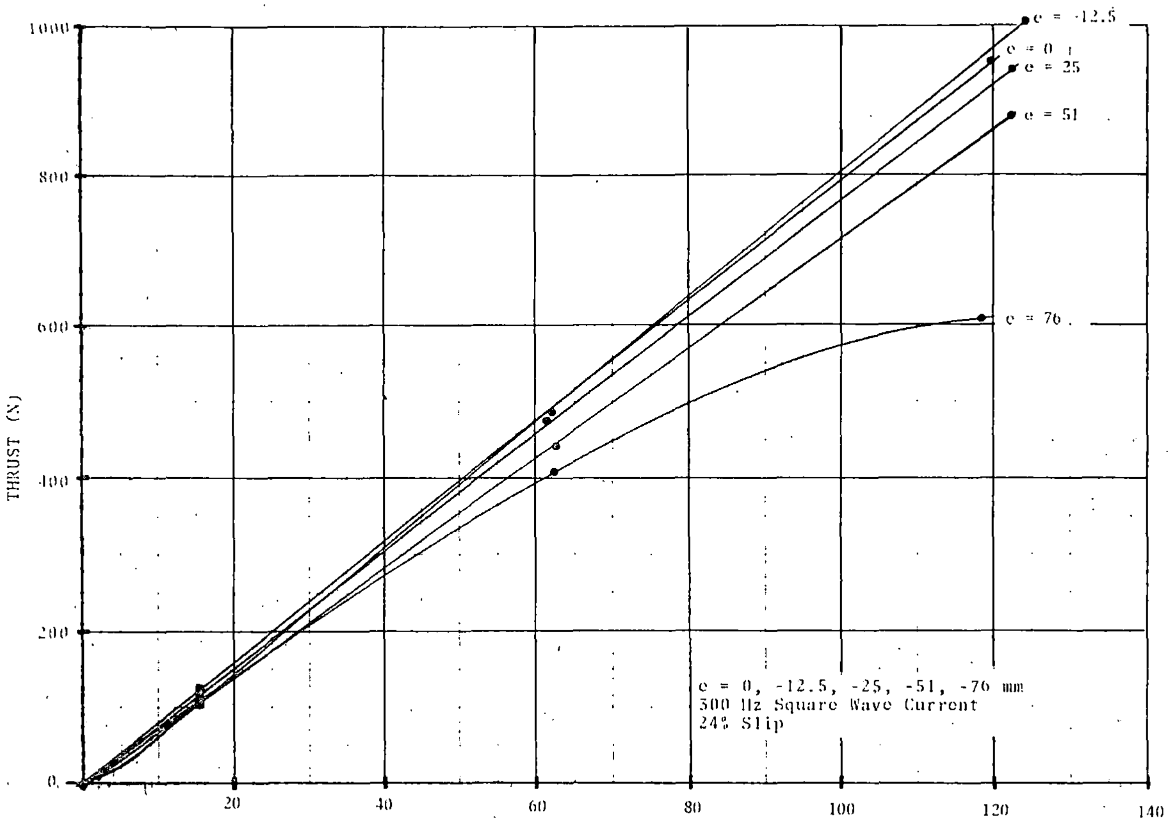

FIGURE 3-41. THRUST VS. (CURRENT)^2.

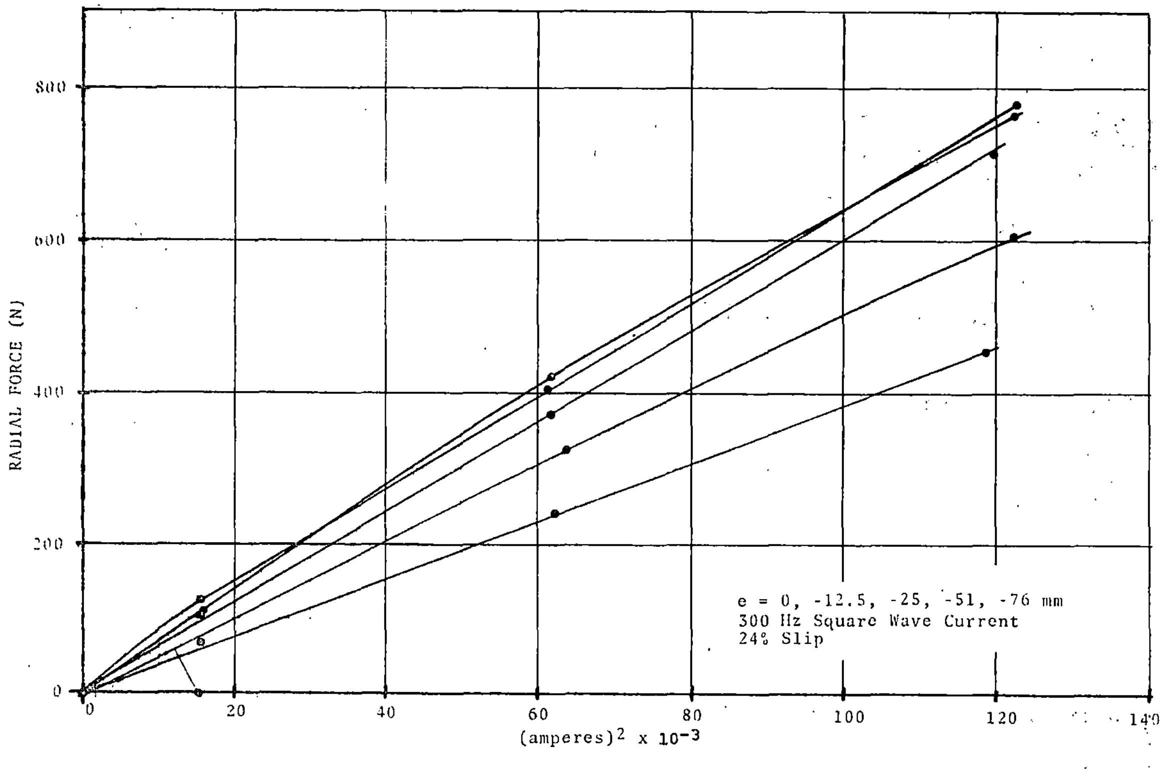

FIGURE 3-42. RADIAL FORCE VS. (CURRENT)^2.

at 350 A was down from 1000 to 600 N, radial force was down from -800 to -450 N, and lateral force was 44% of thrust at 270 N. For the displacements tested, at high current levels, the ratio of lateral force to thrust approximates the ratio of displacement to stator width, as shown in Table 3-2. A similar relationship of ratios holds if radial force is substituted for thrust, except that this ratio is about 40% greater across the board.

TABLE 3-2. DISPLACEMENTS AT HIGH CURRENT LEVELS

Displacement	Displacement % / Stator Width	Lateral Force % / Thrust	Lateral Force % / Radial Force
0	0	0	0
12.5 mm	7	7	9
25	15	9	13
51	30	27	40
76	44	44	62

At low current levels, the thrust of the machine seems to be nearly unaffected by the displacement of the stator. At high currents, the thrust for the largest displacement drops off very rapidly, a fact that seems to indicate a saturation effect in the machine. The voltage at the terminals of the machine, when run at 350 A and the 76 mm displacement, is about 6% higher than for zero displacement.

Roll Angle Displacements

No significant forces or effects on performance were noted in tests at the specified angles of roll.

Yaw Angle Displacements

Yaw torque and lateral force for yaw displacements of b = 0, ±0.0224 rad, and ±0.0448 rad are plotted in Figures 3-43 and 3-45, respectively. The adjusted values of yaw torque which appear in Figure 3-44 do not appear to show any consistent trend. If both ends of the machine are levitated, any yaw torque detected should be in the same direction as the displacement. In the data there does not appear to be any such trend, but the torques are all around 10 N. The b = 0 data indicate the magnitude of the random mechanical noise effects to be larger than this 10 N level. so that, as has been mentioned before, the significant point about the data is that the torques are very small.

The lateral force data was adjusted and plotted in Figure 3-46, where it appears that there is a noticeable effect of yaw angle on lateral force. The lateral force is relatively small (10 to 20 N) but is positive for a positive yaw angle. The greater repulsive force at the lead end, compared to the trailing end, should result in a lateral force to push the leading end of the stator further from the rail; and the data agrees with this prediction.

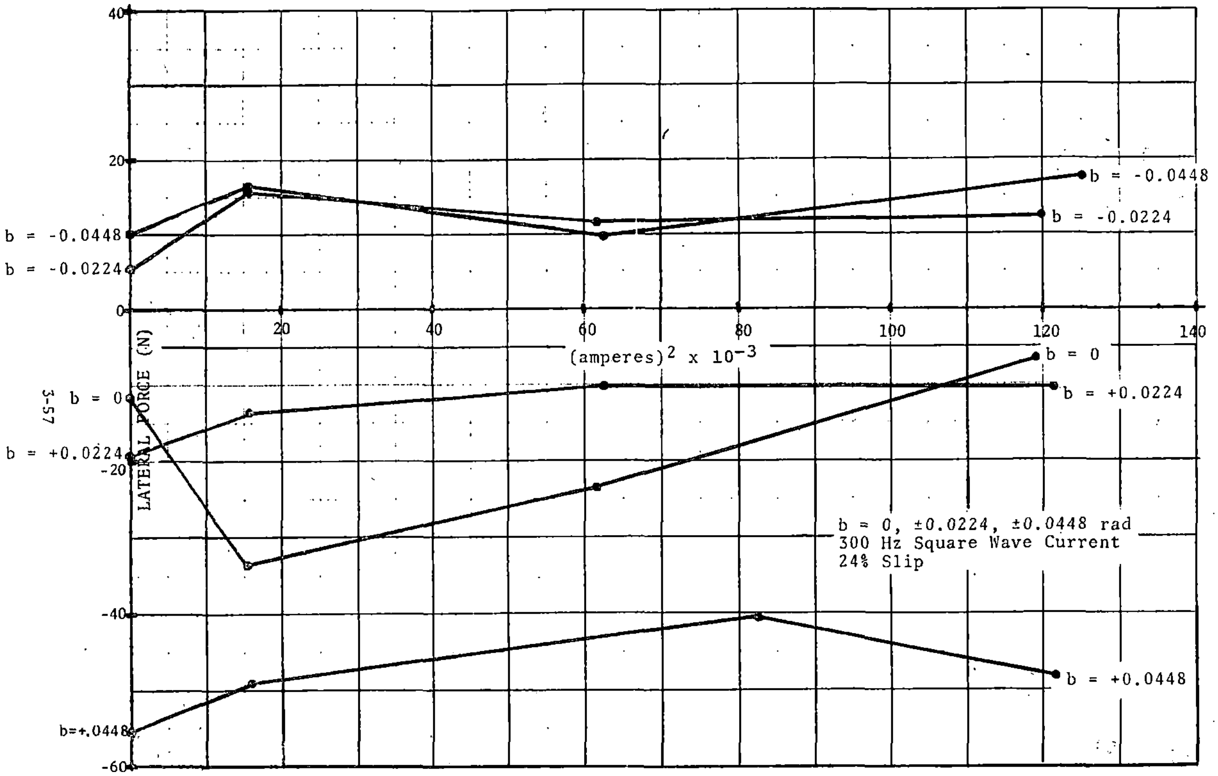

FIGURE 3-43. YAW TORQUE VS. (CURRENT)^2.

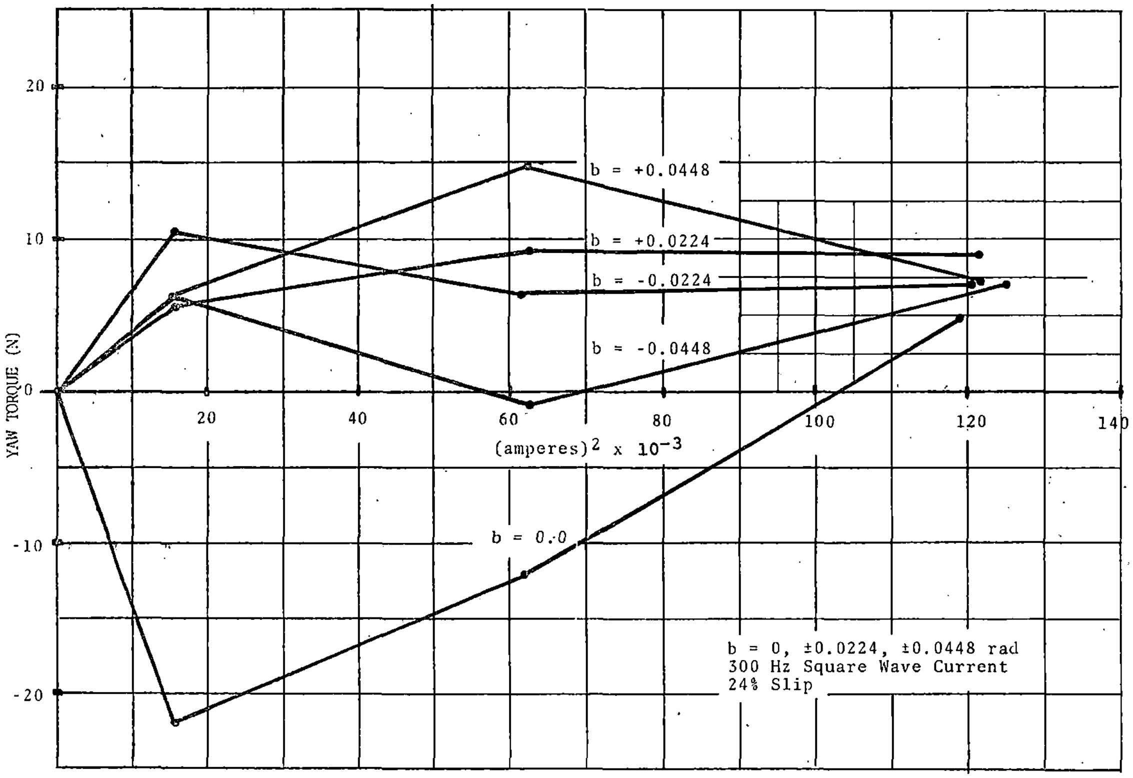

FIGURE 3-44. YAW TORQUE (ADJUSTED) VS. (CURRENT)^2.

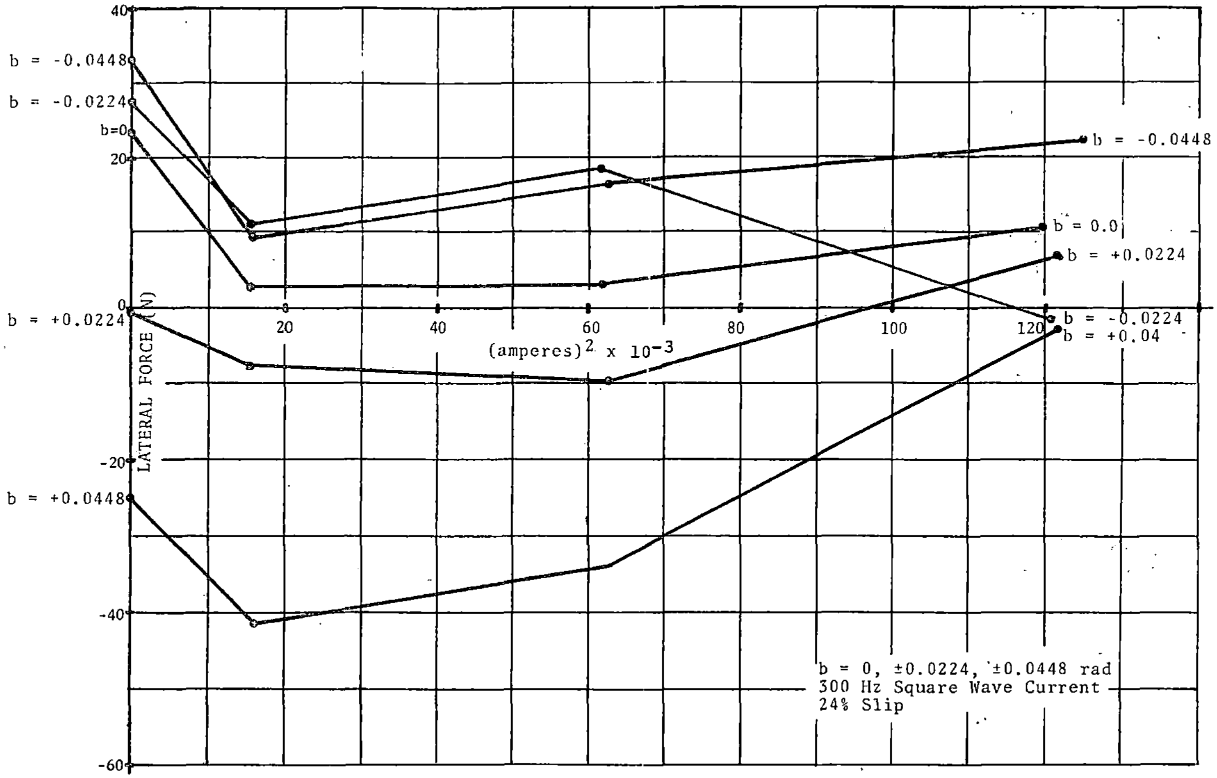

FIGURE 3-45. LATERAL FORCE VS. (CURRENT)^2.

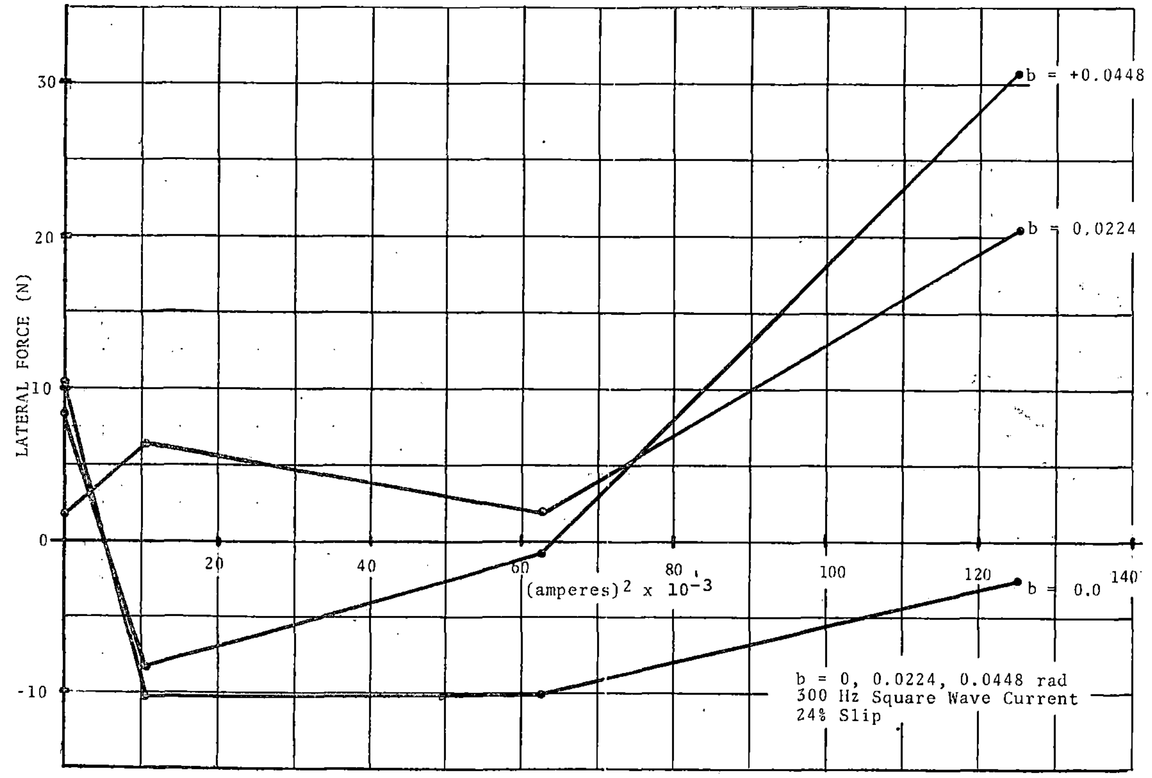

FIGURE 3-46. LATERAL FORCE (ADJUSTED) VS. (CURRENT)^2.

There were no apparent effects of these yaw displacements on thrust, radial force, or on any performance measurements.

Pitch Angle Displacements

Figure 3-47 shows the pitch torque produced on the stator for pitch angles of c = 0, ±0.00456 rad. The pitch torque for a negative pitch angle is greater than for the normal position, the torque for a positive pitch angle less than the normal. This effect is the opposite of that seen at 60 Hz and amounts to a stabilizing influence. The change in pitch causes an opposing pitch torque. This reversal of effect from low frequency to high may explain the confused data at 150 Hz. At some frequency between 60 and 300 Hz, the pitch torque should not change as the pitch of the stator is changed. If this frequency is near 150 Hz, then the data obtained there does, in fact, make some sense.

No effects on the performance of the machine or on other force measurements were noted during the pitch angle tests.

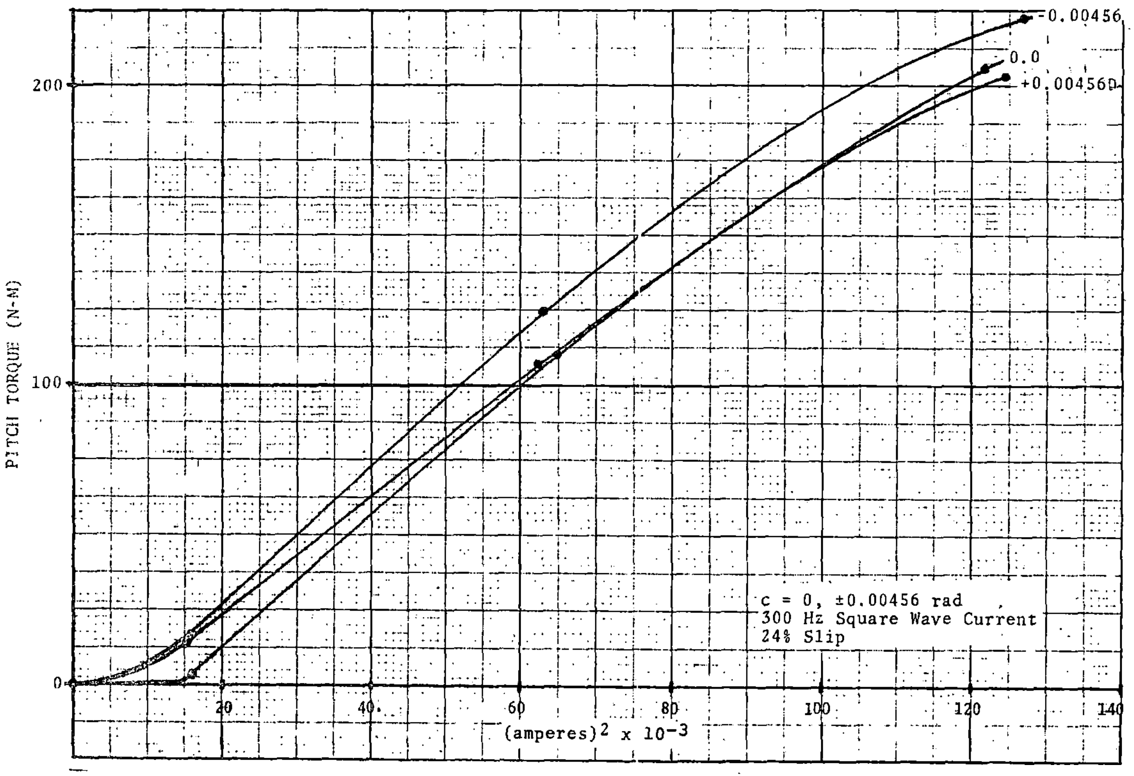

FIGURE 3-47. PITCH TORQUE VS. (CURRENT)^2.

Section 4

INTERPRETATION OF PERFORMANCE DATA

INTRODUCTION

In this section of the report, several aspects of the data contained in the appendix will be extracted and analyzed. For reasons of practicality, this treatment can include neither all of the data nor all aspects of the data that is examined. Since most of the data was obtained with nonsinusoidal current and voltage from the inverter variable frequency source, the method of establishing correspondence between the test data and sinusoidal excitation theories will be established. Next, since a certain amount of scaling must be done to put all of the experimental data on the same basis, the linearity of the machine will be demonstrated. With these preliminaries, the thrust, efficiency, normal forces, and internal fields can be discussed and compared to theoretical predictions.

NONSINUSOIDAL WAVEFORMS

The inverter drive for the linear induction motor (LIM) experiment is an auto sequential type commonly referred to as a controlled current inverter (CCI).(1,2) Typically, the inverter switches a direct current (held constant by a large inductor in the dc link) into the terminals of the motor so that, ideally, only two phases are conducting current at any one time. The result is that, unlike most conventional or voltage source inverters, the current in the motor is fixed, as illustrated in Figure 4-1, for one phase. Current flows for 120° in each direction with a magnitude equal to the dc link current. The resulting motor voltage is sinusoidal except for large commutation "spikes," which are actually portions of a sinusoid. The current does not switch instantaneously as the transition is also a portion of the commutation sinusoid.

At 60 Hz, the commutation interval is short compared to the period so that the actual current and voltage, Figure 4-2, look very much like the ideal waveforms. There is some slope to the current transition, and there is some rectifier ripple on the dc link current.

In spite of the nonzero rise time and ripple, the principal harmonics of the current are very close to the theoretical Table 4-1 (there should also be a strong sixth harmonic of the 60 Hz line (360 Hz) due to the rectifier ripple). Normally, the average

---

1. Ward, E.E., "Inverter Suitable for Operation Over a Range of Frequency," Proceedings IEEE, Vol. III, No. 8 (August 1964), 1427-34.

2. Cornell, E.P. and Lipo, T.A., "Modeling and Design of Controlled Current Induction Motor Drive Systems," Transactions IAS, Vol. IA-13, No. 4 (July/August 1977), 321-29.

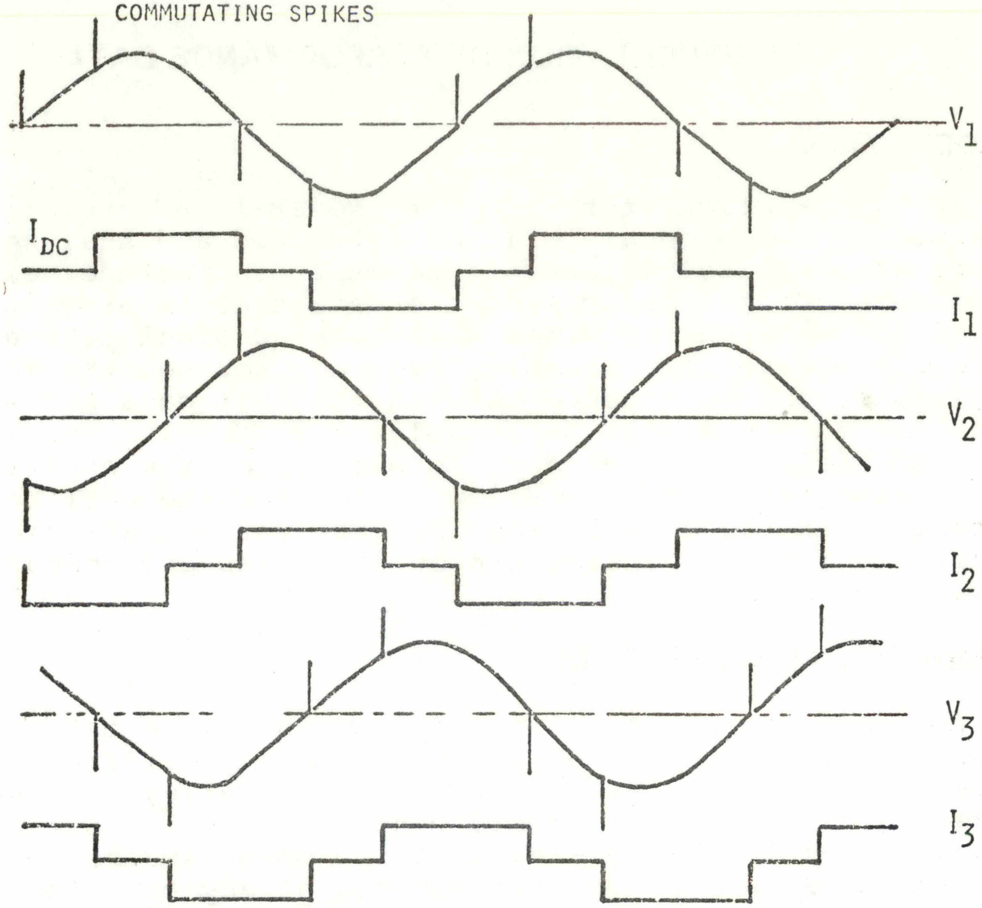

FIGURE 4-1. VOLTAGE AND CURRENT WAVEFORMS FOR THE CONTROLLED CURRENT INVERTER.

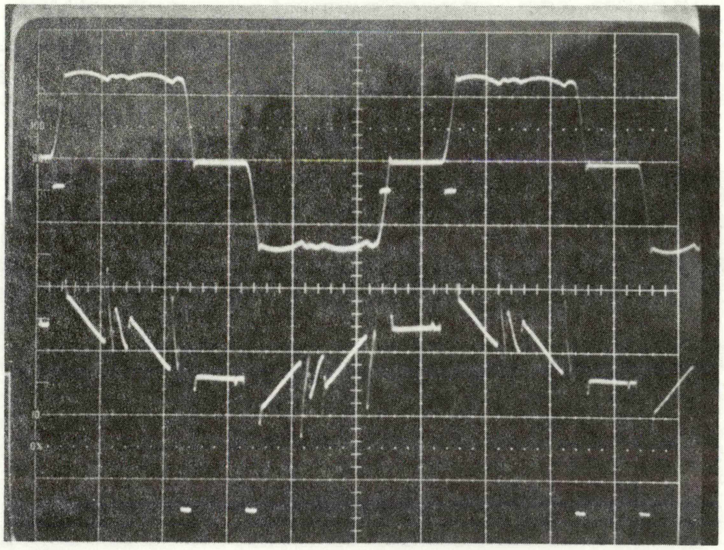

FIGURE 4-2. 60 Hz INVERTER DRIVE CURRENT (TOP) AND VOLTAGE (BOTTOM).

TABLE 4-1. HARMONIC STRUCTURE OF LIM CURRENT AND VOLTAGE AT 60 Hz

	CURRENT		VOLTAGE
Harmonic Number	Theory	Measure	Measure
1	1.000	1.00	1.00
5	0.200	0.18	0.49
7	0.143	0.15	0.74
11	0.091	0.07	0.59
13	0.077	0.07	0.50
17	0.059	0.04	0.44
19	0.053	0.04	0.34
21	0.048	0.01	0.05
23	0.044	0.02	0.31
25	0.040	0.02	0.16
27	0.037	0.01	0.05

thrust of a motor will be due almost entirely to the fundamental of such complex waveforms (the harmonics contribute only very small and generally canceling thrusts).[3]

The current and voltage sensors in the Data Acquisition System (DAS) respond to the true rms of the waveforms presented to them. For the ideal waveforms of Figure 4-1, the rms of the fundamental is related to the true rms by a factor of $3/\pi = 0.955$. The harmonics of the voltage waveforms, on the other hand, are quite large and depend strongly on power factor as well as amplitude. It is, therefore, not practical to attempt to deduce the fundamental from the true rms.

As the frequency of the inverter increases, the commutation interval becomes a larger fraction of the period, as shown in Figures 4-3 and 4-4. At 300 Hz (Figure 4-4), the current waveform is almost sinusoidal; hence, the relation between fundamental rms and true rms is taken to be unity. However, at 150 Hz (Figure 4-3), the waveform, while not ideal, still retains some stepped character; hence, an intermediate value for the constant of 0.98 will be assumed.

---

[3] Kliman, G.B., "Harmonic Effects in PWM Inverter-Induction Motor Drives," IAS Conference Record, 7th Meeting (October 1972).

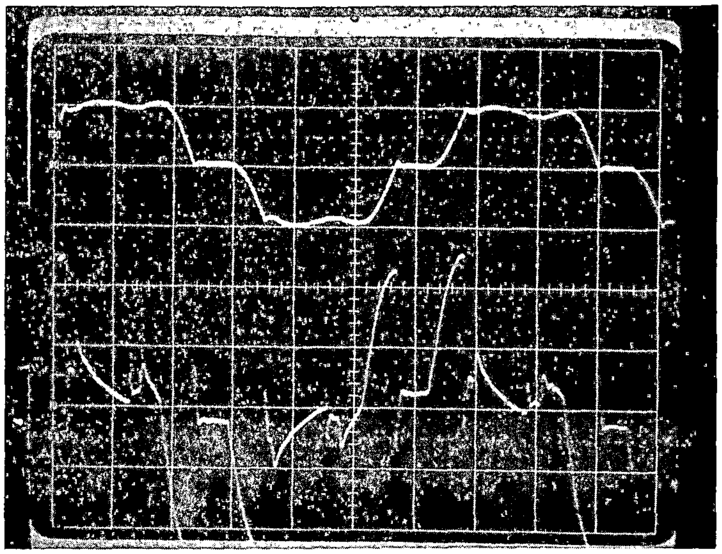

FIGURE 4-3. 150 Hz INVERTER DRIVE CURRENT (TOP) AND VOLTAGE (BOTTOM).

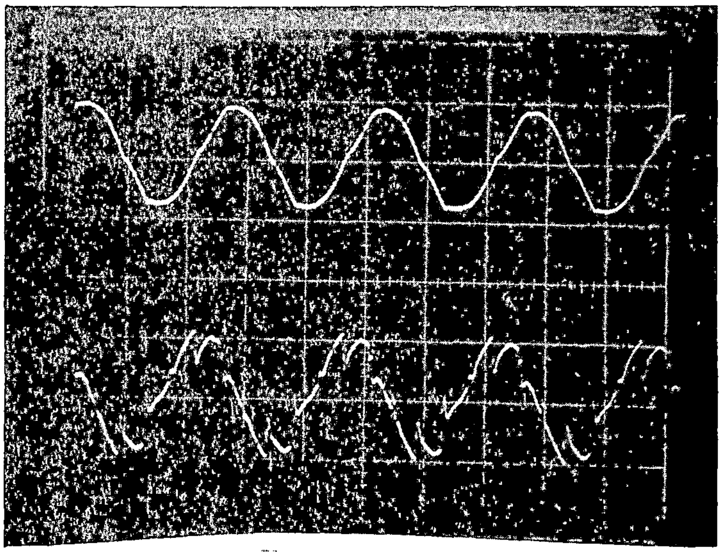

FIGURE 4-4. 365 Hz INVERTER DRIVE CURRENT (TOP) AND VOLTAGE (BOTTOM).

Fortunately, although not originally planned, much 60 Hz sine wave data was taken. A comparison of the thrust at 200 A (fundamental rms) when operating with 60 Hz sinusoids from the power mains and when operating from the inverter at 60 Hz is shown in Figure 4-5. The thrusts, when the inverter drive currents are adjusted by $3/\pi = 0.955$ are generally within 3%, which is close to the resolution of the DAS and is well within the measurement tolerances for conventional motors. The slightly higher thrust on square wave current could be due to a slightly higher value of fundamental current than given by $3/\pi$ or a slightly better current balance. The inverter tends to force the same current in each branch of the motor and unbalance the voltages slightly, whereas

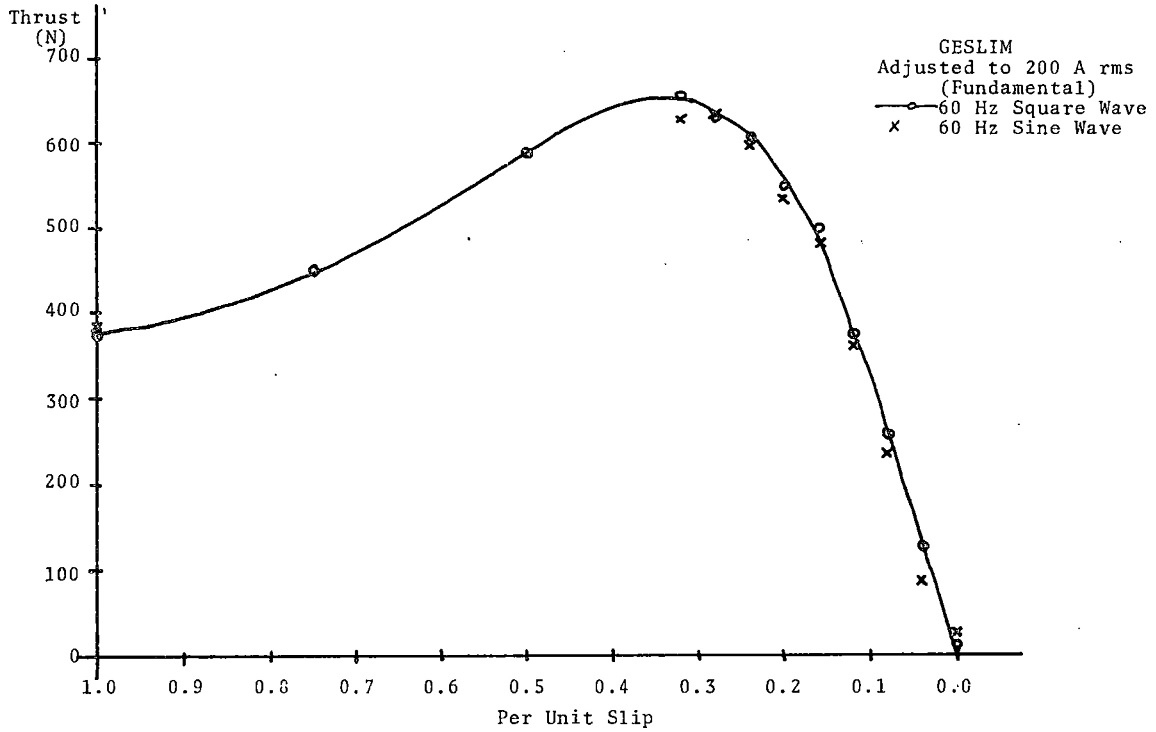

FIGURE 4-5. THRUST AS A FUNCTION OF SLIP FOR 60 Hz SINE WAVE AND SQUARE WAVE CURRENT.

the 60 Hz supply was a relatively well-balanced voltage source resulting in slightly more current unbalance (4.1% vs. 2.6%, at 24% slip). In either case, the amount of current unbalance would be considered normal or better than normal in a conventional motor.

A comparison of efficiency at 60 Hz on square wave and sine wave excitation is shown in Figure 4-6. Again, the results are quite close, being generally within three percentage points. The square wave efficiencies are, surprisingly, consistently higher than those for sine waves. This should not be so, and can only be attributed to minor differences in the response of the instruments on nonsinusoidal excitation or, possibly, to the better current balance on CCI drive. In the following sections, the factors of 0.955 at 60 Hz, 0.980 at 150 Hz and 1.000 at 300 Hz will be utilized without further comment.

LINEARITY AND SKIN SATURATION

In most previously reported linear induction motor experiments, the motor was either double-sided or in single-sided linear induction motors (SLIM), the back iron was well laminated. In both cases the laminations of the stator and back iron assured good distribution of flux throughout the magnetic materials. For economy in the construction of long stretches of rail, it would be advantageous to use solid rather than laminated steel for the secondary back iron of a single-sided LIM (SLIM). In this SLIM experiment, the nature and magnitude of the mechanical stresses involved would not have unduly complicated the design or construction of a laminated wheel,

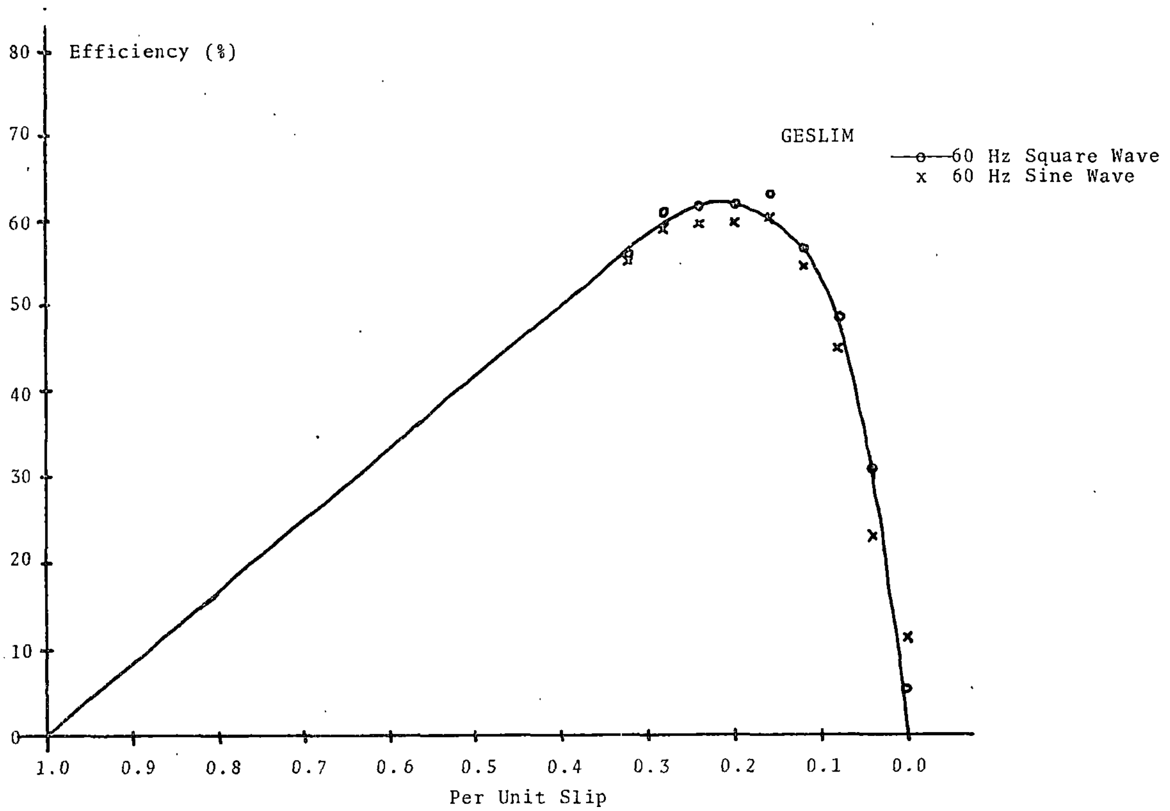

FIGURE 4-6. EFFICIENCY AS A FUNCTION OF SLIP FOR 60 Hz SINE WAVE AND SQUARE WAVE CURRENT - GESLIM.

but the wheel was made solid in order to gain reliable information on performance with, what should be, the most practical rail configuration. Now, however, the magnetic flux is not well-distributed, but, rather, is confined to a small layer near the air gap by the skin effect. Since the steel will saturate at the resultant high flux densities, nonlinear effects should be expected in the measurements.

To gain an appreciation of how strong the nonlinearities might be, the skin depth in the steel material of the wheel (AISI-1020) is given in Table 4-2 for the range of relative permeabilities and slip frequencies expected to occur. The best available value for the conductivity of this steel is approximately 5 x 10^6 s/m.

For a typical case, at 60 Hz line frequency and 24% slip, the maximum yoke flux density is approximately 0.5 tesla rms (the effective yoke height is 1.865 in.). Assuming that the steel is quite saturated in the skin layer, and that the relative permeability $\mu_r = 100$ the skin depth will be about 0.2 in. The back iron flux will be on the order of 75% of the yoke flux. Assuming that all of this flux is confined to the skin layer, the flux density would be 4.7 tesla rms. This is obviously well beyond any reasonable level of saturation, and indicates that the layers of the back iron close to the gap are heavily saturated with much flux spilling over into deeper layers. Application of mathematical analysis to this situation is extremely difficult and complex, but such

TABLE 4-2. SKIN EFFECT IN SOLID STEEL WHEEL

	PART A:	Skin Depth at Various Slip Frequency and Relative Permeability (in inches)					
f Slip Hertz		1	3	10	30	100	300
μ_r	10	2.42	1.40	0.767	0.443	0.242	0.140
	30	1.40	0.767	0.443	0.242	0.140	0.077
	100	0.767	0.443	0.242	0.140	0.077	0.044
	300	0.443	0.242	0.140	0.077	0.044	0.024
	1000	0.242	0.140	0.077	0.044	0.024	0.014
	3000	0.140	0.077	0.044	0.024	0.014	0.008
	PART B:	Relative Slip (%) Corresponding to Slip Frequencies of Part A					
Line	60	1.7	5.0	16.7	50.0	166.7	500.0
Frequency	150	0.7	2.0	6.7	20.0	66.7	200.0
Hertz	300	0.3	1.0	3.3	10.0	33.3	100.0

methods are being actively pursued.(4) Approximate methods utilizing average permeability functions(5,6) or idealized saturation characteristics(7) are also being developed.

While the analytical tools for reliable performance prediction are not yet in hand, some immediate (or first-order) observations may be made. The very hard saturation of the layers adjacent to the air gap ought to manifest itself crudely in two ways: (1) an effectively larger air gap, and (2) an increased conductivity of the rail proportionate to the thickness of the current carrying region of the back iron and its electrical conductivity. In the example just discussed, one should then increase the conductivity of the aluminum rail from 23.6 s/m to 34.3 s/m (45%) for the region with back iron. An increase in air gap, however, is not really appropriate, since even with $\mu_r = 30$ the increase would be less than 1%.

---

4. Jufer, M. and Apostolides, A., "An Analysis of Eddy Current and Hysteresis Losses in Solid Iron Based on Simulation of Saturation and Hysteresis Characteristics," Transactions PAS, Vol. 76 (Nov/Dec 1976), 1786-94.

5. Sakabe, S. and Iwamoto, M., "Experiment on High Speed Linear Induction Motor with a Saturable Iron Secondary," Electric Machines and Electromechanics, Vol. 2, No. 1 (Oct/Dec 1977), 25-36.

6. Boldea, I. and S.A. Nasar, "Improved Performance of High-Speed Single-Sided Linear Induction Motors: A Theoretical Study," Electric Machines and Electromechanics, Vol. 2, No. 2 (Jan/Mar 1978), 155-66.

7. Elliott, D.G., "SLEM Program, 7th Quarterly Report," (June 15, 1977), Section 3.

On the other hand, the flux must not only get to the iron from the airgap but must traverse the back iron in the skin layer to reach the next pole.

Although there will be a dependence on slip frequency, the effective air gap and rail conductivity may depend only on excitation level and the saturation flux of the back iron. The reason for this is that most of the flux (and current) would exist in heavily saturated layers. The unsaturated underlying layers in which normal skin effect occurs would be carrying only a small fraction of the total flux.

In a machine with end effects, the distribution of air gap and yoke flux will not be uniform. The air gap flux will be close to zero near the head end of the stator, rise slowly to a maximum value near the middle or past the middle, and then drop off again (as in Figure 4-7). The yoke flux will vary in an even more marked way. In the ideal case of a uniform air gap flux magnitude, the yoke flux distribution will resemble a rectified sinusoid. Thus, not all parts of the solid back iron will be subjected to a high flux density. Also, not all parts of the machine are at maximum flux density at the same time. The impact of skin saturation may not, therefore, appear as strongly in the overall machine performance as it would locally.

A third factor which would tend to mask or ameliorate this effect of skin saturation is that, even at very high, but less than

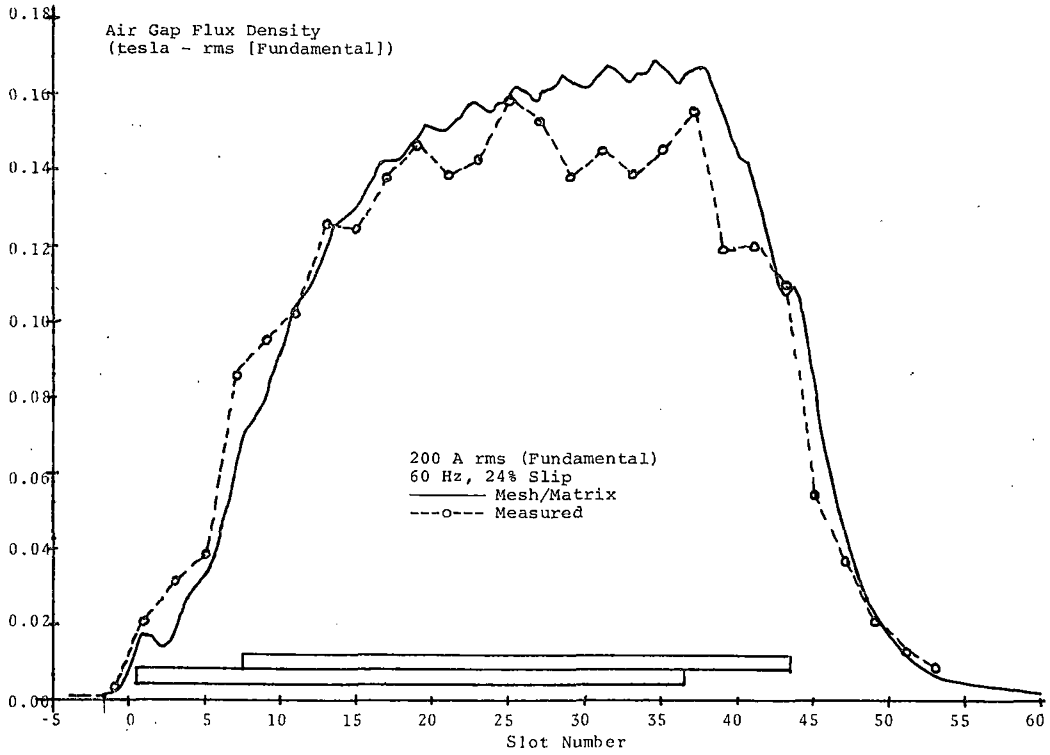

FIGURE 4-7. FLUX DENSITY DISTRIBUTION - GESLIM

intrinsic, flux levels, the permeability of the iron will still be large, relative to vacuum. Even a relative permeability of ten would be enough to keep the fields relatively straight. The additional effective air gap would be on the order of 0.02 in. which is almost negligible.

This conception of the effect of solid back iron conductivity and saturation effects is simple and appealing; it has been successfully applied to the analysis of annular electromagnetic pumps with solid iron cores.(8) In this experiment, however, only weak evidence of nonlinearity could be found. Figure 4-8 is a plot of measured thrust as a function of current squared with 60 Hz excitation at 24% slip. In any linear model of a LIM (ignoring saturation effects), this plot should be a straight line passing through the origin. Most of the plot is indistinguishable from a straight line. There is some falling off (about 6%) at the highest excitation levels (295 A and 325 A), which may be a manifestation of skin saturation.

A similar plot of the "radial" force (Figure 4-9) also shows some dropping off at high excitation, but the last point at the highest excitation lies on the linear characteristic. The results, while suggestive, do not yield unambiguous confirmation of skin saturation. Since both thrust and "radial" force are totals over

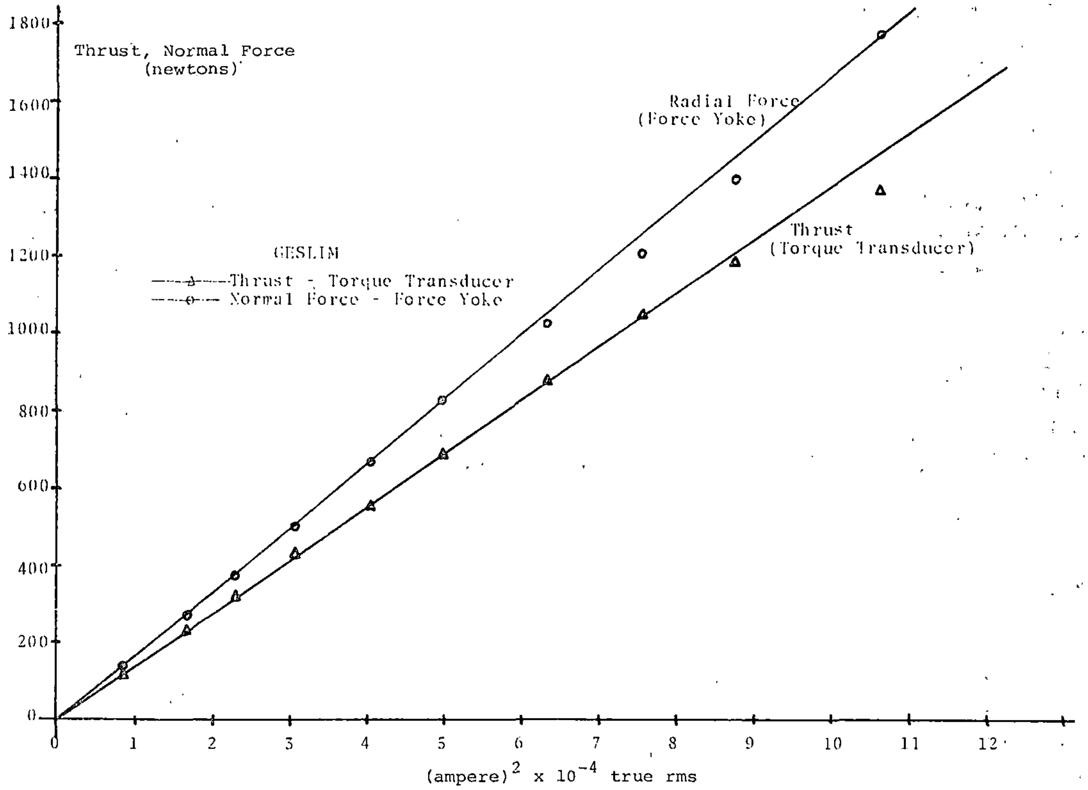

FIGURE 4-8. THRUST AND RADIAL FORCE AS A FUNCTION OF (CURRENT)^2 AT 60 Hz, 24% SLIP - GESLIM.

---

8. Griffin, W.D., Private communication.

the entire air gap surface, an examination of local flux density should show saturation effects more clearly.

A plot of air gap and stator yoke flux density as a function of stator current is given in Figure 4-9. This data is taken close to the point of maximum flux density in the machine. The flux vs. current (magnetization) curves are remarkably similar to the normal force vs. current squared curves (and to the thrust vs. ampere-squared curves, except for the last point), indicating that the local effects are no more or less severe than the general, or average, effect. Note that the yoke and tooth flux (approximately 2.4 times the air gap value) densities do not exceed 0.6 tesla rms; hence, no saturation effects can be attributed to the stator. On the other hand, with 14.4 Hz slip frequency in the secondary, there must be some skin saturation in the solid iron.

In order to confirm the origin of the saturation effects in the secondary, a magnetization curve at zero slip (approximately zero slip frequency) is presented in Figure 4-9 for comparison. Under these conditions, the skin depth in the solid should be very large; hence, there should be no skin saturation. The zero slip curve does, indeed, show no saturation, such as that observed at 24% slip, despite a 30% higher flux.

The yoke and air gap flux density at 365 Hz, 24% slip, is presented in Figure 4-10. No evidence of skin saturation can be detected in this data; however, the yoke flux density does not go above 0.36 tesla rms, even at 400 A excitation. Saturation at 60 Hz, 24% slip, did not begin to appear until a yoke flux density of 0.36 tesla had been reached. The thrust as a function of current squared is shown in Figure 4-11. The linearity of this relationship confirms the absence of observable skin saturation at this frequency. (Note that the machine reached its specified maximum speed and thrust in this data.)

Two conclusions can be drawn from the data examined so far. First, the behavior of the thrust, radial force, and flux densities is highly suggestive of a nonlinear effect having its origin in the back iron. Second, the effect is weak (in this experiment) and affects performance only at maximum excitation. Since the machine is linear over most of its operating range, scaling may be used for all data taken at less than 300 A excitation levels.

PERFORMANCE

Figure 4-12 summarizes the principal results of the thrust measurements. Data were taken at speeds up to the limit of 111 m/s at frequencies of 60, 150, and 300 Hz. Other frequencies were used but, for clarity, are not shown here (see appendix). The mesh/matrix(9) prediction for each frequency is plotted to the same scale. It may be noted that the agreement for the low slip portion of each characteristic is quite good and with zero thrust occurring at or quite close to synchronous speed. Although it was not possi-

---

9. Elliott, D.G., "Matrix Analysis of Linear Induction Machines," FRA-OR & D-75-77 (September 1975).

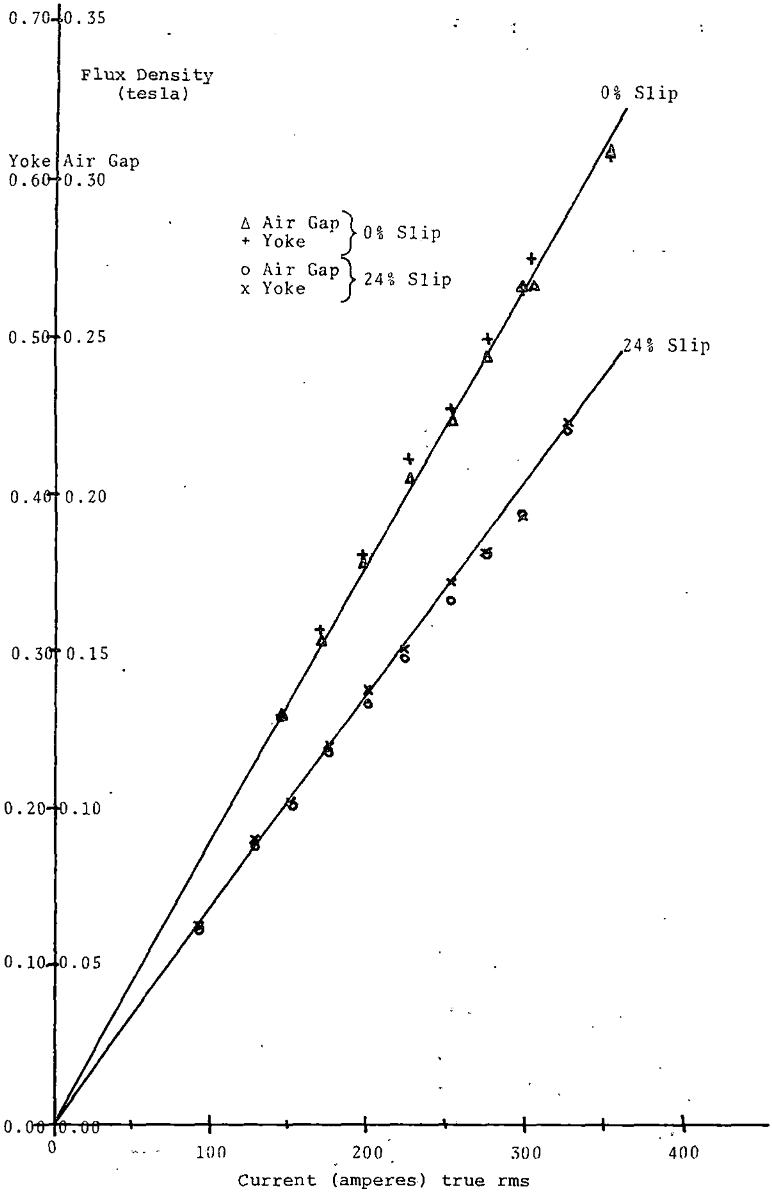

FIGURE 4-9. FLUX DENSITY AS A FUNCTION OF CURRENT AT 60 Hz, 24% SLIP AND 0% SLIP (AIR GAP AND YOKE) - GESLIM.

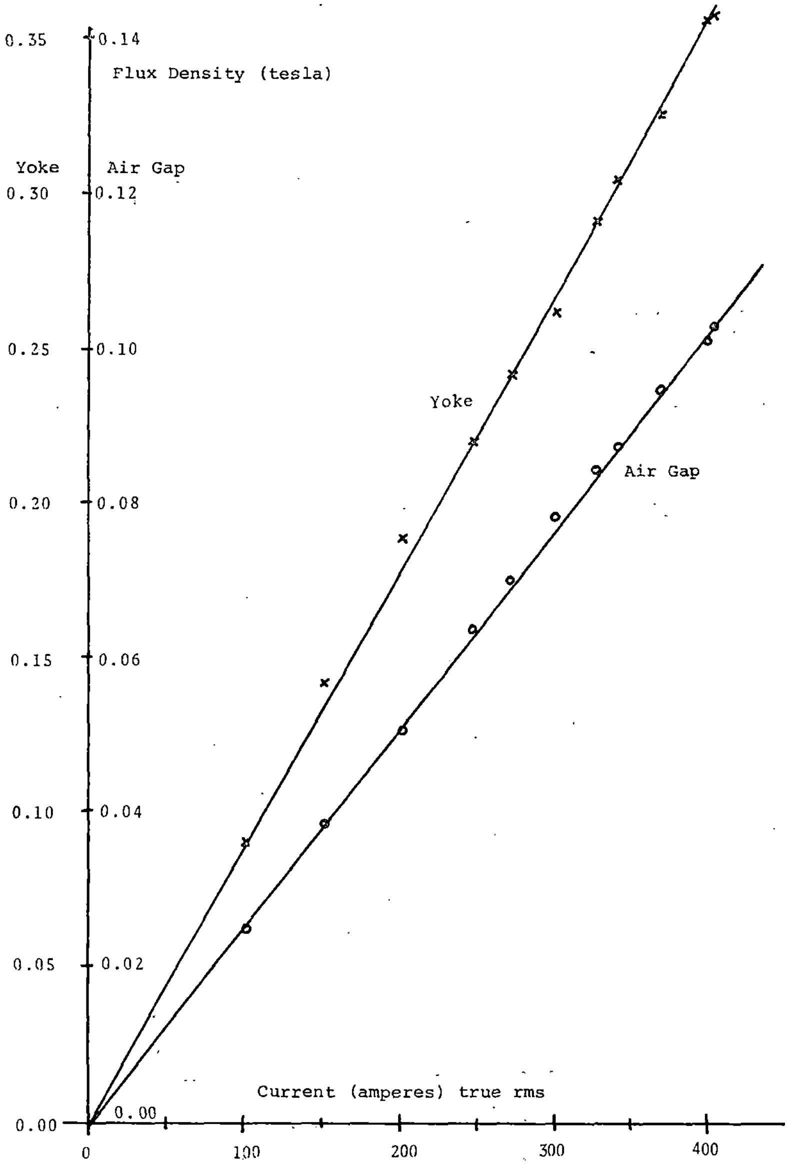

FIGURE 4-10. FLUX DENSITY AS A FUNCTION OF CURRENT AT 365 Hz, 24% SLIP (AIR GAP AND YOKE) - GESLIM.

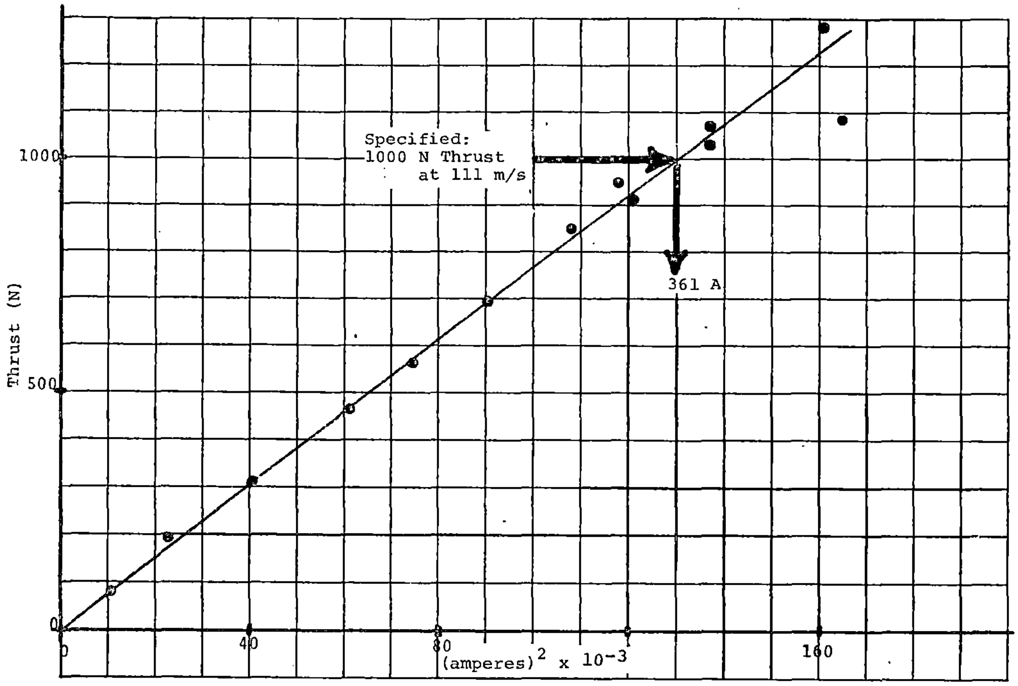

Thrust vs. (Current)^2

FIGURE 4-11. SLIM CHARACTERISTICS 365 Hz SQUARE WAVE CURRENT 24% SLIP, 111 m/s.

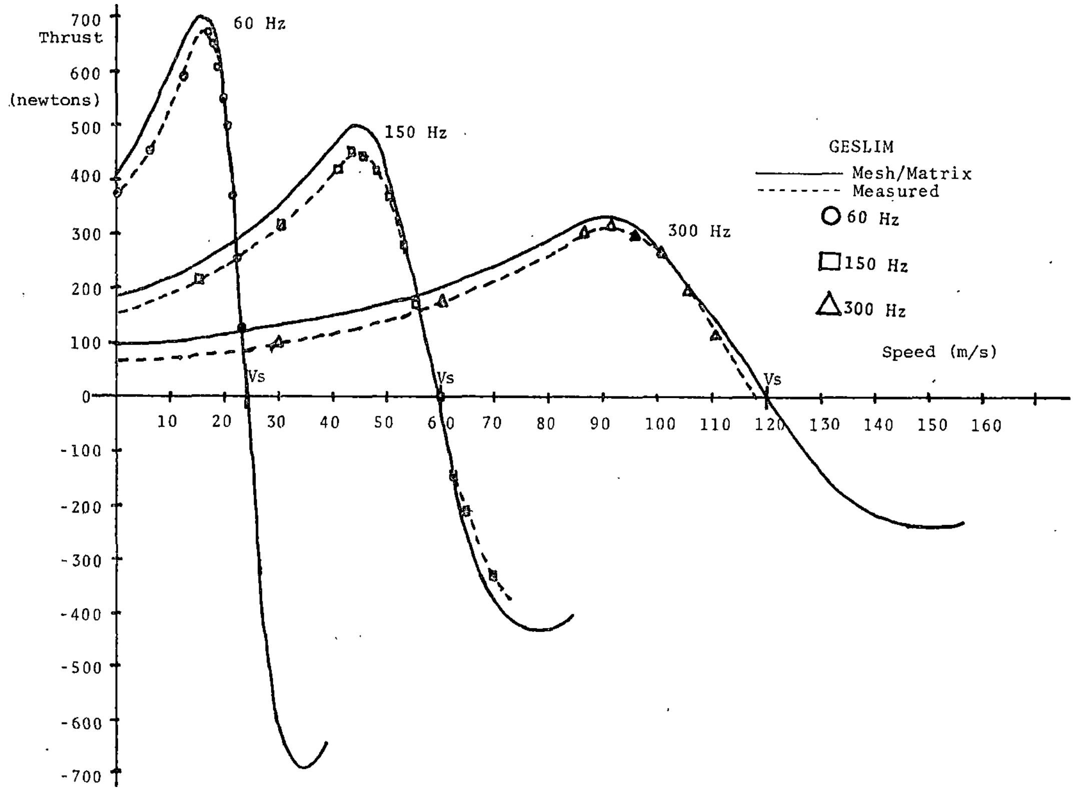

FIGURE 4-12. THRUST AS A FUNCTION OF SPEED.

ble to get measurements at the 300 Hz synchronous speed, the trend of the data is similar to that at 60 Hz and 150 Hz. This is unlike previous data(9) (Figure 61, p. 210) where, at the highest speeds, the point of zero thrust was considerably different from synchronous. This is most likely due to the length of winding and iron being almost the same in this experiment, whereas, in the previous experiment, the stator was several slots larger than the winding, giving rise to different space harmonics. In the expanded plot for 60 Hz (Figure 4-5) the measured thrust is, in fact, not zero at synchronous speed. It is not appropriate to give too much weight to this one point in view of the possibility of instrument errors and the uncertainties in the friction and windage thrusts subtracted to obtain this point.

The second outstanding feature of this plot is the constant offsets between the mesh/matrix prediction and the data at medium and high slips. This result is very similar to that observed in previous experiments where a double-sided motor was converted to single-sided with identical geometry and solid back iron,(10) and the performances compared. It is probable that the decrease in thrust at high slips is due to an apparent increase in rail conductivity caused by currents flowing in the solid iron wheel. The offset is consistent with an effective conducting layer of steel 0.1 in. thick, which is about the thickness of saturated skin layers that are expected. Further elaboration of these results must wait on the development of better analytical tools for handling the effects of solid steel back iron. Note that a simple change in rail conductivity is not sufficient to explain the results.

The efficiency as a function of speed at the same frequencies is shown in Figure 4-13 and compared to prediction. Agreement of prediction and measurement is remarkable. It has been demonstrated(11) that the mesh/matrix method is among the most conservative of the several linear motor analysis techniques currently in use; however, the calculation does not take into account core losses, back iron losses, skin saturation and harmonic losses, all of which are present in the test.

The air gap flux distribution (at 60 Hz, 24% slip) has been referred to previously (Figure 4-9). Similar plots for 150 Hz and 300 Hz, all at 24% slip, are shown in Figures 4-14 and 4-15. The measured flux distributions are shown with the mesh/matrix prediction. The configuration of the double layer winding is also shown to establish a spatial reference. Agreement with prediction is reasonably good at 60 Hz. Some difference must be expected, since the flux coils are immersed in not only the air gap flux but the slot leakage fringing flux, which is quite significant because of the large slot-to-tooth ratio and the large air gap. The net current in each adjoining slot is different in magnitude and phase,

---

10. Kliman, G.B. and Coho, O.C., Unpublished data.

11. Stickler, J.J., "A Study of Linear Induction Motor Characteristics: The Mosebach Model," FRA-OR & D-76-253 (May 1976) (interim).

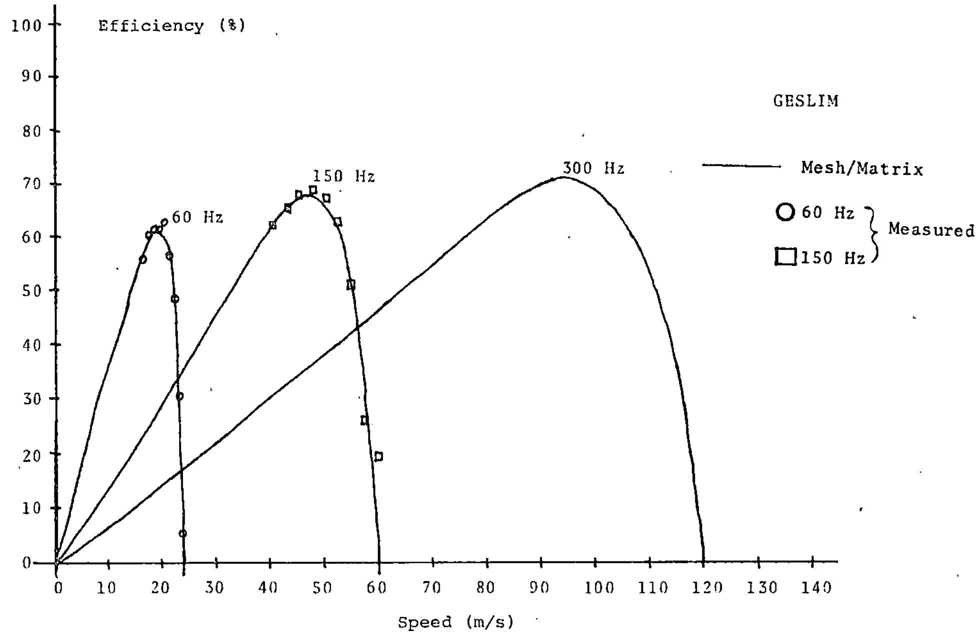

FIGURE 4-13. EFFICIENCY AS A FUNCTION OF SPEED.

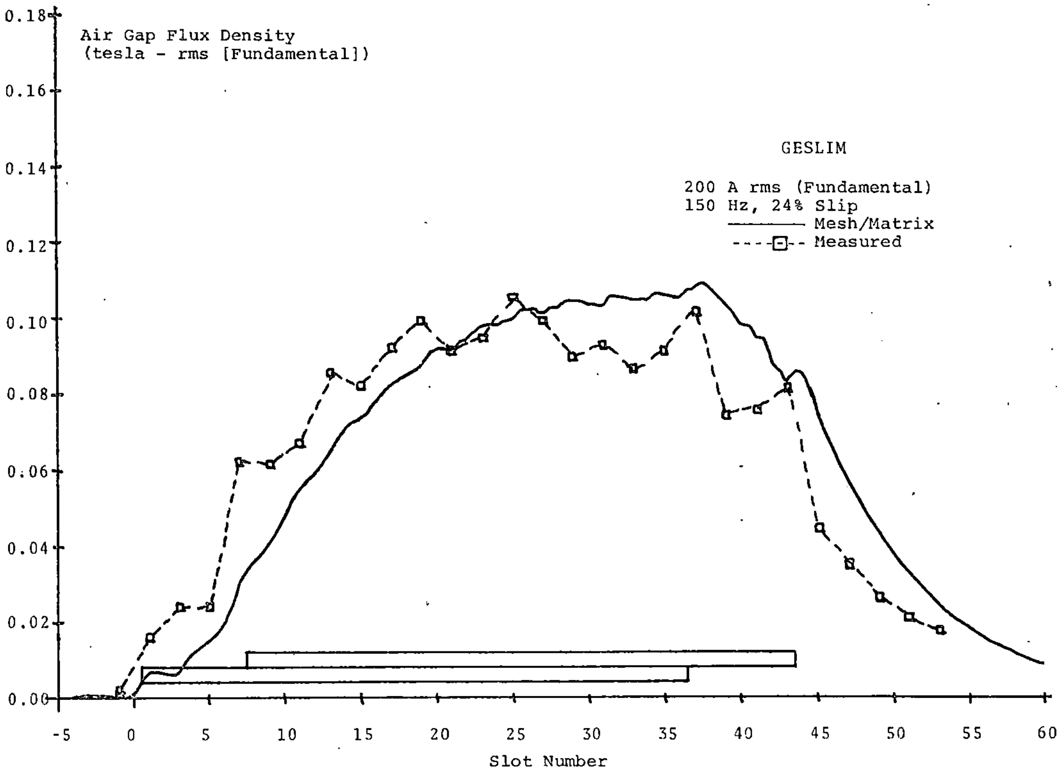

FIGURE 4-14. FLUX DENSITY DISTRIBUTION.

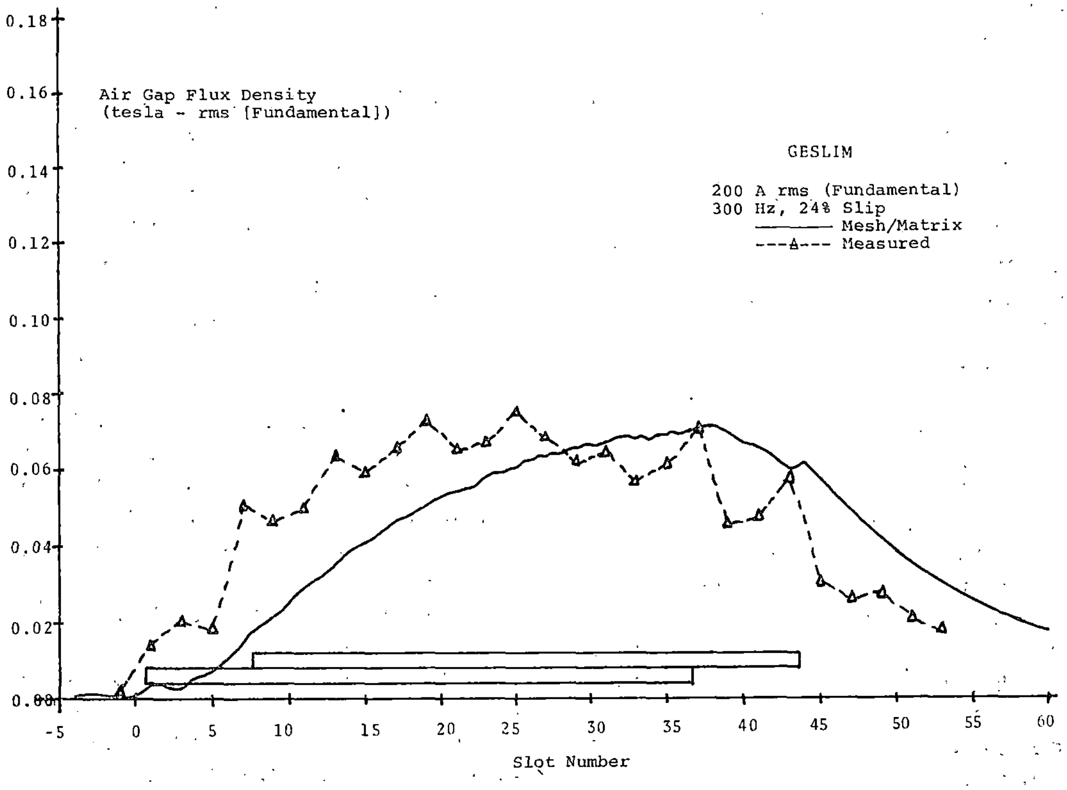

FIGURE 4-15. FLUX DENSITY DISTRIBUTION.

so that there is no opportunity for slot leakage flux cancellation. A second factor leading to differences is that the mesh/matrix method predicts the flux at the center line of the equivalent double-sided machine, with the rail approximated as a ladder network of thin wires, whereas the flux coils are located at the stator. The 60 Hz data is consistent with previous results,(12) where flux sensors placed slightly above the stator surface indicated flux densities somewhat lower than those predicted. In this experiment, however, the sensors were designed to measure the total flux entering the air gap and to cancel out much of the leakage flux, leading to closer agreement between prediction and measurement.

Features of the flux distribution not previously observed are the rapid decay of flux in the latter half of the machine and the high flux near the entry end. These differences are small enough at 60 Hz to be attributable to instrument error. But as frequency (and speed) is increased, both of these effects become more pronounced, and especially so for the entry end flux. There is no ready explanation for these phenomena, but two mechanisms may be proposed. First, it has been observed that a small amount of flux can be implanted in the steel wheel at the exit end of the machine and carried around to the entry end. This small flux may preset the flux at the entry end and allow a faster rise of flux than normal. Second, skin saturation will occur in the latter half of the machine, where the yoke flux builds up to high values

---

12. Kliman, G.B. and Elliott, D.G., "Linear Induction Motor Experiments in Comparison with Mesh/Matrix Analysis," Transactions PAS, Vol. 93, No. 5 (Sept/Oct 1974), 1624-33.

leading to a limit on air gap flux in that region and shifting flux to the entry end.

The final item in this comparison of measurement and prediction is the normal forces. The measurement of forces other than thrust in a wheel experiment is fraught with great difficulties. A number of attempts to measure normal force have been made in other laboratories, but these efforts have not met with great success. In this experiment, a force measuring yoke was devised to measure, not only normal force and its associated pitch torque, but forces in all six degrees of freedom of the stator for various misalignments and displacements (discussed elsewhere in this report).

Because of the curvature of the stator, there will be errors introduced into the measurement of thrust and normal forces by means of sensors mounted on the force yoke. In using force yoke data to determine thrust and normal force, the readings of the vertical and horizontal force sensors are combined to form the net force vector on the stator (magnitude, direction, and point of action). The net force vector is then resolved into a tangential component corresponding to thrust and a radial component corresponding to normal force. The point of action then yields the pitch torque. In the limit of a very short stator arc (or very large radius), these calculations will yield the true values of thrust and normal force. In this experiment, the stator occupies a 79° sector--large enough to cause significant error. With some effort, this error can be calculated for simple distributions of true thrust and normal force.

The transducer forces resulting from realistic distributions of thrust and normal force can be calculated with the mesh/matrix program. A general derivation of the force yoke performance, examples of ideal linear distributions and results from mesh/matrix calculations are presented in Section 5.

The general conclusion to be drawn from Section 5 is that prediction of thrust will be accurate (except for instrument error and friction) under all conditions. Prediction of normal force (and pitch torque) will be reliable only when the magnitude of the normal force is greater than that of the thrust.

Figure 4-16 is a comparison of thrust derived from shaft torque measurements with that derived from the force yoke. If the deviations at low current (and force) are attributed to stick-slip, hysteresis, etc., then the remaining points are very closely linear in current squared. If these points are offset to pass through the origin, it would represent a linear characteristic with a -5.9% error. Since, in principle, the thrust prediction should be exact, there must be a calibration deviation or unidentified frictional force affecting the data. In the Section 5 it is demonstrated that, in principle, valid normal force predictions should be about 3% low. Then it may be expected that normal force data will be about 9% low in the experiment.

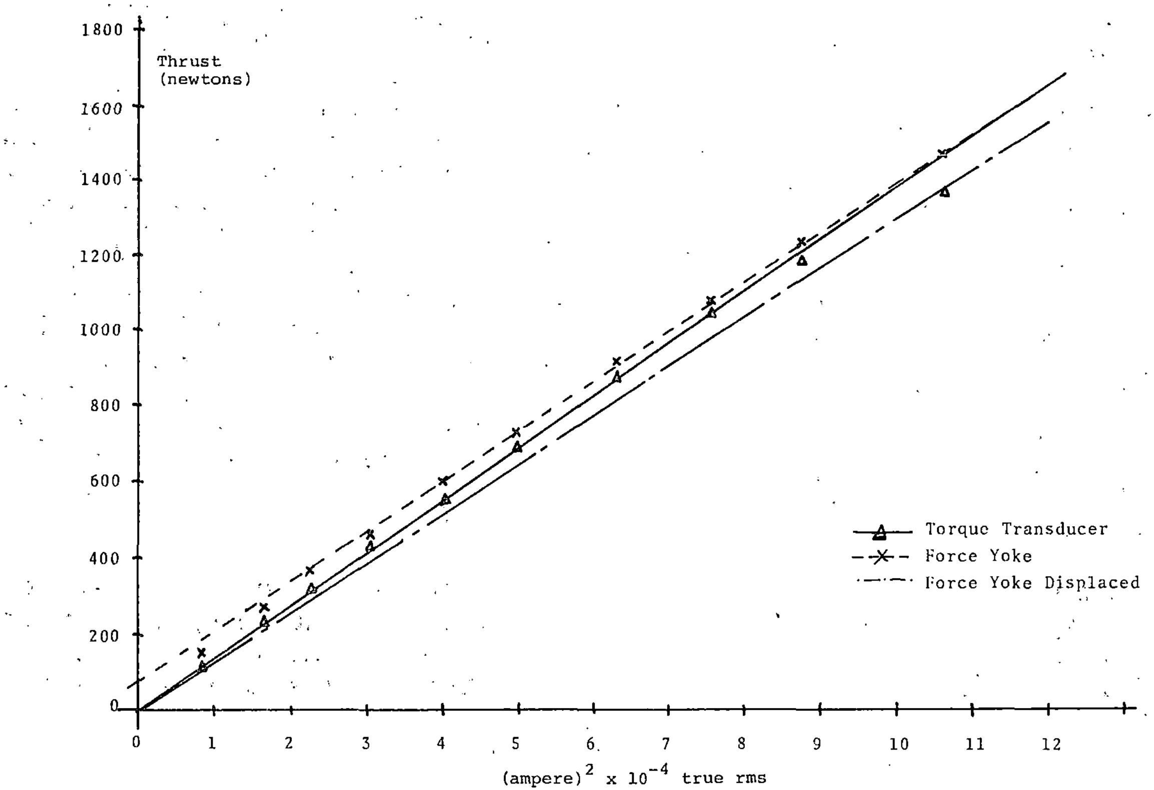

FIGURE 4-16. THRUST AS A FUNCTION OF (CURRENT)^2 AT 60 Hz, 24% SLIP - COMPARISON OF FORCE YOKE AND TORQUE TRANSDUCER - GESLIM.

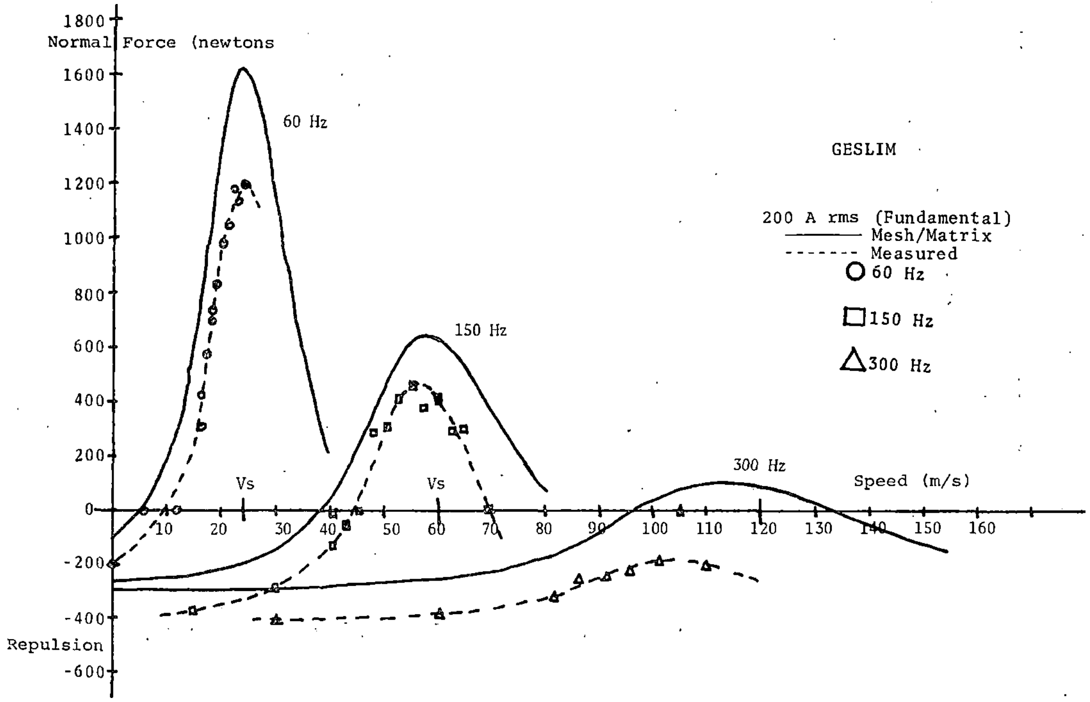

FIGURE 4-17. RADIAL FORCE (ATTRACTION) AS A FUNCTION OF SPEED - GESLIM.

Normal force (actually the radial component) is plotted in Figure 4-17 as a function of speed at 200 A for 60 Hz, 150 Hz, and 300 Hz, along with the mesh/matrix prediction. It is evident that the general character of the normal forces is consistent with the prediction but differs considerably in magnitude. The thrust and normal forces are calculated from the same predicted values of flux density and current. Since these values predicted close to the proper values of thrust, they must be close to correct, at least on the average.* With the average magnetic flux in the air gap close to that predicted, the attraction force must be close to correct also. All of the deviation from prediction is in the direction of increased repulsion force, which is consistent with a correct attraction and an incorrect repulsion. Since the average rail current under the stator must be close to correct, the only source of the additional repulsion force is most likely in the neglected solid iron currents, the interaction of sidebars and end windings, and possibly slot fringing fluxes.

It may be seen that both the normal force (Figure 4-17) and pitch torque (Figure 4-18) as measured are considerably less than that predicted by mesh/matrix. The amounts by which they differ, while in the direction predicted in Section 5, are considerably

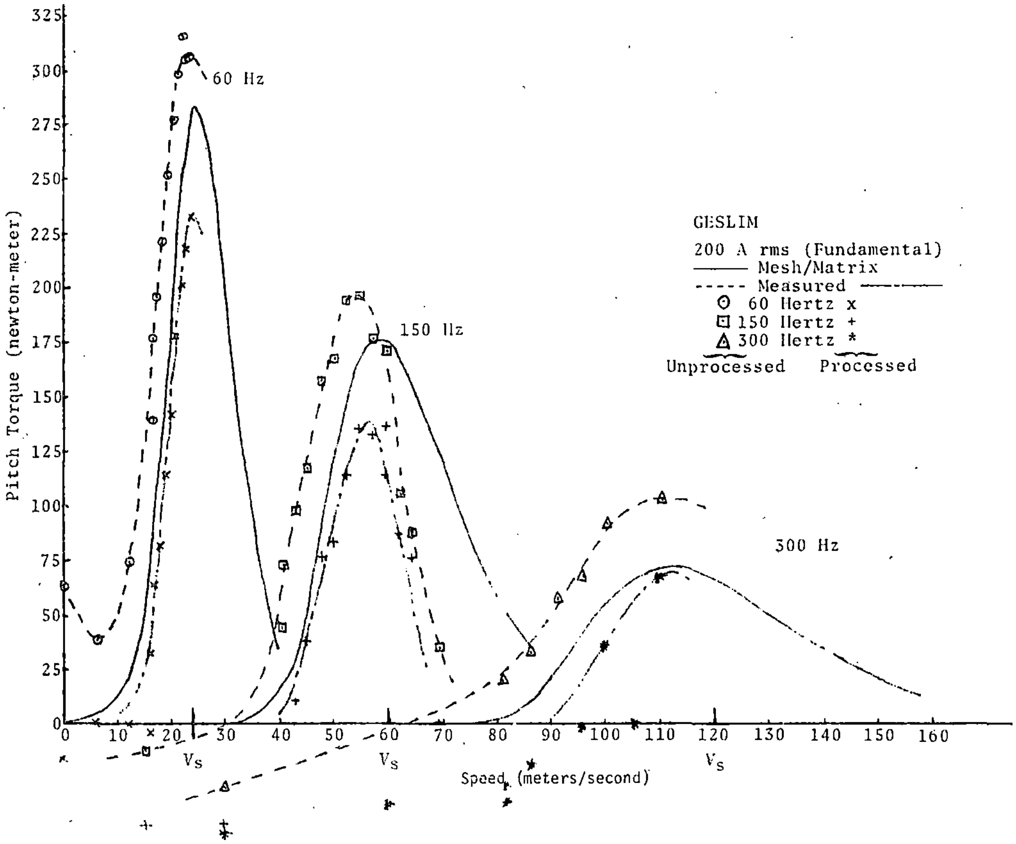

FIGURE 4-18. PITCH TORQUE AS A FUNCTION OF SPEED.

---

*Elliott(9) points out that the averages for normal force calculation should be done in a different manner.

larger. Neglected winding forces can account for 10 to 20% of the total and may be a significant factor in the discrepancies. In Section 5 it is shown that the force resolution can yield inaccurate or misleading results for normal force and pitch torque when the thrust exceeds the normal force. This is amply confirmed by the obviously incorrect results at high slips shown in Figures 4-17 and 4-18.

A comparison of the pitch torques found through the force resolution method of Section 5 (processed) and the "raw" pitch torque, including thrust effects (unprocessed) is shown in Figure 4-18. The effect of the thrust in increasing the apparent pitch torque on the curved stator is quite apparent. It is clear that much additional work needs to be done in both theoretical prediction and the measurement of normal forces and pitch torques.

REFERENCES

1. Ward, E.E., "Inverter Suitable for Operation Over a Range of Frequency," Proceedings IEEE, Vol. III, No. 8 (August 1964), 1427-34.

2. Cornell, E.P. and Lipo, T.A., "Modeling and Design of Controlled Current Induction Motor Drive Systems," Transactions IAS, Vol. IA-13, No. 4 (July/August 1977), 321-29.

3. Kliman, G.B., "Harmonic Effects in PWM Inverter-Induction Motor Drives," IAS Conference Record, 7th Meeting (October 1972).

4. Jufer, M. and Apostolides, A., "An Analysis of Eddy Current and Hysteresis Losses in Solid Iron Based on Simulation of Saturation and Hysteresis Characteristics," Transactions PAS, Vol. 76 (Nov/Dec 1976), 1786-94.

5. Sakabe, S. and Iwamoto, M., "Experiment on High Speed Linear Induction Motor with a Saturable Iron Secondary," Electric Machines and Electromechanics, Vol. 2, No. 1 (Oct/Dec 1977), 25-36.

6. Boldea, I. and Nasar, S.A., "Improved Performance of High-Speed Single-Sided Linear Induction Motors: A Theoretical Study," Electric Machines and Electromechanics, Vol. 2, No. 2 (Jan/Mar 1978), 155-66.

7. Elliott, D.G., "SLEM Program, 7th Quarterly Report," (June 15, 1977), Section 3.

8. Griffin, W.D., Private communication.

9. Elliott, D.G., "Matrix Analysis of Linear Induction Machines," FRA-OR & D-75-77 (September 1975).

10. Kliman, G.B. and Coho, O.C., Unpublished data.

11. Stickler, J.J., "A Study of Linear Induction Motor Characteristics: The Mosebach Model," FRA-OR & D-76-253 (May 1976) (interim).

12. Kliman, G.B. and Elliott, D.G., "Linear Induction Motor Experiments in Comparison with Mesh/Matrix Analysis," Transactions PAS, Vol. 93, No. 5 (Sept/Oct 1974), 1624-33.

Section 5

VALIDITY OF THRUST, NORMAL FORCE, AND PITCH TORQUE FROM FORCE YOKE DATA

INTRODUCTION

The objective of the force yoke measurement system is to derive thrust, normal force, and pitch torque from the various sensors. In this discussion the motor is assumed to be in its nominal (undisplaced) position so that there will be no lateral forces and no roll or yaw torques. If the motor and track were flat, as in the real application, there would be no ambiguity in interpreting the sensor outputs (Figure 5-1).

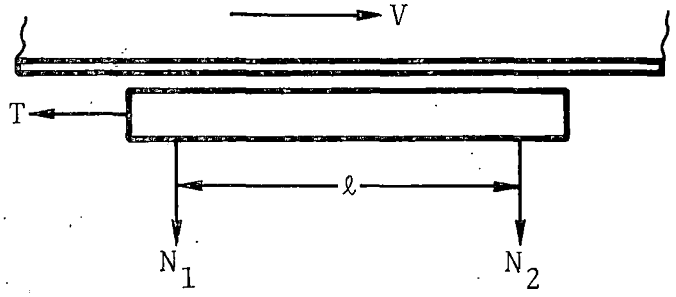

FIGURE 5-1. FLAT MOTOR FORCE SENSING.

The thrust T is given by the force with which the motor pushes on the horizontal force sensors. The net normal force of attraction is given by the sum $N_1 + N_2$. The net pitch torque M about the center line of the motor is given by $(N_1 - N_2)\ell/2$. Because of the constraints of a laboratory test, however, both the motor and rail are curved (Figure 5-2).

Now it is clear that components of the thrust will influence the normal force sensors and that components of the normal force will influence the thrust sensors. Furthermore, some components of the thrust and of the normal force will be absorbed irretrievably in the rigid structure of the stator. Since those sensor outputs can no longer be directly identified with thrust and normal forces, they are labeled only horizontal force F_x and vertical forces F_{y1} and F_{y2}.

An additional complication of the experimental setup is the location of the horizontal force sensor at some distance below the stator.

RESOLUTION OF FORCES

Resolution of the forces is done approximately by first forming a resultant force and point of action. This resultant force is then resolved into components parallel and perpendicular to the stator surface at the point of action (assumed at the stator surface). These components are then identified with the thrust and

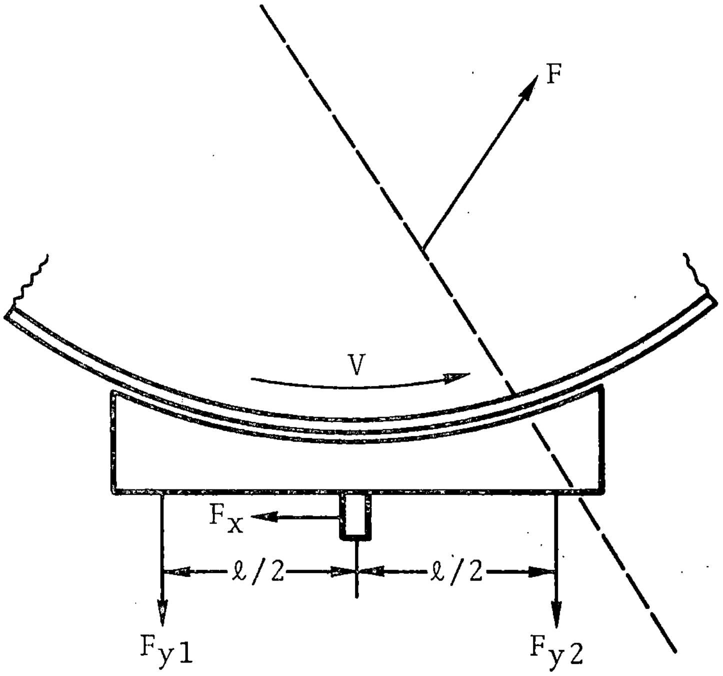

FIGURE 5-2. SECTOR MOTOR FORCE SENSING.

normal force, respectively. By knowing only the values of F_{y1}, F_{y2} and F_x in Figure 5-2, the net equivalent force on the stator, F, can be formed.

$$F = [F_x^2 + (F_{y1} + F_{y2})^2]^{1/2} = \frac{F_x}{\sin \beta} \tag{1}$$

The point of action of this equivalent forces can only be fixed to lie on the dashed straight line in Figure 5-2. Since, in the case of the flat machine, the point of action must be at or near the stator, it must be that the point of action for the equivalent force of the sector machine must be near the stator (or rail). For simplicity the point of action is assumed to be on the surface of the stator. The position of the point of action can now be determined (Figure 5-3).

The net moment about "0" exerted by the sensors is defined as M_p.

$$M_p = (F_{y2} - F_{y1})\ell/2 + F_x p \tag{2}$$

This moment must be balanced by the moment exerted by the equivalent force at angle θ' on the surface of the stator.

$$M_p = (F_{y2} + F_{y1}) r \sin \theta' - F_x r(1 - \cos \theta') \tag{3}$$

Combining Equation (2) and Equation (3) yields the condition for determining θ' and also α', since β comes from the ratio of vertical and horizontal forces.

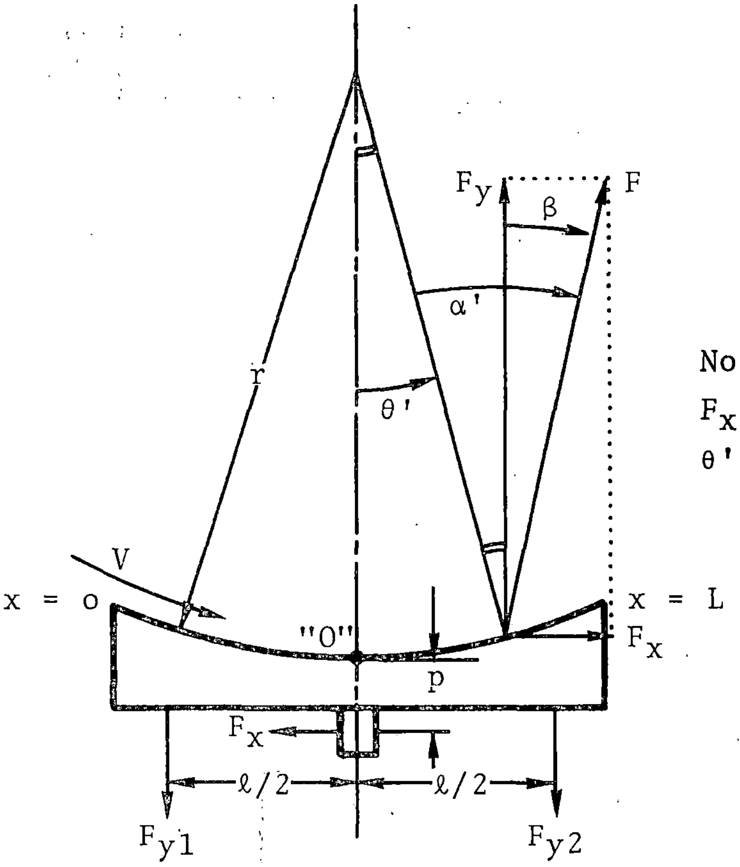

Note:
$F_x<0;F_y>0;F>0$
$\theta'<0;\beta<0;\alpha'<0$

FIGURE 5-3. COORDINATES FOR FORCE RESOLUTION.

$$\beta = \arc\tan \frac{F_x}{F_{y1} + F_{y2}} \tag{4}$$

$$\sin \alpha' = \sin(\beta + \theta') = \left[\frac{F_{y2} - F_{y1}}{F_x} \frac{\ell}{2r} + \frac{r + p}{r} \right] \sin \beta \tag{5}$$

The resultant force, F, may now be resolved into radial and tangential components.

$$T' = F \text{ (tangential)} = \text{"thrust"} = F \sin \alpha' \tag{6}$$

$$= F_x(1 + p/r) + (F_{y2} - F_{y1})\ell/2r$$

$$N' = F \text{ (radial)} = \text{"Normal Force"} = F \cos \alpha' \tag{7}$$

$$\text{Center of attraction} = r\ \theta' \tag{8}$$

$$\text{Moment about "O"} = r\ \theta'\ F \cos \alpha' = r\ \theta'\ N' \tag{9}$$

[Note: In the data printouts "location of resultant" corresponds to θ' (which is reversed in sign). The printed pitch torque, however, is not found by Equation (9) but, rather by Equation (2) with p = 0; hence it is not the true resolved pitch torque which is given by Equation (9).]

VERIFICATION BY GIVEN FORCE DISTRIBUTIONS

Assume the true thrust distribution and normal force distribution are t(x) and n(x), respectively, with x measured on the surface of the stator from the entry end (Figure 5-4).

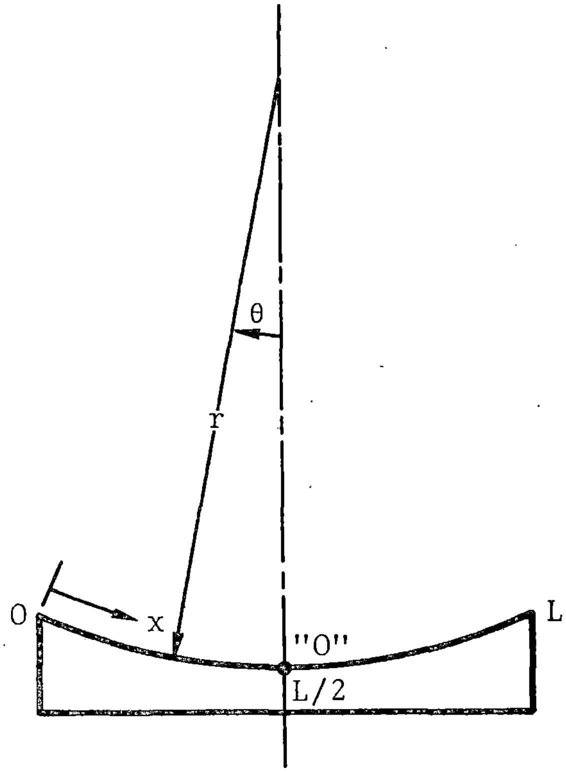

FIGURE 5-4. COORDINATES FOR FORCE CALCULATION.

The true thrust is given by T.

$$T = \int_0^L t(x)\,dx \qquad (10)$$

The true normal force is given by N

$$N = \int_0^L n(x)\,dx \qquad (11)$$

and the true moment (about "0" is given by M

$$M = \int_0^L (L/2 - x)\,n(x)\,dx \qquad (12)$$

These forces may be resolved at each point on the curved stator to find the actual vertical and horizontal forces and the net moment (in this case it is convenient to take moments about the center line on the stator surface).

The net vertical force at a point is given by v(x).

$$v(x) = n(x)\cos\theta + t(x)\sin\theta \tag{13}$$

The net horizontal force at a point is given by h(x).

$$h(x) = -n(x)\sin\theta + t(x)\cos\theta \tag{14}$$

The net (clockwise) torque about "0" is given by m(x).

$$m(x) = n(x)\ r\sin\theta + t(x)r(1 - \cos\theta) \tag{15}$$

The total vertical force, V, the total horizontal force, H, and the net moment, M_p, may then be found by carrying out the integrals for particular force distributions. These results may then be put into the force resolution of Section 2 for comparison to the true values.

In the following discussion the horizontal force measurement will be assumed to take place at the stator surface center line. That is, p = 0 so that the expressions for the resolved forces can be simplified. It is also convenient to use the symbols H, V, and M_p that have been defined.

$$\beta = \arc\tan\frac{H}{V} \tag{4a}$$

$$\sin(\beta + \theta') = \sin\alpha' = \left(\frac{M_p}{rH} + 1\right)\sin\beta \tag{5a}$$

$$T' = F\sin\alpha' = M_p/r + H \tag{6a}$$

$$N' = F\cos\alpha' = \frac{V}{\cos\beta}\sqrt{1 - \left(\frac{M_p}{rH} + 1\right)^2\sin^2\beta} \tag{7a}$$

Expressions for the pitch moment become too complex to be useful.

Case 1 Uniform Distributions

Assume t(x) = t and n(x) = n; then--

$$T = tL;\ N = nL;\ M=0.$$

The reaction forces on the curved stator are--

$$H = T\,k \tag{16}$$

$$V = N\,k \tag{17}$$

$$M_p = T\,r(1 - k) \tag{18}$$

where

$$\theta_m = L/2r \text{ and } k = \frac{\sin\theta_m}{\theta_m} \tag{19}$$

Notice that as $\theta_m \rightarrow 0$, $H \rightarrow T$, $V \rightarrow N$ and $M_p \rightarrow 0$. Now put H and M_p into Equation (5) (with $p = 0$):

$$\sin\alpha' = \frac{\sin\beta}{k} \tag{20}$$

That is, α' is slightly larger than β for a reasonably sized stator that does not occupy too much arc. This puts θ' slightly positive whereas it should be zero (α=β); where α' should equal β it is now slightly larger.

Since both H and V are smaller than T and N, respectively, then the resultant force F will be smaller than the true value; but, since α' is a little larger than it should be, the thrust prediction will be compensated, whereas the normal force prediction will be worsened. In fact

$$T' = T \tag{6b}$$

Prediction of thrust is exact. This happens because the normal forces completely balance out, and the "lost" vertical components of thrust are reinserted through the torque. The normal force is more complex

$$N' = kN\sqrt{1-\left(\frac{t}{n}\right)^2\frac{1-k^2}{k^2}} \tag{7b}$$

For the experimental stator L/2 = 0.4825 m and r = 0.6795 m or θ_m = 0.71 rad (40.7°); hence

$$k = \frac{\sin\theta_m}{\theta_m} = 0.918$$

Case 1a t = n

The normal force and thrust densities are both positive, uniformly distributed, and equal in magnitude. Hence

$$\beta = 45.0^\circ;\ \alpha' = 50.4^\circ;\ \theta' = 5.4^\circ$$

$$M' = 0.06T;\ T' = T;\ N' = 0.83N$$

$$M_p = 0.06T;\ H = 0.92T;\ V = 0.92N$$

Case 1b n = 2t

The normal force and thrust densities are both positive and uniformly distributed, but the normal force is twice the thrust.

$$\beta = 26.6^\circ;\ \alpha' = 29.2^\circ;\ \theta' = 2.6^\circ$$

$$M' = 0.06T;\ T' = T;\ N' = 0.90N$$

$$M_p = 0.06T;\ H = 0.92T;\ V = 0.92N$$

Since the normal force is larger, it is less affected by the thrust.

Case 1C n = - 1/2t

This situation is characteristic of the stopped rail case (locked rotor or for slips approaching unity)

$$\beta = -63.4^\circ;\ \alpha' = -77.0^\circ;\ \theta' = -13.6^\circ$$

$$M' = 0.06T;\ T' = T;\ N' = 0.46N$$

$$M_p = 0.06T;\ H = 0.92T;\ V = 0.92N$$

Here, while the thrust is well predicted, the normal force is in error by about a factor of two. Since θ' is also getting large, there will be a large pitch torque indicated where there should be none.

While the prediction of thrust is exact, the prediction of normal force is considerably affected by the thrust. A plot of Equation (7b) for this stator illustrates the range (Figure 5-5).

It may be seen that, for conditions where the magnitude of the normal force is less than the magnitude of the thrust, the normal force prediction is in error by increasing amounts. Hence, for uniform distributions the normal force prediction is fair as long as the normal force is greater than the thrust. In all cases of uniform distribution it is more accurate to take the vertical force, V, rather than N' as the normal force prediction. The torque and resolved torque are the same but nonzero. The resolved thrust is accurate.

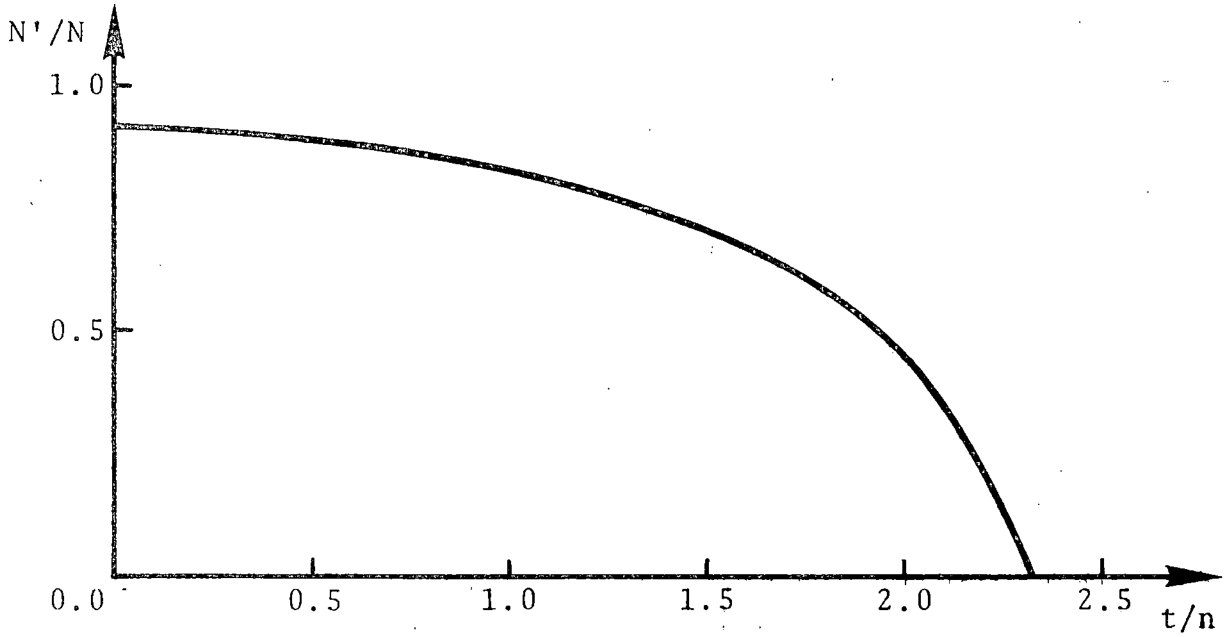

FIGURE 5-5. EFFECT OF THRUST ON THE NORMAL FORCE PREDICTION FOR UNIFORM DISTRIBUTIONS.

Case 2 Nonuniform Distributions

Assume the thrust and normal force distributions are linearly skewed as in Figure 5-6.

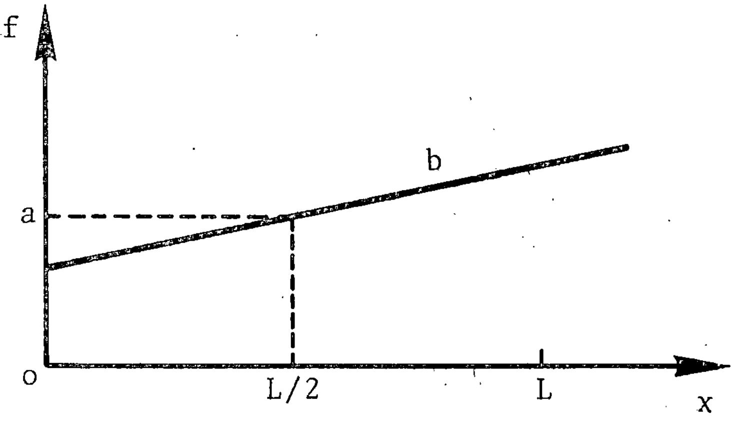

FIGURE 5-6. ASSUMED SKEWED FORCE DISTRIBUTION.

$$f = a + b(x-L/2) = a - br\,\theta \tag{21}$$

This distribution with appropriate sign and magnitude for a and b should represent most conditions occurring in practice (including Case 1). The true forces and moments can be found directly.

$$T = a_t L \tag{22a}$$

$$N = a_n L \tag{22b}$$

$$M = -\frac{1}{12} b_n L^3 \tag{22c}$$

In like manner the forces and torques on the curved stator can be found.

$$H = T k \left(1 + \frac{b_n r}{a_t}\right) - b_n L r \cos \theta_m \tag{23}$$

$$V = N k \left(1 - \frac{b_t r}{a_n}\right) + b_t L r \cos \theta_m \tag{24}$$

$$M_p = Tr(1 - k) - b_n L r^2 (k - \cos \theta_m) \tag{25}$$

Note that Equations (23) to (25) reduce to Equations (16) to (18) when the skew ($b_{t,n}$) terms are set to zero. Notice also that the skew in thrust does not affect either the horizontal force H or the torque M_p and that the skew in normal force does not affect the vertical force H. Expressions (23) to (25) may now be put into the force resolution.

Again, the resolved thrust T' = T. That is, for arbitrary linear distributions of thrust and normal force density, the force resolution will yield an exact prediction of thrust as in the case of uniform force densities. The normal force prediction N' and the pitch torque prediction M' are not so straightforward.

Case 2a $b_t = 2\, a_t/L$; $a_n = 3/2\, a_t$; $b_n = 2\, a_n/L$

This case is characteristic of operation near the 60 Hz, 0.2 slip design point. Both the thrust and normal force densities are positive and increase uniformly from the entry to the exit. The net normal force is 50% greater than the net thrust.

$\beta = 42.5^\circ$; $\alpha' = 32.6^\circ$; $\theta' = -9.9^\circ$

$T' = T$; $N' = 1.04N$; $M' = 0.77M$

$H = 1.26T$; $V = 1.52N$; $M_p = 0.72M$

Case 2b $b_t = 2\, a_t/L$; $a_n = -1/4\, a_t$; $b_n = -2\, a_n/L = 1/2\, a_t/L$

This case is characteristic of operation near the rated slip point (s = 0.25) at high speeds (f = 300 Hz). The thrust is similar to Case 2a in that it rises uniformly from zero at the entrance to a maximum at the exit. The normal force, however, is mostly repulsion and of relatively small magnitude. It has large magnitude near the entrance (where flux is low and rail current is high) to near zero at the exit. The net repulsion force is 25% of the net thrust magnitude.

$T' = T$; $N' = 1.58N$; $M' = 0.40M$

$H = 0.97T$; $V = 1.82N$; $M_p = -0.43M$

Hence, it may be tentatively concluded that, for linear skewed distributions, the thrust is accurately predicted. When the normal force is large, the force resolution will yield good predictions for it. When the normal force is small, the prediction is poor but better than accepting the raw vertical force.

The improvement in normal force prediction is most likely a result of the insertion of torque components due to the skewing, which enables recovery of additional normal force information.

Pitch torque, whether the raw torque M_p or the resolved torque M', appears to be quite doubtful, in general, but is best when the normal force prediction is good.

Case 3 General Distributions

It may be shown, by direct substitution of the integrals of Equations (14) and (15) over the stator into Equation (6a), that the thrust prediction is exact for any distribution of thrust and normal force. That is, $T' = T$ under all conditions.

Little more can be said about the general problem for normal force and pitch torque except to note that, if the functions n(x) and t(x) are expanded (power or fourier), the odd and even components will contribute to the forces as shown in Table 5-1.

Table 5-1.

CONTRIBUTION OF ODD AND EVEN COMPONENTS OF THRUST AND NORMAL FORCE TO THE FORCE YOKE OUTPUTS

	H	V	M_p
Thrust t(x)	even	odd	even
Normal Force n(x)	odd	even	odd

The results of Table 5-1 may be seen in Equations (23) to (25).

VERIFICATION BY COMPARISON TO MESH/MATRIX

The Mesh/Matrix calculation may be used as a source of non-ideal, realistic thrust and normal force distributions independent of whether or not those distributions are physically correct. Dr. D.G. Elliott has modified his mesh/matrix program to apply Equations (13) to (15) at each mesh point of the solution. In this way the net vertical and horizontal forces and the net torque for a sector motor may be built up. These quantities may then be processed through the force resolution and compared to the directly calculated values for a straight motor. The straight and sector motor force and torque predictions from mesh/matrix along with the force yoke resolution are given in Table 5-2.

TABLE 5-2 COMPARISON OF MESH/MATRIX WITH FORCE YOKE RESOLUTION

			Mesh/Matrix Prediction						Force Resolution		
			Straight			Sector					
Case #	Velocity M/s	Slip p/u	Thrust T n	Normal Force N n	Pitch Torque M n-m	Horiz. Force H n	Vert. Force V n	Pitch Torque M_p	Thrust T' n	Normal Force N' n	Pitch Torque M' n-m
					60 Hz						
142	0	1.00	407	-111	-1	389	-120	13	*/406	*	*
143	10	0.58	602	173	-13	590	123	8	602	37	4
144	18	0.25	650	1020	-125	792	857	-97	649	970	-103
145	24	0.00	-7	1610	-280	388	1490	-270	-9	1540	-273
					150 Hz						
146	0	1.00	184	-265	1	174	-258	7	184	-251	7
147	40	0.33	466	28	-14	463	-31	2	*/464	*	*
148	50	0.17	414	467	-115	552	338	-94	414	497	-111
149	60	0.00	-35	627	-176	219	584	-173	-36	623	-176
150	70	-0.17	-377	352	-121	-180	411	-136	-381	238	-97
					300 Hz						
151	0	1.00	96	-294	1	91	-284	4	96	-282	4
152	80	0.33	282	-187	1	270	-211	8	282	-194	8
153	90	0.25	328	-80	-20	340	-141	-8	328	-165	-8
154	100	0.17	278	45	-54	338	-29	-41	277	196	-70
155	110	0.08	142	98	-71	238	56	-65	142	199	-98
					6 Hz						
157	1.2	0.50	337	2510	-67	415	2360	-53	337	2370	-53
156	2.4	0.00	19	2640	-74	120	2500	-69	19	2500	-69
158	3.6	-0.50	-306	2570	-70	-196	2440	-76	-307	2430	-75
					30 Hz						
159	12	0.00	41	2160	-245	383	2020	-233	39	2060	-235

Note that, in each case that the force resolution gave an answer, the thrust prediction was either exact or within a very small percentage of being exact as predicted. In the two cases (marked with asterisks) where there was no solution, the magnitude of the normal force was one quarter (or less) of the thrust, which (as was seen in Section 3) causes large errors in the force resolution. In addition, the mesh/matrix method as it is presently constituted produces a somewhat "hashy" normal force distribution* leading to a small loss of consistency among the torques and forces. This inconsistency is not serious when the normal force is large, but in Cases No. 142 and No. 147 it resulted in requiring a solution of Equation (5) for $\sin \alpha' > 1$. In those cases the thrust may be better approximated by taking $\alpha' = 90^{\circ}$ -- that is, by setting the thrust equal to the net resultant force F. The normal force and torque in those cases is meaningless.

For the cases where the normal force magnitude is comparable or large compared to the thrust, the agreement in normal force and pitch torque produced from the force resolution with the straight motor values is quite good (Cases 144, 145, 146, 148, 149, 151, 152, 157, 156, 158, 159). In a few of these cases the pitch torque appears to be quite far off, but these are all for very small torques where the computational noise will have an effect. Case No. 150 has $|N|<|T|$, so the results are not good. Those remaining, (Cases 143, 153, 154, 155) the normal force magnitude is small compared to the thrust, and the normal force prediction is correspondingly bad.

OTHER TORQUES AND FORCES

The lateral force and yaw torque required no correction due to curvature or height. The roll torque as shown on the printouts** is, strictly, not correct since there will be additional torques resulting from the displacement of the sensors below the stator surface when there is a lateral force. Lateral forces will only appear when the stator is laterally displaced and, possibly, when the stator is yawed.

CONCLUSIONS

The force yoke system with the force resolution technique will yield reliable measurements of thrust under all conditions. It will yield reliable measurements of normal force and pitch torque when the magnitude of the normal force is comparable to, or greater than, the magnitude of the thrust.

---

*The thrust distribution is, however, quite smooth.

**And in QPR #5. Note also that A should be replaced by D in Equation (8) of Figure 5-3 in that report. Equation (7) is also incorrect.

All other force data is correct as printed except for roll torque in the presence of lateral force.

Normal (radial component) force printouts should be disregarded when the normal force is less than the thrust. Pitch torque as printed is incorrect and should be computed from Equation (9). This value should be disregarded for normal force less than thrust and also when it is less than 10% of the maximum value.

From an inspection of the comparisons of Table 5-2, for acceptable points it may be estimated that, theoretically, the thrust measurement will be good to within 1% with a scatter of ± 2%, normal forces will average 3% low with scatter of ± 5%, and pitch torques will be 8% low with a scatter of ± 13%. Additional error will be introduced by the characteristics of the sensors and the linear bearings.

It is evident from Figures 4-16, 4-17, and 4-18 that there were no major problems with the sensors, linear bearings, or the effect of motor weight over most of the speed range that would lead to data scatter. However, where the magnitude of the vertical force becomes small compared to the weight of the stator assembly (around 150 N), considerable error and scatter in the data are to be expected. These occur because the motor weight is electronically subtracted from the sensor outputs before scanning by the DAS. But it is precisely under these conditions that it was shown earlier in the section that the normal force readings are inherently in error due to the stator curvature and thrust interference.

In much of the vertical sensor data, regular deviation is present in which sensors B and C appear to have larger readings than A and D (see Figure 3-1 for definitions). This occurs as the result of a small symmetrical thermal twisting of the frame bearing on the sensors. The redistribution of force across the diagonal does not affect the net vertical forces, pitch torques, or rail torques, since the sensors are always used in pairs for their determination.

Looking ahead to the synchronous motor tests, all of the normal force data should be reliable, since normal force will be 5 to 8 times the thrust.

Appendix A

OFF-LINE DATA REDUCTION PROGRAM

This is the final form of the program used to process the linear induction motor data.

```
10◆#RUN◆;TSSLIB/RLINE,R=<NWARN>#DATA"10";TESLA"11"
20 CHARACTER POS◆1<10>/1HA,1HB,1HC,1HD,1HE,1HF,1HG,1HH,1HI,1HJ/
30 CHARACTER VOL◆27<4>/27H<<V<1>-V<74>>/V<1>>◆100.     ,
40 & "<<V<74>-V<75>>/V<1>>◆100.     ","<<V<75>-V<76>>/V<1>>◆100.     ",
50 & "<<V<76>/V<1>>◆100.     "/
60 CHARACTER VOL1◆27<4>/"<<V<77>-V<78>>/V<3>>◆100.     ",
70 & "<<V<3>-V<77>>/V<3>>◆100.     ","<<V<78>-V<79>>/V<3>>◆100.     ",
80 & "<V<79>/V<3>>◆100.     "/
90 REAL NM1,NM2,MAX1,MAX2
100 REAL MAX3,MAX4,MAX5,MAX6,MAX7,MAX1C,MAX3C,MAX5C
110 CHARACTER STORE◆18,STOR1◆30
115 REAL MAX8
120 CHARACTER DATE◆8,TIME◆5
130 DIMENSION ISTART<5>,C<400>,F2<10>,AA<4>,CC<4>
140 DIMENSION V<9>
145 DIMENSION F<10>
150 CHARACTER IBUF◆72
160 INTEGER RNO,DRPM,SHZ,OHZ,AMP,ENG
170C
172C THESE CONSTANTS ARE FOR RUNS
174c 172 AND UP
180C IDENTIFICATION<DATE,TIME,RUN NUMBER,DRUMRPM,SLIP FREQUENCY,
190C OSC FREQUENCY,AMPS AND ENGINEER> IS READ FROM THE FIRST
200C LINE OF FILE "DATA" AND PRINTED AT THE TOP OF THE REPORT.
210C THE FIRST 2 ITEMS ARE IN THE FORM XX/XX/XX AND XX:XX
220C AND THE REMAINING ARE INTEGERS. ALL ITEMS ARE SEPARATED
230C BY BLANKS.
240C
250C
260 READ <10,20> DATE,TIME,RNO,DRPM,SHZ,OHZ,AMP,ENG
270 PRINT 66
280 66 FORMAT<1X////////"DATE",T11,"TIME",T19,"RN#",T26,"DRUMRPM",
290 & T35,"SLIP % ",T45,"OSC HZ",T55,"VOLTS",T63,"ENG"//>
300 PRINT 67,DATE,TIME,RNO,DRPM,SHZ,OHZ,AMP,ENG
310 67 FORMAT<1X,A8,T12,A5,T19,I4,T27,I4,T35,I4,T45,I4,
320 & T55,I4,T65,I1//////>
330
340
350 LSW=3
360 I=1
370C
380C THE REMAINING DATA ITEMS ARE READ AND PLACED IN THE ARRAY
390C <C>. POINTERS ARE SET UP TO THE BEGINNING OF THE THREE SETS
400C OF DATA<-1 SIGNALS THE END OF A DATA SET; -2 SIGNALS THE
410C END OF DATA;THE FIRST ITEM IN EACH SET IS THE STARTING
420C CHANNEL NUMBER,WHICH IS IGNORED>.
430C
440 10 CALL RLINE<10,IENT,LSW,IBUF,$30,$50,$50>
450 DECODE<IBUF,20><C<I>,I=I,I+<IENT-1>>
460 I=I+1
470 20 FORMAT<V>
480 GO TO 10
490 30 N=1
500 ISTART<N>=2
510 DO 40 M=1,I
520 IF<C<M>.NE.-1>GO TO 40
530 IF<C<M+1>.EQ.-2>GO TO 60
540 N=N+1
550 ISTART<N>=M+2
560 40 CONTINUE
570 50 PRINT," ERROR RETURN"
580 GO TO 310
590 60 PRINT 65
600 65 FORMAT<1X,"SENSOR#",T15,"1ST READING",T30,"2ND READING",
610 & T45,"3RD READING",T60,"AVERAGE">
620C
630C THE THREE SETS OF DATA ARE AVERAGED AND THE VALUES STORED
640C AT THE END OF ARRAY <C>. THESE VALUES ARE USED IN THE
650C CALCULATIONS. THE 3 VOLTAGE READINGS AND THE
660C AVERAGE ARE PRINTED OUT.
```

APPENDIX A (Cont'd)

```
670C
680 I1=ISTART(1);I2=ISTART(2);I3=ISTART(3);I4=M+1
690 DO 62 I=1,ISTART(2)-4
700 C(I4)=(C(I1)+C(I2)+C(I3))/300.
710 PRINT 64,I,C(I1)/100.,C(I2)/100.,C(I3)/100.,C(I4)
720 64 FORMAT(1X,T3,I2,T14,F7.4,T29,F7.4,T44,F7.4,T59,F7.4)
730 I1=I1+1;I2=I2+1;I3=I3+1;I4=I4+1
740 62 CONTINUE
750C
760C THE REMAINDER OF THE PROGRAM DEALS WITH MAKING CALCULATIONS
770C (MULTIPLYING THE CONVERSION FACTOR BY THE VOLTAGE READING
780C FROM THE TAPE) AND PRINTING THEM FOR THE FIRST 79 SENSOR
790C READINGS.
800C
810 IB=M+1;IS=1
820 PRINT 23
830 STORE="VOLTS"
840 PRINT 11,STORE
850 11 FORMAT(" LINE",T20,"SENSOR#",T40,"CFACTOR",T60,A6)
860 V1=136.986
870 DO 80 I=1,3
880 V2=V1*(C(IB))
890 V(I)=V2
900 PRINT 12,I,IS,V1,V2
910 12 FORMAT(I2,"-N",T22,I1,T39,F10.4,T58,F10.4)
920 IS=IS+1;IB=IB+1
930 80 CONTINUE
940 PRINT 24
950 STORE="AMPS"
960 PRINT 11,STORE
970 A1=96.98
980 DO 90 I=1,3
990 A2=A1*(C(IB))
1000 VOLAMP=A2*V(I)+VOLAMP
1010 PRINT 12,I,IS,A1,A2
1020 IS=IS+1;IB=IB+1
1030 90 CONTINUE
1040 PRINT 25
1050 STORE="KWATTS"
1060 PRINT 11,STORE
1070 RK1=128.77
1080 RK3=0.
1090 DO 100 I=1,3
1092 IF(I.EQ.2) RK1=142.330
1094 IF(I.EQ.3) RK1=134.902
1100 RK2=RK1*(C(IB))
1110 PRINT 12,I,IS,RK1,RK2
1120 RK3=RK2+RK3
1130 IS=IS+1;IB=IB+1
1140 100 CONTINUE
1150 PRINT 122,RK3
1160 122 FORMAT(1X/T39,"TOTAL KWATTS=",T58,F10.4/)
1170 FR1 = 166.67
1180C
1190C 0.9 IS THE DUMMY SENSOR READING FOR FREQUENCY
1200C
1210 FR2=FR1*0.9
1220 PRINT 44
1230 44 FORMAT(1X,//T20,"SENSOR#",T40,"CFACTOR")
1240 STORE="FREQUENCY(HERTZ)"
1250 PRINT 13,STORE,IS,FR1,FR2
1260 13 FORMAT(1X,A18,T22,I2,T39,F10.4,T58,F10.4)
1270 IB=IB+1;IS=IS+1
1280 RS1=200.0
1290 RS2=RS1*(C(IB))
1300 STORE="POTOR SPEED(RPM)"
1310 PRINT 13,STORE,IS,RS1,PS2
1320 IB=IB+1;IS=IS+1
```

APPENDIX A (Cont'd)

```
1330 NM1=299.3
1340 NM2=NM1*(C(IB))
1350 STORE="SHAFT TORQUE(NM)"
1360 PRINT 13,STORE,IS,NM1,NM2
1370 FW=.0193*RS2-1.17
1380 STORE="F&W TORQUE(NM)="; PRINT 13,STORE,IS,NM1,FW
1390 STORE="ELECTRO-MAG TORQUE((NM)=";PRINT 13,STORE,IS,NM1,(FW+NM2)
1400 NM2=NM2+FW
1410 IB=IB+1;IS=IS+1
1420 DCV1=325/9.75
1430 DCV2=DCV1*(C(IB))
1440 STORE="DC LINK VOLTS"
1450 PRINT 13,STORE,IS,DCV1,DCV2
1460 IB=IB+1;IS=IS+1
1470 DCA1=1000/9.75
1480 DCA2=DCA1*(C(IB))
1490 STORE="DC LINK AMPS"
1500 PRINT 13,STORE,IS,DCA1,DCA2
1510 IB=IB+1;IS=IS+1
1520C
1530C CALCULATE AND PRINT POWER OUTPUT VALUES.
1540C
1550 RKW=NM2*RS2*.00010477
1560 HP=RKW/.746
1570 TR=NM2/.7008
1580 EF=(RKW/RK3)*100.
1590 SL=FR2-(11.*RS2/60.)
1600 PRINT 45
1610 STOR1="KW=";PRINT 42,STOR1,RKW
1620 STOR1="HP=";PRINT 42,STOR1,HP
1630 STOR1="THRUST(NEWTONS)=";PRINT 42,STOR1,TR
1640 STOR1="EFFICIENCY(%)=";PRINT 42,STOR1,EF
1650 POFA=1000.0*RK3*100.0/VOLAMP
1660 STOR1="POWER FACTOR(%)=";PRINT 42,STOR1,POFA
1670 STOR1="KVA=";PRINT42,STOR1,(VOLAMP/1000.0)
1680 STOR1="EFF X PF (PU)=";PRINT 42, STOR1,(EF*POFA/10000.0)
1690 STOR1="SLIP(HERTZ)=";PRINT 42,STOR1,SL
1700 PRINT 26
1710 PRINT 14
1720 14 FORMAT(1X,"POSITION",T20,"SENSOR#",T40,"CFACTOR",T60,"NEWTONS")
1730C
1740C THE 10 FORCE CALCULATIONS ARE STORED IN ARRAY (F2) TO BE USED
1750C IN THE LATER CALCULATIONS ON THE FORCES.
1760C
1770 F1=890.0
1780 DO 109 I=1,4
1790C ATTRACTION PRODUCES A POSITIVE F2(I) I=1,4
1800 F2(I)=F1*(5.00-C(IB))
1810 PRINT 15,POS(I),IS,F1,F2(I)
1820 IB=IB+1; IS=IS+1
1830 109 CONTINUE
1833C
1835C FOR "J" ADD 44.5N OFFSET
1836c
1850 DO 110 I=5,10
1851 F(5) = 445.0*1.236
1852 F(6) = 445.0*1.236
1853 F(7) = 445.0*1.254
1854 F(8) = 445.0*1.254
1855 F(9)=445.0*1.03
1856 F(10)=445.0*1.05
1860 F2(I)=F(I)*(C(IB))
1865 108 IF(I.EQ.10) F2(I)=F2(I)+44.5
1870 PRINT 15,POS(I),IS,F(I),F2(I)
1880 15 FORMAT(3X,A1,T22,I2,T38,F10.4,T58,F10.4)
```

APPENDIX A (Cont'd)

```
1890 IB=IB+1;IS=IS+1
1900 110 CONTINUE
1910C
1920C A NUMBER OF CALCULATIONS ARE MADE USING THE FORCE VALUES
1930C IN THE ARRAY (F2) AND PRINTED OUT BY THE STATEMENTS FOLLOWING.
1940C
1950 RAD=.701; RL=.762; W=.1524; P=.1953
1960 C1=(F2(10)-F2(9))/(F2(1)+F2(2)+F2(3)+F2(4))
1970 BETA=ATAN(C1)
1980 RES=(F2(10)-F2(9))/SIN(BETA)
1990 CC2=(((F2(1)+F2(2)-F2(3)-F2(4))*RL)/2.0)+(F2(9)-F2(10))*(RAD+P)
2000 ALPHA=ARSIN((SIN(BETA)*CC2)/(RAD*(F2(9)-F2(10))))
2010 THETA=BETA-ALPHA
2020 A=RES*COS(ALPHA)
2030 T=RES*SIN(ALPHA)
2035 FTAIL = F2(5)-F2(6)-.78
2036 FLEAD = F2(7)-F2(8)-6.85
2040 PTO=((F2(1)+F2(2))-(F2(3)+F2(4)))*(RL/2.0)
2050 YTQ =  (FLEAD-FTAIL)*(RL/2.0)
2060 RTQ=((F2(2)+F2(4))-(F2(1)+F2(3)))*(W/2.0)
2065 FLAT = FLEAD+FTAIL
2070 PRINT 41
2080 STOR1="RESULTANT OF TZA=";PRINT 42,STOR1,RES
2090 STOR1="FORCE ANGLE OF RESULTANT=";PRINT 42,STOR1,ALPHA
2100 STOR1="LOCATION OF RESULTANT=";PRINT 42,STOR1,THETA
2110 STOR1="RADIAL FORCE=";PRINT 42,STOR1,A
2120 STOR1="TANGENTIAL THRUST=";PRINT 42,STOR1,T
2130 STOR1="PITCH TQ=";PRINT 42,STOR1,PTQ
2140 STOR1="ROLL TQ=";PRINT 42,STOR1,RTQ
2150 STOR1="YAW TQ=";PRINT 42,STOR1,YTQ
2155 STOR1="LATERAL FORCE=";PRINT 42,STOR1,FLAT
2160 STORE="POSITION"
2170 PRINT 27
2180 PRINT 16,STORE
2190 16 FORMAT(1X,A11,T14,"SENSOR#",T24,"CFACTOR",T36,
2200 & "PEAK",T48,"CFACTOR",T60,"RMS")
2210C
2220C THE CONVERSION FACTORS FOR THE FLUX DENSITY ARE READ FROM
2230C FROM THE FILE "TESLA" AND USED IN THE CALCULATIONS.
2240C THE RMS AND MAX VALUES ARE STORED IN THE FILE, FIRST
2250C FOR SENSORS 25 THRU 52, FOLLOWED BY 53 THRU 55, FOLLOWED
2260C BY 56 AND 57. THEY ARE REAL VALUES SEPARATED BY SPACES.
2270C
2280 READ(11,43) RMS1,MAX1,RMS3,MAX3,RMS5,MAX5,RMS8,MAX8
2290 43 FORMAT(V)
2320 RMS2=RMS1*(C(IB))
2330 MAX2=MAX1*(C(IB))
2340 I=-1
2350 PRINT 17,I,IS,MAX1,MAX2,RMS1,RMS2
2360 IB=IB+1;IS=IS+1
2370 DO 120 I=1,53,2
2380 RMS2=RMS1*(C(IB))
2390 MAX2=MAX1*(C(IB))
2400 PRINT 17,I,IS,MAX1,MAX2,RMS1,RMS2
2410 17 FORMAT(1X,"SLOT ",I2,T16,I2,T22,F10.4,T34,F10.4,T46,
2420 & F10.4,T59,F10.4)
2430 IB=IB+1;IS=IS+1
2440 120 CONTINUE
2450 STORE="YOKE BELOW:"
2460 PRINT 16,STORE
2490 DO 130 I=11,33,11
2500 RMS4=RMS3*(C(IB))
2510 MAX4=MAX3*(C(IB))
2520 PRINT 17,I,IS,MAX3,MAX4,RMS3,RMS4
2530 IB=IB+1;IS=IS+1
```

APPENDIX A (Cont'd)

```
2540 130 CONTINUE
2570 RMS6=RMS5*(C(IB))
2580 MAX6=MAX5*(C(IB))
2590 PRINT 18,"BUTT-LEAD ",IS,MAX5,MAX6,RMS5,RMS6
2600 18 FORMAT(1X,A10,T16,I2,T22,F10.4,T34,F10.4,T46,
2610 & F10.4,T59,F10.4)
2620 IB=IB+1;IS=IS+1
2630 RMS7=RMS8*(C(IB))
2640 MAX7=MAX8*(C(IB))
2650 PRINT 18,"BUTT-TRAIL",IS,MAX8,MAX7,RMS8,RMS7
2660 IB=IB+1;IS=IS+1
2670 PRINT 28
2680 PRINT 19,"CELESUA  "
2690 19 FORMAT(1X,"  POSITION",T20,"SENSOR#",T40,"CFACTOR",T60,A9)
2700 PRINT 22
2710 22 FORMAT(1X,"(DRAWING AXXXXXX)")
2720 IB=IB+1;IS=IS+1
2730 T1=21.33
2740 DO 140 I=1,12
2750 T2=T1*(C(IB))
2760 PRINT 21,I,IS,T1,T2
2770 21 FORMAT(1X,T6,I2,T22,I2,T39,F10.4,T58,F10.4)
2780 IB=IB+1;IS=IS+1
2790 140 CONTINUE
2800 PRINT 29
2810 V1=54.7
2820 V2=V1*(C(IB))
2830 STORE="VOLTS"
2840 PRINT 13,STORE,IS,V1,V2
2850 IB=IB+1;IS=IS+1
2860 AM1=(C(IB)-1.)*100.
2870 AM2=AM1*(C(IB))
2880 STORE="AMPS"
2890 PRINT 13,STORE,IS,AM1,AM2
2900 IB=IB+1;IS=IS+1
2910 FAM1=20.04
2920 FAM2=FAM1*(C(IB))
2930 STORE="FLD AMPS"
2940 PRINT 13,STORE,IS,FAM1,FAM2
2950 IB=IB+1;IS=IS+1
2960 PRINT 31
2970 PRINT 19,"TAP VOLTS"
2980 PRINT 22
2990 TV1=94.624
3000 DO 150 I=13,18
3010 TV2=TV1*(C(IB))
3020 V(I-9)=TV2
3030 PRINT 21,I,IS,TV1,TV2
3040 IB=IB+1;IS=IS+1
3050 150 CONTINUE
3060C
3070C CALCULATE PHASE BELT VOLTAGES FROM THE VOLTAGES STORED
3080C IN ARRAY V(I).
3090C
3100 AA(1)=((V(1)-V(4))/V(1))*100.0
3110 AA(2)=((V(4)-V(5))/V(1))*100.0
3120 AA(3)=((V(5)-V(6))/V(1))*100.0
3130 AA(4)=(V(6)/V(1))*100.0
3140 CC(1)=((V(7)-V(8))/V(3))*100.0
3150 CC(2)=((V(3)-V(7))/V(3))*100.0
3160 CC(3)=((V(8)-V(9))/V(3))*100.0
3170 CC(4)=(V(9)/V(3))*100.0
3180 PRINT 35
```

APPENDIX A (Cont'd)

```
3190 PRINT 34;PRINT 36
3200 DO 160 I=1,4
3210 PRINT 32,"A",I,VOL(I),AA(I)
3220 160 CONTINUE
3230 PRINT 33
3240 DO 170 I=1,4
3250 PRINT 32,"C",I,VOL1(I),CC(I)
3260 170 CONTINUE
3270 23 FORMAT(1X//T20,"VOLTS - LINE TO NEUTRAL"//)
3280 24 FORMAT(1X//T25,"AMPS - LINE"//)
3290 25 FORMAT(1X//T20,"KWATTS - LINE TO NEUTRAL"//)
3300 26 FORMAT(1X//T25,"FORCE"//)
3310 27 FORMAT(1X//T20,"FLUX DENSITY IN TESLA"//)
3320 28 FORMAT(1X//T25,"MOTOR TEMP"//)
3330 29 FORMAT(1X//T25,"DC MOTOR"//T20,"SENSOR#",T40,"CFACTOR")
3340 31 FORMAT(1X//T25,"AC MOTOR"//)
3350 32 FORMAT(1X,T3,A1,T22,I1,T33,A27,"=",F10.4)
3360 33 FORMAT(1X,//)
3370 34 FORMAT(1X,"PHASE",T20,"BELT",T43,"VOLTAGE %")
3380 35 FORMAT(1X//T20,"PHASE BELT VOLTAGES"//)
3390 36 FORMAT(1X/T33,"V(X) = VOLTAGE VALUE AT SENSOR X"//)
3400 41 FORMAT(1X,///T18,"REDUCTION OF SENSOR FORCES TO
3410 & RESULTANT FORCES"//)
3420 42 FORMAT(1X,A30,F10.4)
 '30 45 FORMAT(1X//T25,"POWER OUTPUT"//)
 +40 310 STOP;END
3450     SUBROUTINE TEST
3460     CHARACTER PAUSE*4
3470     PRINT, "   WHAT NEXT?"
3480     READ, PAUSE
3490     IF(PAUSE .EQ. "RUN") RETURN
3500     STOP
3510     END
```

Performance of a Single-Sided Linear Induction Motor with Solid Back Iron and with Various Misalignments, 1980
US DOT, FRA, Gerald B Kliman, william R Mischler, W Russel Oney